

**A Numerical Simulation of Mesoscale
Flow over Mountainous Terrain**

by
Richard Lynn Hughes

Department of Atmospheric Science
Colorado State University
Fort Collins, Colorado



**Department of
Atmospheric Science**

Paper No. 303

A NUMERICAL SIMULATION OF MESOSCALE FLOW OVER MOUNTAINOUS TERRAIN

by

Richard Lynn Hughes

Research supported by the
National Science Foundation
Grant # ATM09770
National Center for Atmospheric Research
National Hail Research Experiment
sub-contract # 6106

Department of Atmospheric Science
Colorado State University
Fort Collins, Colorado

December, 1978

Atmospheric Science Paper No. 303

ABSTRACT OF THESIS
A NUMERICAL SIMULATION OF MESOSCALE FLOW
OVER MOUNTAINOUS TERRAIN

A three-dimensional, hydrostatic, primitive equation mesoscale model was used to investigate thermally driven flow over the Colorado Rocky Mountains and plains. One idealized and two real cases were simulated. Some similarities to observations and climatological data were obtained. Episodes of eastward propagation of vertical velocity regions were predicted. Persistent lines of rising motion were simulated near areas of observed enhanced cloudiness. Weakening of the modeled downslope circulation occurred at the time that convection was observed to erupt. There was, however, poor correspondence with the observed surface flow, especially with respect to wind direction. Several possible reasons for the departure of the model from observations were commented upon, with the intents of both discerning causal mechanisms for the observed upslope, and gaining insight into the characteristics of the model. Singled-out as particularly important were the deviation of the model winds from observations during the initialization process, absence of synoptic-scale forcing, local topographic forcing (especially slope heating) and the effects of latent heat release. Suggestions for modification of the model included the development of initialization procedures which accurately simulate observations, and inclusion of a boundary layer parameterization which more effectively decouples

surface flow from the free atmosphere above the nocturnal inversion. One should also consider replacement of the upper boundary condition with conditions which affect the flow less significantly throughout the depth of the model and less diffusive numerical operators.

Richard Lynn Hughes
Department of Atmospheric Science
Colorado State University
Fort Collins, Colorado 80523
Fall 1978

ACKNOWLEDGEMENTS

The author would like to express his appreciation to Dr. William R. Cotton for his valuable suggestions, guidance, and encouragement. The author is also indebted to Mr. Gregory J. Tripoli for his untiring assistance and advice, and to Mr. Raymond L. George for many fruitful discussions. The efforts of Mrs. Lucy McCall in figure drafting and of Mrs. Kathy Malewicz and Mrs. Kathy Pursley in typing and preparation of the manuscript are deeply appreciated. Thanks are also due to Dr. J. C. Fankhauser and Mr. Carl More for their aid in data acquisition.

This research was supported by National Center for Atmospheric Research, National Hail Research Experiment project sub-contract #6016, and National Science Foundation grant #ATMO9770.

TABLE OF CONTENTS

<u>Chapter</u>	<u>Page</u>
1 GOAL OF PRESENT RESEARCH	1
1.1 Introduction	1
1.2 The Import of Mesoscale Studies in General	3
1.3 A Review of Some Mesoscale Modeling	9
2 DESCRIPTION OF THE MODIFIED PIELKE MODEL	16
2.1 Basic Equations Used	16
2.2 Transformation of Co-ordinates	20
2.3 Turbulent Closure	22
2.4 Finite Difference Techniques	26
3 NUMERICAL EXPERIMENTS	31
3.1 Introduction	31
3.2 Experiment A: "Witch of Agnesi" Topography	32
3.3 Experiment B: July 9, 1973 Simulation	38
3.4 Experiment C: August 4, 1977 Simulation	83
3.5 Comparison of Results of Numerical Experiments B and C	102
4 DISCUSSION, SUMMARY AND CONCLUSIONS	106
4.1 Discussion of Results	106
4.2 Comparison with Other Selected Models	111
4.3 Summary and Conclusions	112
4.4 Suggestions for Future Research	113
REFERENCES	117

LIST OF FIGURES

<u>Figure</u>		<u>Page</u>
1	Schematic profile of the eddy exchange coefficients.	23
2	Schematic picture of model grid mesh.	23
3	"Witch of Agnesi" topography (vertical scale is exaggerated).	33
4	Vector plot of horizontal winds at interior grid-points on the $z^* = 0.03$ km surface at five minutes of simulated time. Axis labels are distances in kilometers east and north of the southwest corner of the model domain respectively. Unless otherwise noted, this and all subsequent plots of model output exclude the four gridpoint wide strip of constant topography near the perimeter.	34
5	Contour plots at five minutes of simulated time on the $z^* = 0.03$ km surface of (a) divergence in sec^{-1} contoured from -0.4×10^{-3} to 0.2×10^{-3} in intervals of 0.1×10^{-3} (b) vertical velocity in m sec^{-1} contoured from -0.3 to 0.4 in intervals of 0.1 . In this and all subsequent contour plots, negative values are shaded.	36
6	Vector plot of horizontal winds at interior grid-points on the $z^* = 0.25$ km surface at fifteen minutes of simulated time.	37
7	Cross sectional plot through the $y = 18$ slab at thirty minutes of simulated time. Contour delineates area of negative vertical velocity. Perimetric points are included.	39
8	Topography for Experiments B and C viewed from the north-east corner of the domain (vertical scale is exaggerated).	40
9	Contour plot of deviation of topography from average value used in Experiments B and C, contoured from -750 m to 1250 m in intervals of 250 m. Transparent overlays of this figure are provided.	41
10	Contour plots of deviation of topography from the average value, used in Experiments B and C, contoured from -750 m to 1250 m in intervals of 250 m. Transparent overlays of this figure are provided.	42

LIST OF FIGURES (CONT'D)

<u>Figure</u>		<u>Page</u>
11	Initial winds used for Experiment B.	43
12	Skew-T, log-P plot of the thermodynamic sounding taken at 0500 LST on July 9, 1973 at Denver, and of the sounding used in the model for Experiments A and B. The boxed point shows how the morning inversion was removed.	45
13	Observed and modeled surface temperatures for five locations within the model domain at various elevations for Experiments A and B.	47
14	Semi-logarithmic plot of total kinetic energy in the model for each of the experiments during initialization and simulation.	49
15	Surface weather map for the United States at 0500 LST on July 9, 1973.	51
16	Contour plots at 0230 LST of (a) the height of the planetary boundary layer in decameters contoured from 40 to 130 in intervals of 10 (b) vertical velocity at $z^* = 0.03$ km in m sec^{-1} contoured from -0.4 to 0.4 in intervals of 0.1 (c) divergence at $z^* = 0.03$ km in sec^{-1} contoured from -0.2×10^{-3} to 0.3×10^{-3} in intervals of 0.1×10^{-3} .	52
17	Contour plots at 0230 LST of (a) vertical velocity at $z^* = 2.0$ km in m sec^{-1} contoured from -3.0 to 3.0 in intervals of 1.0 (b) divergence in sec^{-1} at $z^* = 2.0$ km contoured from -1.6×10^{-3} to 1.6×10^{-3} in intervals of 0.8×10^{-3} (c) divergence in sec^{-1} at $z^* = 4.0$ km contoured from -0.2×10^{-3} to 0.2×10^{-3} in intervals of 0.1×10^{-3} .	53
18	Vector plot of horizontal winds at interior grid-points on the $z^* = 0.03$ km surface at 0330 LST.	55
19	Contour plots at 0300 LST on the $z^* = 0.03$ km surface of (a) the height of the planetary boundary layer in decameters contoured from 50 to 150 in intervals of 10 (b) divergence in sec^{-1} contoured from -0.24×10^{-3} to 0.16×10^{-3} in intervals of 0.8×10^{-4} .	57

LIST OF FIGURES (CONT'D)

<u>Figure</u>		<u>Page</u>
20	Contour plots of mixing ratio in grams metric ton ⁻¹ (a) at 0800 LST on the z* = 0.03 km surface contoured from 800 to 860 in intervals of 10 (b) at 1100 LST on the z* = 0.03 km surface con- toured from 770 to 820 in intervals of 10 (c) at 0800 LST on the z* = 2.0 km surface con- toured from 360 to 560 in intervals of 40 (d) at 1100 LST on the z* = 2.0 km surface contoured from 320 to 600 in intervals of 40.	58
21	Contour plots on the z* = 0.03 km surface of vertical velocity in m sec ⁻¹ contoured from -0.5 to 0.3 in intervals of 0.1 at (a) 0530 LST (b) 0600 LST (c) 0630 LST and of (d) the thirty minute change in divergence at 0600 LST in sec ⁻¹ contoured from -0.6 x 10 ⁻⁴ to 0.6 x 10 ⁻⁴ in intervals of 0.3 x 10 ⁻⁴ .	60
22	Contour plots of (a) vertical velocity in m sec ⁻¹ at 0700 LST on the z* = 0.03 km surface contoured from -0.5 to 0.3 in intervals of 0.1 (b) vertical velocity in m sec ⁻¹ at 0830 LST on the z* = 2.0 km surface contoured from -3.0 to 3.0 in intervals of 1.0 (c) divergence in sec ⁻¹ at 0830 LST on the z* = 2.0 km surface contoured from -0.14 x 10 ⁻³ to 0.14 x 10 ⁻³ in intervals of 0.7 x 10 ⁻⁴ (d) the thirty minute change in divergence in sec ⁻¹ at 0700 LST on the z* = 0.03 km surface contoured from -0.9 x 10 ⁻⁴ to 0.6 x 10 ⁻⁴ in intervals of 0.3 x 10 ⁻⁴ .	61
23	Contour plots on the z* = 0.03 surface of (a) vertical velocity at 0830 LST contoured from -0.5 to 0.3 m sec ⁻¹ in intervals of 0.1 m sec ⁻¹ (b) vertical velocity in m sec ⁻¹ at 0930 LST contoured from -0.4 to 0.3 in intervals of 0.1	64
24	Satellite imagery from ATS-3 taken on July 9, 1973 at (a) 0922 LST (b) 1115 LST (c) 1326 LST (d) 1405 LST (e) 1504 LST (f) 1602 LST.	65

LIST OF FIGURES (CONT'D)

<u>Figure</u>		<u>Page</u>
25	Contour plots of vertical velocity in m sec^{-1} on the $z^* = 0.03$ km surface contoured from -0.3 to 0.3 in intervals of 0.1 at (a) 1000 LST (b) 1030 LST (c) 1100 LST.	66
26	Contour plots of vertical velocity in m sec^{-1} on the $z^* = 0.03$ km surface contoured from -0.3 to 0.3 in intervals of 0.1 at (a) 1130 LST (b) 1200 LST.	68
27	Contour plots on the $z^* = 4.0$ km surface at 1200 LST of (a) divergence contoured from -0.18×10^{-3} to 0.18×10^{-3} in intervals of 0.9×10^{-4} (b) the thirty minute change in divergence contoured from -0.12×10^{-3} to 0.8×10^{-3} in intervals of 0.4×10^{-4} .	68
28	Radar data taken at Limon, Colorado on July 9, 1973 at (a) 1114 LST (b) 1150 LST (c) 1201 LST (d) 1415 LST (e) 1458 LST (f) 1525 LST.	69
29	Vector plot of horizontal winds at interior grid-points on the $z^* = 0.03$ km surface at 1230 LST.	71
30	Contour plots of divergence on the $z^* = 0.03$ km surface contoured from -0.14×10^{-3} to 0.14×10^{-3} in intervals of 0.7×10^{-4} at (a) 1330 LST (b) 1415 LST (c) 1515 LST (d) 1615 LST.	73
31	Contour plots of mixing ratio in grams metric ton^{-1} (a) on the $z^* = 0.03$ km surface at 1515 LST contoured from 740 to 810 in intervals of 10 (b) on the $z^* = 0.03$ km surface at 1615 LST contoured from 720 to 800 in intervals of 10 (c) on the $z^* = 2.0$ km surface at 1515 LST contoured from 350 to 600 in intervals of 50 (d) on the $z^* = 2.0$ km surface at 1615 LST contoured from 360 to 600 in intervals of 40.	75
32	Vector plot of horizontal winds at interior grid-points on the $z^* = 0.03$ km surface at 1515 LST.	76
33	Vector plot of horizontal winds at interior grid-points on the $z^* = 0.03$ km surface at 1615 LST.	78

LIST OF FIGURES (CONT'D)

<u>Figure</u>		<u>Page</u>
34	Contour plots of the Exner function in Joules kilogram ⁻¹ °K ⁻¹ on the z* = 0.03 km surface contoured from 87 to 105 in intervals of 3 at (a) 1915 LST (b) 2015 LST.	79
35	Contour plots of potential temperature in °K on the z* = 0.03 km surface contoured from 308 to 312 in intervals of 0.5 at (a) 1415 LST (b) 1515 LST (c) 1615 LST (d) 1715 LST.	81
36	Contour plots of vertical velocity in m sec ⁻¹ on the z* = 0.03 km surface contoured from -0.2 to 0.3 in intervals of 0.1 at (a) 2215 LST (b) 2315 LST.	82
37	Initial winds used for Experiment C.	84
38	Skew-T, log-P plot of the thermodynamic sounding taken at 0500 LST on August 4, 1977 at Limon and of the sounding used in the model for Experiment C.	86
39	Observed and modeled surface temperatures for five locations within the model domain at various elevations for Experiment C. Numbered locations refer to NCAR Portable Automated Mesonet surface stations used during the SPACE.	87
40	Surface weather map for the United States at 0500 LST on August 4, 1977.	89
41	Contour plots on the z* = 0.03 km surface of (a) vertical velocity in m sec ⁻¹ at 0300 LST contoured from -0.4 to 0.4 in intervals of 0.1 (b) vertical velocity in m sec ⁻¹ at 0400 LST contoured from -0.4 to 0.4 in intervals of 0.1 (c) divergence in sec ⁻¹ at 0300 LST contoured from -0.3 x 10 ⁻³ to 0.3 x 10 ⁻³ in intervals of 0.1 x 10 ⁻³ . (d) divergence in sec ⁻¹ at 0400 LST contoured from -0.3 x 10 ⁻³ to 0.3 x 10 ⁻³ in intervals of 0.1 x 10 ⁻³ .	91

LIST OF FIGURES (CONT'D)

<u>Figure</u>		<u>Page</u>
42	Contour plots of (a) divergence at 0500 LST on the $z^* = 0.03$ km surface in sec^{-1} contoured from -0.3 to 0.3 in intervals of 0.1 (b) vertical velocity in m sec^{-1} on the $z^* = 2.05$ km surface at 0500 LST contoured from -4.0 to 4.0 in intervals of 1.0 (c) vertical velocity in m sec^{-1} at 0600 LST on the $z^* = 0.03$ km surface contoured from -0.3 to 0.3 in intervals of 0.1 (d) vertical velocity in m sec^{-1} on the $z^* = 0.03$ km surface at 0800 LST contoured from -0.9 to 0.6 in intervals of 0.3 .	93
43	Contour plots of vertical velocity in m sec^{-1} (a) at 0900 LST on the $z^* = 0.03$ km surface contoured from -0.9 to 0.6 in intervals of 0.3 (b) at 0930 LST on the $z^* = 0.03$ km surface contoured from -0.6 to 0.6 in intervals of 0.3 (c) at 1000 LST on the $z^* = 2.0$ km surface contoured from -4.0 to 6.0 in intervals of 1.0 .	94
44	Satellite imagery taken on August 4, 1977 at (a) 1200 LST (b) 1445 LST (c) 1800 LST (d) 2100 LST (infrared data).	96
45	Contour plot of 1030 LST of vertical velocity in m sec^{-1} on the $z^* = 0.03$ km surface contoured from -0.6 to 0.6 in intervals of 0.3 .	97
46	Contour plots of vertical velocity in m sec^{-1} on the $z^* = 0.03$ km surface (a) at 1130 LST contoured from -0.8 to 0.8 in intervals of 0.4 (b) at 1200 LST contoured from -0.9 to 0.6 in intervals of 0.3 .	97
47	Contour plots of vertical velocity in m sec^{-1} at 1500 LST (a) on the $z^* = 0.03$ km surface contoured from -0.4 to 0.4 in intervals of 0.2 (b) on the $z^* = 2.0$ km surface contoured from -3.0 to 5.0 in intervals of 1.0 .	99
48	Contour plot of mixing ratio in grams metric ton^{-1} on the $z^* = 0.03$ km surface contoured from 220 to 234 in intervals of 2 at (a) 1700 LST (b) 1900 LST.	99

LIST OF SYMBOLS

<u>Symbol</u>		<u>Value</u>	<u>Units</u>
\bar{a}	mean value of a(a can be q, T,u, ρ , or θ)		
a'	perturbation value of a		
C_p	Specific heat of air at constant pressure	1.004×10^7	Joule $g^{-1} \text{ } ^\circ K^{-1}$
f_j	j^{th} component of Coriolis parameter		sec^{-1}
g	effective surface acceleration due to gravity	980	cm sec^{-2}
H	Height of boundary layer		cm
h	Height of surface layer		cm
K_H	Horizontal eddy exchange coefficient		$\text{cm}^2 \text{ sec}^{-1}$
K_z^m	Vertical eddy momentum exchange coefficient		$\text{cm}^2 \text{ sec}^{-1}$
K_z^q	Vertical eddy moisture exchange coefficient		$\text{cm}^2 \text{ sec}^{-1}$
K_z^θ	Vertical eddy heat exchange coefficient		$\text{cm}^2 \text{ sec}^{-1}$
L	Monin-Obukhov length		cm
p	pressure		K Pa
q	Mixing ratio		$g g^{-1}$
R	Gas constant for dry air	2.87×10^6	$\text{erg } g^{-1} \text{ } ^\circ K^{-1}$
s	height of material surface		cm
\bar{s}	initial height of material surface	1.1×10^6	cm
T	Temperature		$^\circ K$
t	time		sec

LIST OF SYMBOLS (Cont'd)

<u>Symbol</u>	<u>Value</u>	<u>Units</u>
t'	transformed time co-ordinate	sec
u	Eastward velocity	cm sec ⁻¹
u_*	Friction velocity	cm sec ⁻¹
v	Northward velocity	cm sec ⁻¹
w	Vertical velocity	cm sec ⁻¹
w^*	Transformed vertical velocity	cm sec ⁻¹
w_*	free convection friction velocity	cm sec ⁻¹
x_i	distance in i^{th} direction	cm
x'_i	transformed distance	cm
z_G	height of terrain	cm
z_o	surface roughness length	cm
z^*	transformed vertical co-ordinate	cm
α	arbitrary constant (see eq. 30)	0.72
δ_{ij}	Kroniker delta	1 for $i=j$ 0 for $i \neq j$
ϵ_{ijk}	three dimensional Levi-Civita symbol	1 for ijk an even permutation of 123 -1 for ijk an odd permutation of 123 0 otherwise
ζ	dimensionless height	
ζ_o	dimensionless roughness length	
θ	potential temperature	°K

LIST OF SYMBOLS (Cont'd)

<u>Symbols</u>		<u>Value</u>	<u>Units</u>
θ_s	Surface potential temperature		$^{\circ}\text{K}$
θ_*	Scaling temperature		$^{\circ}\text{K}$
ν	Kinematic viscosity coefficient		cm
π	Exner function		Joules $\text{g}^{-1} \text{ } ^{\circ}\text{K}^{-1}$
ρ	density		g cm^{-3}
ϕ_h	dimensionless temperature gradient		
ϕ_m	dimensionless wind shear		
χ_T	Thermal diffusion coefficient		$\text{cm}^2 \text{ sec}^{-1} \text{ } ^{\circ}\text{K}^{-1}$
ψ_1	integrated form of dimensionless wind shear relation		
ψ_2	integrated form of dimensionless temperature gradient		
Ω	Angular velocity of earth	7.2722×10^{-5}	sec^{-1}

1. GOAL OF PRESENT RESEARCH

1.1 Introduction

For many reasons weather patterns of the Colorado eastern slope and plains are an important area of research. The winter and summer climates are both important contributors to the tourist industry of the state (Thompson, 1971). Understanding local patterns of convection can aid in recreational planning, in control of range and forest fires, and in planning air quality strategies. Areal-specific forecasting is also important for agricultural purposes. The forecasting of the time and intensity of rainfall and dust storms as well as snow depth and wind velocity could be an invaluable boon to the dryland farmer (Yang, 1967). Opportunities for weather modification both for the purpose of precipitation enhancement and for secondary benefits such as pest control might be improved by understanding the natural circulation (Committee on Climate and Weather Fluctuation and Agricultural Production, 1976). The Great Plains area suffers an annual average crop loss to hail damage of 86.7 million dollars (out of a national total of 284.1 million dollars--1967 prices) (Gokhale, 1975). It is clear that an understanding of mesoscale weather, particularly convective weather could result in economic and social benefits.

Several studies have noted the eastward progression of thunderstorms across the great plains. Dirks (1969) numerically simulated the effects of the sloping plain in producing a two-celled circulation. Wetzel (1973) established the "dominance of local topography and moisture availability on the presence and motion of convective storms

in the area". His calculations of daily moisture budgets indicate that local convergence induced by mountain--plains circulation was a dominant mechanism for producing convection on the majority of summer days studied, operating independently of large-scale features. His radar climatology showed preferential genesis and propagation regions occurring over the Cheyenne and Palmer ridges with a later, more stationary convective maximum near the foothills.

It therefore seems fitting to investigate numerically the basis for this behavior. Clearly, to simulate this flow, a three-dimensional model is needed. If the elevated heating mechanism discussed by Dirks (1969) is indeed the driving mechanism for this phenomenon, the initial circulation should be apparent even in a model which contains none of the effects of latent heat.

The dominant influence of mesoscale forcing on convective scales has been often noted. The findings of Henz (1974) that mountain and ridge convection genesis sites produce 40% of all thunderstorm systems and 73% of severe weather occurrences in the study area indicate the importance of mesoscale topography in the initiation of convection. The characterization of these sites by proximity to low-level moisture sources and to topography which maximizes convergence emphasizes the importance of mesoscale flow to convection. His further findings concerning the importance of shallow fronts, meso-highs and dry line discontinuities are an indication that mesoscale forcing is a complex and dynamic process, beyond the resources of real-time conventional analysis. Indeed, it has been found that three hour sondes contain "highly significant" features on the mesoscale missed in the corresponding 12 hour data (Randerson, 1975). Case study work also

points up the importance of mesoscale forcing to convection. Fujita, et al (1962) were able to follow the development of a small low-pressure area on a heated slope to a convergence field leading to morning convection. Cotton, et al (1976) in a numerical study discerned mesoscale forcing in (1) perturbation of thermodynamic profiles, (2) increased depth of the planetary boundary layer, (3) changes in surface flux, (4) changes in vertical shear, and (5) development of convergence regions.

1.2 The Import of Mesoscale Studies in General

When Orlanski (1973) introduced the now-common terminology for mesoscales¹, it was reflective of the growing realization that the time had come when atmospheric phenomena of this size should be energetically investigated. The importance of these phenomena has long been recognized (Fujita, et al 1956), but the singular difficulties presented by this scale had often diverted attention to the more classical areas of micro- and synoptic scale meteorology. The increased interest in urban environments and severe storms has combined with new observational and computational tools to make investigation in this field not only feasible but imperative.

Besides the intrinsic interest induced by a largely unexplained area of investigation, many of the phenomena encountered on the mesoscale e.g. squall lines, hail and tornadoes, generate inquisitiveness. Mesoscale studies are also pursued for their relationship to atmospheric occurrences on other scales.

¹Orlanski proposed the following terminology: The meso- α scale is 200-2000 km, the β scale is 20-200 km, the γ scale is 2-20 km. This study is concerned with the β scale.

Even though, for certain purposes, the mesoscale is viewed as parasitic on large scale events (Perkey, 1976), the large scale environment can be so appreciably affected by occurrences on the mesoscale that the relationship might be more properly termed symbiotic. The feedback from mesoscale activity can actually be significant enough that the determination of which scale is a cause and which an effect becomes difficult (Lewis, et al 1974; George and Cotton, 1978). In particular, there is evidence that mesoscale vertical motion can interact significantly with synoptic scale vertical motion (Randerson, 1975; Lewis, 1973). One study further found that mesoscale convection provides substantial energy input into the atmosphere; the conversion from available potential energy to kinetic energy being on the order of $0.8 \text{ cal cm}^{-1} \text{ day}^{-1}$ (Randerson, 1975). Kaplan and Paine found in a numerical study (1973) that not only the release of latent heat, but also the propagation of gravity waves can have significant effect on large scale motion. The theory of a gravity wave mechanism for meso-macro scale interaction has undergone periodic sufferance and disfavor. Recently, Uccelli (1973) has given observational evidence and theoretical arguments to support the occurrence of gravity waves and Lewis and Ogura (1973) have found stratification discontinuities conducive to their initiation.

In addition to scale interaction considerations, many mesoscale features are of interest in themselves. Chemical and thermal pollution are strongly affected by local conditions (Scorer, 1972) resolvable on the mesoscale. Many conventional weather events are likewise influenced by mesoscale forcing. Squall lines seem to be related to mesoscale convergence zones (Lewis et al 1974). Rainbands

are correlated with mesoscale vertical motion (Elliot and Einer, 1964). Thunderstorm activity is often organized on the mesoscale (Dirks, 1969) and may be dominated by such interactions as thunderstorm outflow and gravity waves (Lilly, 1977).

It is only recently, however, that advances in observational and computational tools have made it possible to conduct thorough investigations of these phenomena. Satellite observations now make it possible to obtain data on the necessary scales (Kreitzberg, 1977). Measurement systems such as METROMEX and PAM (Chagnon, 1975; Cotton and George, 1978) have now become economically viable. Unfortunately, such systems generally yield only surface values yet still produce an enormous amount of data, taxing even computer reduction methods (Giraytys, 1975). Three-dimensional data can of course be obtained by special field projects such as the South Park Area Cumulus Experiment (SPACE) (Danielson and Cotton, 1978) but these data are not available on a routine basis. The complexity of mesoscale events makes a quantitative study necessary for a complete qualitative understanding (Kreitzberg and Perkey, 1976). The degree of sophistication needed for a particular application can be estimated only after the nature of the events are grasped. Thus it may eventually be decided that the mesoscale can be parameterized in synoptic models, but this can be determined only after a quantitative understanding has been achieved (Kreitzberg, et al 1974). The SESAME project plan (Lilly, ed., 1975) determined that to model severe storms it would be necessary to input such mesoscale forces as (1) frontal-scale baroclinic development, (2) topography, (3) boundary layer transports and (4) gravity waves. These are not resolvable from

standard synoptic data. In the absence of a dense rawinsonde network or more sophisticated satellite data, these inputs must be obtained from a mesoscale model. Besides needing more dense data, cumulus scale models will require time-varying boundary conditions which again suggest the need for numerical modeling on the mesoscale.

A computing machine with an infinitesimal cycle time and an infinite memory could conceivably model all atmospheric motion from molecular to global scales. The constraints of state-of-the art machines, algorithms and data make it unrealistic to hope for more than two orders of magnitude difference between the largest and smallest scales resolvable (Anthes,1976), or a computing time on a scale much smaller than real time (Ross,1974). Thus mesoscale models need to account for synoptic scale and cloud scale effects by a method other than explicit calculation, such as by parameterization or through boundary conditions (Manton and Cotton,1977).

Much valuable information has been gained by the resolution afforded by two-dimensional models, discussed below. This study, however, focuses upon the characteristics of a three-dimensional mesoscale model. Several studies (Dirks, 1969; Anderson, 1971) have noted the importance on the mesoscale of local topography which certainly requires fully three-dimensional simulations. The effects can be felt on short time scales pertinent to pollution studies (Anderson, 1971) and on much longer climatological scales (Wallace and Hartranft, 1969). Another three-dimensional feature important to mesoscale circulation is the large-scale forcing. The importance has been established both observationally (Pielke and Cotton, 1977) and by means of numerical studies (Pielke, 1973). Features such as large-scale moisture convergence (Wetzel, 1973; Modahl, 1978) wind and temperature distributions

(Lewis et al 1974), and large scale instability (Dirks, 1969) can be of significant import to mesoscale circulation.

Although of somewhat smaller importance than large scale forcing, small scale feedback cannot be ignored if one is trying to simulate mesoscale vents even the size of rainbands (Kreitzberg and Perkey, 1976). Feedback from this scale can come through such mechanisms as gravity waves, radiation effects, latent heating, vertical eddy momentum transport and boundary layer disturbances. Since cloud scale events have an important time-dependent effect on mesoscale events, which in turn may act as forcing for further cloud scale activity-- all interacting on the time-scale of the mesoscale events, i.e. a few hours (Kreitzberg and Perkey, 1977), it seems clear that the treatment of small-scale dynamics should not be time-invariant. Pielke (1974) has mentioned three possible treatments of the problem. An ensemble cloud type was the basis of the parameterization of Arakawa and Schubert (1974). An often-used approach is that of running a one-dimensional cloud model at appropriate times as, for instance, in Kreitzberg and Perkey (1976). Cotton and Tripoli (1978) have developed a fully three-dimensional model which may aid in investigating scale relationships, but almost certainly will require dynamic initialization and boundary values for long-term real case studies. If, as discussed above, a mesoscale model is used to provide boundary conditions for the cloud model there must be some way to parameterize cloud scale effects prior to initialization time (Cotton, 1974). Kreitzberg has concluded that his one-dimensional "parameterization and calculation of the impact of the convection on the environment are satisfactory" for his purposes (Kreitzberg, et al

1974), at least until the case of the tilted updraft (Kreitzberg, 1974). This parameterization has, up until now, been applied only to quite idealized situations. Cotton and Tripoli (1978) have demonstrated the importance of three-dimensional shear in producing realistic vertical moisture profiles. For a three-dimensional mesoscale model, there are several small-scale phenomena which might be important (Cotton, et al 1976) such as the depth of the planetary boundary layer and changes in vertical flux, which would be beyond the capacities of a one-dimensional treatment of the small scale (Cotton, Hahn and Banta, 1978). Wilhelmson and Klemp (1978) and Moncrieff and Miller (1976) have shown numerically the importance of three-dimensional shear interacting with the gust front in sustaining a storm and influencing its movement.

Thus, it can be seen that an important aspect of both theoretical and applied studies of mesoscale phenomena is the numerical model. The particular application of the model will determine its characteristics, but it has been noted that among the properties of an ideal mesoscale model are:

1. full three-dimensionality
2. realistic topography
3. time-dependent forcing from the large scale
4. time-dependent parameterization of small scale
5. ability to couple with larger and smaller scale models
6. simulation of important phenomena such as gravity waves, radiation, planetary boundary layer, mesoscale pressure anomalies, rain evaporation and momentum transport.

This study will use a three-dimensional, thermodynamically dry mesoscale model with a diurnal heating function to investigate the

mountain-plain circulation over eastern Colorado. Since the model is "dry" it will not only be relatively economical with respect to computation time but will have the effect of separating strictly diabatic effects from latent heat effects.

1.3 A Review of Some Mesoscale Modeling

One of the earliest mesoscale models was written by Sasaki (1959) to study the initiation of squall lines. His model was integrated on a small grid (250 n.mi. x 600 mb) and, because of the computing facilities then available (the IBM 650 was used), it was integrated only ten time steps of six minutes each. He was able to conclude that two significant factors in squall line formation are imbalances between thermal and actual winds, and low-level moisture supplies.

The first of a series of numerical studies by Orville (1964) considered a one km mountain with a 45° slope adjacent to a two km plain. The model was driven by a sinusoidal potential temperature wave whose amplitude decreased linearly from 7°C on the plain to 3°C at the summit. The streamfunction equations of Ogura (1962) were integrated in two dimensions by the forward upstream method for two cases: a neutral environment and a slightly stable environment. The first experiment yielded a "bubble" which moved up the slope and then over the plain. The stable environment produced columnar-shaped convection over the ridge. The results showed some similarity to slope wind observations, such as the pressure deviation and shapes of isentropes, but it was noted that the forcing conditions and dimensionality were of dubious validity.

The next study in this series (Orville, 1965) included moisture effects. These indicated that the moisture augments the development of upslope motion. Increased stability strongly damped development. The position of the stream function center with respect to the cloud has a strong effect on cloud development and shape. Other experiments showed the suppressing effect of both decreased slope angle and greater eddy mixing coefficient.

The effect of including ambient winds and discerning the flow barrier aspects of orography were discussed in the subsequent study (Orville, 1968). A linearly increasing wind tends to prompt an earlier initiation which develops downwind of the ridge, but grows more slowly than in calm winds. A mountain wave simulation results in a rapid development and advection out of the grid. Orville concludes that further work should include three dimensions, treatment of evaporative processes and a surface radiation budget.

Evaporation and cloud shadow effects are included in the next study (Liu and Orville, 1969). Precipitation physics were parameterized following a procedure similar to Kessler (1969). Evaporative downdrafts developed which generally shortened the lifetime of the clouds. Shadow effects increased propagation rates and decreased subsequent cloud sizes. Autoconversion as formulated by Berry was compared with that of Kessler. Little difference is found in development times, but the Berry method yielded more precipitation.

Orville and Sloan (1970) extended the two-dimensional model to ten kilometers in width and height. They simulated the hour-long development, maturation and dissipation of a precipitating thunderstorm. Among their conclusions was that two-dimensionality forced evaporative

erosion of the updraft and proposed that three-dimensional models might avoid this fate. A later version (Orville and Kopp, 1977) included hail calculations and mentions the possibility of interfacing with a three-dimensional mesoscale model.

In an attempt at observational verification of numerical prediction on the mesoscale, Fosberg (1967) using a network of rawinsondes found agreement with the models then commonly used (Orville, 1964; Lilly, 1964; Beuttner and Thyer, 1965; and Asai, 1964) in energy calculations, position of the solenoid cell, and perturbation motion values, but found the valley winds were somewhat precocious and the unstable layers were too shallow.

In an attempt to explain the observed behavior of Colorado Plains convection, Dirks (1969) modeled dry upslope flow with a scheme similar to Liu and Orville (1969) except that a sloping plain of 180 km was included and the grid was extended vertically to 10 km. In a weak stability study ($\partial\theta/\partial z = 1^\circ\text{C}/\text{km}$) a region of ascent was found 75-100 kilometers east of the ridge, resulting from interaction of the ridge and sloping plain circulations. Dirks also found an enhancement of the mountain slope cell by vertical shear.

The choice of two-dimensional constant-slope topography had been largely a result of the difficulty of formulating equations for an irregularly shaped domain. In his doctoral dissertation, Gal-Chen (1973) formulated appropriate equations in a generalized non-orthogonal co-ordinate system. He applied these results in a two-dimensional model of symmetric and asymmetric heating on a continuous slope, in neutral and stable conditions. He also observed the climb of the vortex center up the hill but, unlike Orville, found a weak

secondary circulation beyond the base of the hill; a phenomenon with some observational support. He later (1975) attributed this to advective cooling, rather than mechanical convergence. He found agreement with observations that the depth of the upslope and unstable layer both increase uphill.

Pollution studies have given impetus to much mesoscale modeling. Tang developed the first three-dimensional model of diffusion in a valley terrain (1973). Using a "V" shaped valley and cyclic boundary conditions, he concluded that vehicular pollutants are particularly stagnant in such situations.

The study of squall lines was taken up again by Hane (1973) who used a two-dimensional model employing a nine point Arakawa advective scheme and centered differences elsewhere. He found several surges of convection which maintained themselves by interaction with the synoptic environment through updraft-downdraft patterns. His results indicated three areas in which three-dimensional treatment would be important:

1. The region of contact between downdraft and the earth,
2. The extra-cloud compensating downdraft, and
3. The upper half of the cloud where environmental flow is strong.

Lavoie (1973) undertook a quasi-two-dimensional simulation of lake effect flow represented by three layers: a constant flux layer overlain by a well-mixed planetary boundary layer overlain by a deep stable layer. The hydrostatic model included latent heat and terrain effects and was integrated using forward upstream schemes to steady state. The model predicted vertical velocities and changes in the inversion height. He isolated the forcing functions and found some

mountain waves generated by topography, and convergence generated by friction. The main forcing function was, however, land-water potential temperature differences. A similar model was applied by Lavoie (1974) to the trade wind flow over Oahu. He found good qualitative agreement with cloud base height but the model tended to over-predict precipitation amounts.

Huang (1969) adapted the Lavoie model for use over the Black Hills topography of South Dakota. In following the perturbations of the inversion height, he concluded that in this model, the topographical forcing is the most significant, followed by the effects of heating and the surface friction effect.

Another three-dimensional model has been described by Anthes (1974a). This model, based on an earlier version which attempted to simulate hurricane dynamics (Anthes, 1974b), and using sigma as a vertical co-ordinate developed almost stagnant winds in the lee of the Appalachians which Anthes attributed to gravity waves initiated by the topography. He noted the sensitivity of the model to the large-scale boundary conditions and reported difficulties in obtaining appropriate verification data.

Yet a different vertical co-ordinate was the sigma-theta system used by Devon (1976). The problem of co-ordinate surfaces intersecting the ground, which has plagued this system was circumvented by hybridizing with a pressure co-ordinate system near the surface. The model was two-dimensional and used "leapfrog" differencing in time and a modified central difference in space. A mountain wave was simulated, but the main result of the experiment was the establishment of the feasibility of this hybrid system over complex terrain.

The co-ordinate transform referred to in the work of Gal-Chen was used by Clark (1976) in the development of a three-dimensional model. In a comparison of results with linear theory, Clark found agreement in total wave drag and structure of the vertical velocity field.

A three-dimensional mesoscale model of the sea breeze over south Florida written by Pielke (1973) was able to simulate convergence zones as detected by remote photography and radar. The basis of this model was the Navier-Stokes equations, along with the quasi-Boussinesq form of the continuity equation and the thermodynamic equation (ignoring radiation flux divergence). These were formulated in terms of perturbation values for the winds and scaled pressure (Exner function). The domain of integration extended to five kilometers vertically.

Subsequent versions of the model (Pielke and Mahrer, 1975) included total rather than perturbation quantities and performed the pressure integration downward from the material surface. Additionally, the height of the planetary boundary layer was predicted by a method based on Deardorff (1974).

A study by Mahrer and Pielke (1975) incorporated topography via a co-ordinate transform and initiated the model by a gradual increase of the topography from a flat surface. Later, (Mahrer and Pielke, 1976) a three-dimensional version of this model was used in a study of flow over Barbados. The significance of topography in producing low-level sinking on the westward slopes and upward motion on the windward side of the island corresponded to observations, but it was not possible to relate nighttime precipitation increases

to convergence zones. This version of the model forms the basis for much of the work to be discussed and will be described extensively in Chapter 2.

More recently, Mahrer and Pielke (1977a, 1977b) have modified the model by calculating surface temperatures from a heat balance equation and including radiation heating. Initiation of variables is done along horizontal planes, using a gradual growth of the topography for the case studies, and initializing by a balance equation for the idealized sea breeze-mountain circulation.

2. DESCRIPTION OF THE MODIFIED PIELKE MODEL

2.1 Basic Equations Used

The prognostic variables for the model are u , v , θ , and q as well as the height of the material surface, s , and the height of the planetary boundary layer, H . Vertical velocity and the Exner function of pressure, π , are diagnosed. The momentum equations can be written in the form:

$$\frac{\partial u_i}{\partial t} = -u_j \frac{\partial u_i}{\partial x_j} - \frac{1}{\rho} \frac{\partial p}{\partial x_i} - g \delta_{3i} + \nu \frac{\partial^2 u_i}{\partial x_j \partial x_j} - \epsilon_{ijk} f_j u_k \quad (1)$$

where

$$f_j = \{0, \cos \phi, \sin \phi\}. \quad (2)$$

Molecular/viscous diffusion is ignored in the model. Dividing thermodynamic variables into mean and perturbation values

$$a = \bar{a} + a',$$

where

$$|a'/\bar{a}| \ll 1; \quad a = \rho, T, \text{ or } \theta \quad (3)$$

and applying the equation of state, one derives

$$\bar{\rho}(1 + \rho'/\bar{\rho}) = \frac{p}{R\bar{T}(1+T'/\bar{T})},$$

$$\text{so that } \bar{\rho} \approx p/R\bar{T}. \quad (4)$$

Applying this to the pressure gradient term of (1) yields

$$-R\bar{T} \partial \ln p / \partial x_i. \quad (5)$$

Log differentiation of the definition of π

$$\pi = C_p (p/p_0)^K; \quad (6)$$

where $\kappa = R/C_p$, $P_o = 100$ kPa

yields

$$\frac{\partial \ln \pi}{\partial x_i} = \kappa \frac{\partial \ln p}{\partial x_i} \quad (7)$$

which, substituted into (5) gives

$$-\frac{R\bar{T}}{\kappa} \frac{\partial \ln \pi}{\partial x_i} = -\frac{C\bar{T}}{p} \frac{\partial \pi}{\partial x_i} = -\bar{T} \left(\frac{P_o}{p}\right)^\kappa \frac{\partial \pi}{\partial x_i} \quad (8)$$

Using the definition of potential temperature:

$$\theta = T \left(\frac{P_o}{p}\right)^\kappa, \quad (9)$$

one similarly derives

$$\bar{\theta} \approx \bar{T} \left(\frac{P_o}{p}\right)^\kappa \quad (10)$$

Combined with (8) one finds for the pressure gradient term

$$-\bar{\theta} \frac{\partial \pi}{\partial x_i} \quad (11)$$

This leaves as the momentum equation:

$$\frac{\partial u_i}{\partial t} = u_j \frac{\partial u_i}{\partial x_j} - \theta \frac{\partial \pi}{\partial x_i} - g \delta_{3i} - \epsilon_{ijk} f_j u_k \quad (12)$$

The atmosphere is assumed to be hydrostatic. Conditions for this are discussed by Haltiner (1971) viz. $D^2/L^2 \ll 1$, where D is a characteristic vertical scale and L is a characteristic horizontal scale. The phenomenon of interest in the simulations described below is the upslope circulation. Taking 200 kilometers as a characteristic distance from the Continental Divide to the plains (which would represent a half-wavelength), and a 5 kilometers as a vertical wavelength,

$$\frac{D^2}{L^2} = 1.625 \times 10^{-4} \quad .$$

This is well within the constraint of Haltiner. Therefore, the hydrostatic equation is employed for the vertical momentum equation, which takes the form:

$$\frac{\partial \bar{\pi}}{\partial z} = - \frac{\bar{g}}{\theta} . \quad (13)$$

The thermodynamic equation can be expressed in the form

$$\frac{\partial \theta}{\partial t} = - u_j \frac{\partial \theta}{\partial x_j} + \chi_T \frac{\partial^2 \theta}{\partial x_j \partial x_j} - \text{radiation flux divergence} + \text{latent heat} . \quad (14)$$

Radiation flux divergence is ignored in the model. As pointed out by Busch (1973) this assumption is questionable, and will probably result in discrepancies in experimental results. Condensation effects are also ignored. As mentioned in Walmsley and Reid (1976) this should probably be included in future versions of the model to avoid super-saturation. This leaves for the thermodynamic equation:

$$\frac{\partial \theta}{\partial t} = - u_j \frac{\partial \theta}{\partial x_j} . \quad (15)$$

In the moisture conservation equation, condensation is also ignored, so moisture can be regarded as a "tracer", affected only by advection, and diffusion, thus:

$$\frac{\partial q}{\partial t} = - u_j \frac{\partial q}{\partial x_j} . \quad (16)$$

Equations 12, 15, and 16 are Reynolds averaged using the notation:

$$a = \bar{a} + a' ; a = u_j, \theta, q, \pi$$

To yield:

$$\frac{\partial \bar{u}_i}{\partial t} = -\bar{u}_j \frac{\partial \bar{u}_i}{\partial x_j} - \bar{\theta} \frac{\partial \bar{\pi}}{\partial x_i} - \epsilon_{ijk} f_j \bar{u}_k - \frac{\partial}{\partial x_j} (\overline{u'_i u'_j}) \quad (17a)$$

$$\bar{\theta} \frac{\partial \bar{\pi}}{\partial x_i} = -g \quad (17b)$$

$$\frac{\partial \bar{\theta}}{\partial t} = -\bar{u}_j \frac{\partial \bar{\theta}}{\partial x_j} - \frac{\partial}{\partial x_j} (\overline{u'_j \theta'}) \quad (17c)$$

and

$$\frac{\partial \bar{q}}{\partial t} = -\bar{u}_j \frac{\partial \bar{q}}{\partial x_j} - \frac{\partial}{\partial x_j} (\overline{u'_j q}) \quad (17d)$$

The incompressible continuity equation averages to:

$$\frac{\partial \bar{u}_i}{\partial x_i} = 0. \quad (17e)$$

The diffusion terms in the resulting equations are modeled by K-theory:

$$-\overline{u'_i u'_j} = \begin{cases} K_H \frac{\partial \bar{u}_i}{\partial x_j}, & j = 1, 2 \\ K_z^{(m)} \frac{\partial \bar{u}_i}{\partial x_j}, & j = 3 \end{cases} \quad (18a)$$

$$-\overline{u'_j \theta'} = \begin{cases} K_H \frac{\partial \bar{\theta}}{\partial x_j}, & j = 1, 2 \\ K_z^{(\theta)} \frac{\partial \bar{\theta}}{\partial x_j}, & j = 3 \end{cases} \quad (18b)$$

$$-\overline{u'_j q'} = \begin{cases} K_H \frac{\partial q}{\partial x_j}, & j = 1, 2 \\ K_z^{(q)} \frac{\partial q}{\partial x_j}, & j = 3. \end{cases} \quad (18c)$$

2.2 Transformation of Co-ordinates

The vertical co-ordinate used in the model is

$$z^* = \frac{\bar{s} - z - z_G}{\bar{s} - z_G}, \quad (19)$$

where s is the height of the material surface, and z_G is the terrain height. \bar{s} is the initial value of s . Since $z_G = z_G(x, y)$, by the chain rule,

$$\frac{\partial a}{\partial x} = \frac{\partial a}{\partial x'} \frac{\partial x'}{\partial x} + \frac{\partial a}{\partial y'} \frac{\partial y'}{\partial x} + \frac{\partial a}{\partial z^*} \frac{\partial z^*}{\partial x} + \frac{\partial a}{\partial t'} \frac{\partial t'}{\partial x}. \quad (20)$$

Because z^* is parallel to z , $x' = x$, $y' = y$, and $t' = t$, thus,

$$\frac{\partial a}{\partial x} = \frac{\partial a}{\partial x'} + \frac{\partial a}{\partial z^*} \frac{\partial z^*}{\partial x} \quad (21)$$

and similarly

$$\frac{\partial a}{\partial y} = \frac{\partial a}{\partial y'} + \frac{\partial a}{\partial z^*} \frac{\partial z^*}{\partial y}; \quad (22a)$$

$$\frac{\partial a}{\partial z} = \frac{\partial a}{\partial z^*} \frac{\partial z^*}{\partial z}; \quad (22b)$$

$$\frac{\partial a}{\partial t} = \frac{\partial a}{\partial t'} + \frac{\partial a}{\partial z^*} \frac{\partial z^*}{\partial t}. \quad (22c)$$

Applying the chain rule to evaluate terms involving z^* we find

$$\frac{\partial z^*}{\partial x} = \frac{\partial z^*}{\partial s} \frac{\partial s}{\partial x} + \frac{\partial z^*}{\partial z_G} \frac{\partial z_G}{\partial x} \quad (23)$$

$$\frac{\partial z^*}{\partial y} = \frac{\partial z^*}{\partial s} \frac{\partial s}{\partial y} + \frac{\partial z^*}{\partial z_G} \frac{\partial z_G}{\partial y}. \quad (24)$$

Differentiating equation 19 to yield

$$\frac{\partial z^*}{\partial z_G} = \frac{z^* - \bar{s}}{s - z_G}; \quad (25a)$$

$$\frac{\partial z^*}{\partial s} = \frac{-z^*}{s - z_G}; \quad (25b)$$

$$\frac{\partial z^*}{\partial z} = \frac{\bar{s}}{s - z_G}; \quad (25c)$$

and substituting gives us

$$\frac{\partial a}{\partial x} = \frac{\partial a}{\partial x'} + \frac{\partial a}{\partial z^*} \left[\frac{z^* - \bar{s}}{s - z_G} \frac{\partial z_G}{\partial x'} - \left(\frac{z^*}{s - z_G} \right) \frac{\partial s}{\partial x'} \right] \quad (26a)$$

$$\frac{\partial a}{\partial y} = \frac{\partial a}{\partial y'} + \frac{\partial a}{\partial z^*} \left[\frac{z^* - \bar{s}}{s - z_G} \frac{\partial z_G}{\partial y'} - \left(\frac{z^*}{s - z_G} \right) \frac{\partial s}{\partial y'} \right] \quad (26b)$$

$$\frac{\partial a}{\partial z} = \frac{\partial a}{\partial z^*} \frac{\bar{s}}{s - z_G} \quad (26c)$$

$$\frac{\partial a}{\partial t} = \frac{\partial a}{\partial t'} + \frac{\partial a}{\partial z^*} \left[\frac{z^* - \bar{s}}{s - z_G} \frac{\partial z_G}{\partial t'} - \left(\frac{z^*}{s - z_G} \right) \frac{\partial s}{\partial t'} \right]. \quad (26d)$$

In order to arrive at an equation for the vertical velocity in the z^* system, we note that since $\frac{da}{dt'} = \frac{da}{dt}$,

$$\frac{\partial a_i}{\partial t'} + u \frac{\partial a_i}{\partial x'} + v \frac{\partial a_i}{\partial y'} + w^* \frac{\partial a_i}{\partial z^*} = \frac{\partial a_i}{\partial t} + u \frac{\partial a_i}{\partial x} + v \frac{\partial a_i}{\partial y} + w \frac{\partial a_i}{\partial z}. \quad (27)$$

Then, substituting from eqs. 26 a-d, we find

$$w^* = w \frac{\bar{s}}{s - z_G} + \left(\frac{z^* - \bar{s}}{s - z_G} \right) \left(\frac{\partial z_G}{\partial t'} + u_i \frac{\partial z_G}{\partial x'_i} \right) - \left(\frac{z^*}{s - z_G} \right) \left(\frac{\partial s}{\partial t'} + u_i \frac{\partial s}{\partial x'_i} \right). \quad i = 1, 2 \quad (28)$$

In the experiments to be described, topography does not change in time, so that in eqs. 26d and 28, $\frac{\partial z_G}{\partial t} \equiv 0$. In order to treat the vertical component of eq. 11 in the z^* system, we substitute from eq. 25c to get

$$\frac{\partial \pi}{\partial z} = \frac{\partial \pi}{\partial z^*} \left(\frac{\bar{s}}{s - z_G} \right). \quad (29)$$

The horizontal pressure gradients are obtained by a technique to be described in the last section of this chapter. Since the horizontal

eddy diffusion terms are present more for the purpose of numerical smoothing than representation of the physics (see Pielke, 1975), it is assumed that

$$\frac{\partial}{\partial x_i} K_H \frac{\partial u_i}{\partial x_i} = \frac{\partial}{\partial x'_i} K_H \frac{\partial u_i}{\partial x'_i} \quad i = 1, 2$$

where

$$K_H = \alpha \Delta x \Delta y \left\{ \left(\frac{\partial v}{\partial x} + \frac{\partial u}{\partial y} \right)^2 + \frac{1}{2} \left[\left(\frac{\partial u}{\partial x} \right)^2 + \left(\frac{\partial v}{\partial y} \right)^2 \right] \right\}^{1/2}. \quad (30)$$

The values of K_z remain unchanged in the transformed co-ordinate system, since they are functions of dimensionless height. However, since the transformation of the diffusion terms in eq. 17 requires two applications of eq. 22b, we have

$$\frac{\partial}{\partial z} \left(K_z^{(m)} \frac{\partial u}{\partial z} \right) = \left(\frac{\bar{s}}{s-z_G} \right)^2 \frac{\partial}{\partial z^*} K_z^{(m)} \frac{\partial u}{\partial z^*}. \quad (31)$$

2.3 Turbulent Closure

The equations are formally closed by including equations for $K_z(z^*)$. This is assumed to be constant at $K_z = 1 \frac{\text{cm}^2}{\text{sec}}$ above the planetary boundary layer, and to have a linear profile in the surface layer:

$$K_z(z^*) = \frac{z^*}{h} K_z \text{ for } z^* < h \quad (32)$$

where h is the height of the surface layer. Between the planetary boundary layer and the surface layer, a Hermite interpolating polynomial is used to preserve continuity of second derivatives. This is displayed in Figure 1 and expressed by

$$K_z(z^*) = K_z(z_H) + \left(\frac{H-z^*}{H-h} \right) \left\{ K_z(h) - K_z(H) + (z^*-h) \left[\frac{\partial K_z}{\partial z^*} \right]_h + 2 \frac{K_z(h) - K_z(H)}{H-h} \right\}. \quad (33)$$

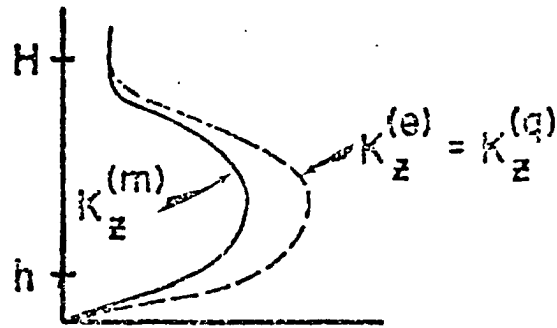


Figure 1 Schematic profile of the eddy exchange coefficients.

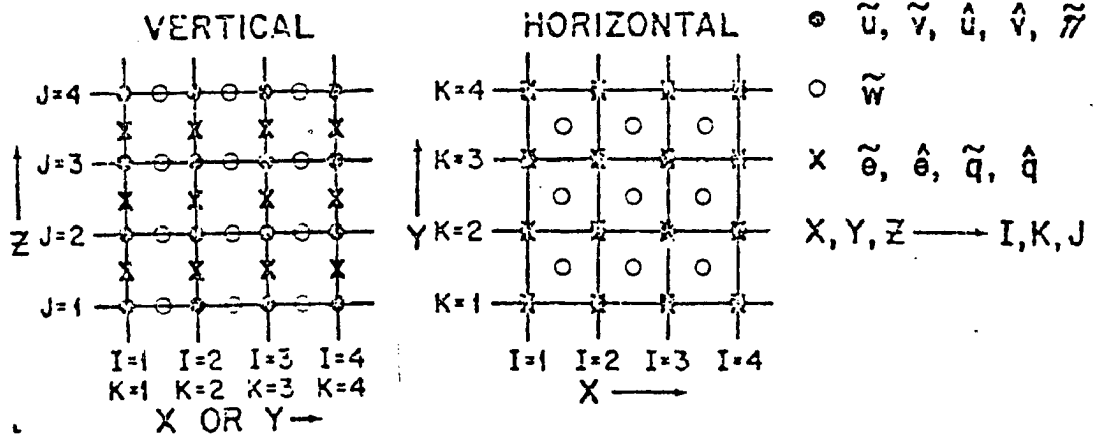


Figure 2 Schematic picture of model grid mesh.

The value of K_z at the top of the surface layer, and the heights of the surface and boundary layers are then all that are needed to solve for K_z . K_z at the top of the surface layer is given by

$$K_z^f(h) = \frac{kU_*h}{\phi_f(\zeta)} \quad \text{for } f = m, \theta, q \quad (34)$$

where h is taken to be $H/25$ in accordance with the findings of Blackadar and Tennekes (1968) for a neutrally stratified boundary layer. ζ is the dimensionless height z^*/L , where L is the Monin-Obukhov length:

$$L = \frac{\theta u_*^2}{kg\theta_*} \quad (35)$$

and k is von Kármán's constant. The dimensionless velocity, temperature and humidity gradients ϕ_f are taken from Yamamoto and Shiminuki (1966). u_* and θ_* are determined iteratively from

$$u_* = \frac{k(u^2 + v^2)^{1/2}}{(\ln(\frac{z}{z_0}) - \psi_1)} \quad i = 1, 2 \quad (36)$$

$$\theta_* = \frac{k[\theta - \theta(z_0)]}{[.74(\ln(\frac{z}{z_0}) - \psi_2)]} \quad i = 1, 2 \quad (37)$$

$$\zeta_0 = z_0/L$$

where z_0 is the surface roughness determined from:

$$z_0 = 0.032 u_*^2 / g \quad (\text{Clark, 1970}).$$

And the ψ 's are defined by

$$\psi_1 = \begin{cases} 2\ln[1+\phi_m^{-1}/2] + \ln[1+\phi_m^{-2}/2] - 2 \tan^{-1}\phi_m^{-1} + \frac{\pi}{2} & \text{for } \zeta \leq 0 \\ -4.7 & \text{for } \zeta > 0 \end{cases}$$

$$\psi_2 = \begin{cases} \ln[1+0.74 \phi_H^{-1}/2] & \text{for } \zeta \leq 0 \\ -6.35 \zeta & \text{for } \zeta > 0 \end{cases}$$

$$\text{and } \phi_m = \frac{kz}{u_*} \frac{\partial u}{\partial z}$$

$$\phi_H = \frac{kz}{\theta_*} \frac{\partial \theta}{\partial z}$$

u_* is constrained to be not less than

$$\frac{k(u^2 + v^2)^{1/2}}{2 \ln\left(\frac{z(1)}{z_0}\right)}$$

where u and v are evaluated at the lowest z^* level.

The height of the planetary boundary layer H is prognosed as a function of u_* , θ_* , and the potential temperature at the surface, θ_s . Following Deardorff (1974)

$$\frac{\partial H}{\partial t} = -u \frac{\partial H}{\partial x} - v \frac{\partial H}{\partial y} + w|_H + \frac{1.8[w_*^3 + 1.1 u_*^3 - 3.3 u_*^2 f_3 H]}{g \frac{H^2}{\theta_s} \frac{\partial \theta}{\partial z}|_{H^+} + 9.w_*^2 + 7.2u_*^2} \quad (38)$$

where w_* is zero for positive θ_* and

$$w_* = \left(\frac{-g}{\theta_s} u_* \theta_* z_*\right)^{1/3} \quad \text{for non-positive } \theta_*.$$

$\frac{\partial \theta}{\partial z}|_{H^+}$ is the vertical gradient of potential temperatures evaluated just above H .

Thus we see that the value of H is determined by:

1. Advection
2. Vertical Velocity at H (Deardorff cautioned that when convection is included, $w|_H$ should include the effects of cumulus-induced subsidence.)
3. w_* , u_* . Since these are functions of the low-level winds, H will be smaller over areas of calmer winds.

4. θ_s . As the surface heats, the planetary boundary layer will tend to deepen, in accordance with observation.

In an experiment comparing this formulation with an earlier formulation for H (viz. $H = .33 u_*^2 / f_3$) there was little change in vertical motion, but the values for H were quite different, being largest over heated convergence zones (Pielke and Mahrer, 1975) whereas the earlier formulation gave lower values of H in the convergence zone, because of the lower values of u_* . The new formulation was considered more physically reasonable, since one would expect a deeper planetary boundary layer in regions of mesoscale convergence. Pielke found, nevertheless, that the mean predicted w field was relatively insensitive to which formulation was used. He attributed this result to the rapidly developing surface heating function used, so that the heat flux quickly overwhelmed the stress contribution. He concluded that the prognostic method would be superior in less strongly forced simulations.

2.4 Finite Difference Techniques

In order to proceed with an integration of the equations expressed above, various boundary and initial conditions need to be considered. In addition, the forcing functions in the model (surface heating) and the space and time differencing operators need consideration.

To prevent unrealistic pressure anomalies, the height of the top surface of the model is allowed to vary in time and space. This height is obtained by integrating the continuity equation from the surface to the original height of the material surface and setting w^* to zero at top and bottom:

$$\frac{\partial s}{\partial t} = -\frac{1}{\bar{s}} \int_0^{\bar{s}} \left\{ \frac{\partial}{\partial x} [u(s-z_G)] + \frac{\partial}{\partial y} [v(s-z_G)] \right\} dz^* \quad (39)$$

π_i is obtained by integrating the hydrostatic equation downward from \bar{s} . The value of π_i at $z=\bar{s}$ is given by

$$\pi(\bar{s}, t) = \pi(\bar{s}, 0) - \frac{g}{\bar{\theta}} (s - \bar{s}) \quad (40)$$

where $\bar{\theta}$ is the average of the potential temperatures at s and \bar{s} .

At $z^*=0$, the boundary conditions are

$$u = v = w^* = 0$$

$$q = \text{constant}$$

$$\theta = \theta(t, z_G).$$

At $z^*=\bar{s}$, the boundary conditions are

$$u = u_{\text{synoptic}}$$

$$v = v_{\text{synoptic}}$$

$$w^* = 0$$

$$\theta = \text{constant.}$$

On lateral boundaries

$$w^* = \frac{\partial s}{\partial t} = \frac{\partial \theta}{\partial x_i} = \frac{\partial q}{\partial x_i} = \frac{\partial \pi}{\partial x_i} = 0 \text{ for } i = 1, 2 \text{ on } x_i \text{ boundary.}$$

Because of the upstream differencing method used,

$$\frac{\partial u_i}{\partial x_i} = \frac{\partial u_j}{\partial x_i} = 0 \text{ on } x_i \text{ outflow boundary; } u_i = u_{\text{synoptic}} \text{ on inflow}$$

boundary. Initial profiles of wind, potential temperature, and mixing ratio as well as surface values of pressure, potential temperature and mixing ratio are specified. Variables are staggered on the finite difference grid as shown in Figure 2.

Space differencing is done upstream for the advective terms while centered differencing is employed for diffusive and pressure gradient terms. The forward, upstream scheme on advection is well-known to be a numerically diffusive operator (Molenkamp, 1968). Pielke (1974) claims that for shallow systems and circulations changing slowly in time, such diffusion has advantages, such as dissipation of shorter wavelengths near the boundaries by the stretched grid system. Using the results of Jones (1973), computational stability is maintained by evaluating the equations in the order:

1. u, v
2. w
3. θ, q, π

This scheme is semi-implicit in the sense that the newly computed variables are used as soon as they are available. The time differencing operator is semi-implicit and forward in time. The semi-implicit character of operator is apparent in the finite difference analogue of eq. 31:

$$\left(\frac{\bar{s}}{s-z_G}\right)^2 \frac{1}{\Delta z_T} \frac{K_{j+1/2}}{\Delta z_1} (u_{j+1}^v - u_j^{v+1}) - \frac{K_{j-1/2}}{\Delta z_2} (u_j^{v+1} - u_{j-1}^v) \quad (41)$$

where the j subscripts indicate the model vertical level with midpoint values indicated by $j+1/2$. v indicates the time level and

$$\begin{aligned} \Delta z_1 &= z_{j+1}^* - z_j^* \\ \Delta z_2 &= z_j^* - z_{j-1}^* \\ \Delta z_T &= z_{j+1/2}^* - z_{j-1/2}^* . \end{aligned}$$

In order to compute the time tendencies, the $v + 1$ values of u must be moved to the left side of eq. 17a, resulting in

$$u_j^{v+1} = u_j^v + \Delta t \left\{ \frac{\left(\frac{\bar{s}}{s-z_G}\right)^2 \frac{1}{\Delta z_T} \frac{K_{j+\frac{1}{2}}}{\Delta z_1} u_{j+1}^v + \frac{K_{j-\frac{1}{2}}}{\Delta z_2} u_{j-1}^v + \text{other terms}}{1 + \Delta t \left(\frac{\bar{s}}{s-z_G}\right)^2 \frac{1}{\Delta z_T} \frac{K_{j+\frac{1}{2}}}{\Delta z_1} + \frac{K_{j-\frac{1}{2}}}{\Delta z_2}} \right\} .$$

The model is integrated over a grid containing 48 points in the direction, 42 in the y and 7 vertical levels. The horizontal grids have a spacing of 11 km in the interior and are stretched near the boundaries at the i th gridpoint according to the scheme:

$$x_j = x(i-1) + 55 \text{ km} - (i-2) \times 11 \text{ km} \quad 2 \leq i \leq 5$$

And similarly on other lateral boundaries. The vertical spacing is cubic and is given by

$$Z(I) = Z(1) \cdot I^3 \quad 2 \leq I \leq 7$$

The appropriate Courant-Friedrichs-Lewy stability criterion for a forward upstream scheme is

$$\Delta t \leq \frac{\sqrt{2}\Delta x}{C} ,$$

where C is the propagation speed of the disturbance. In order to leave a "margin of safety" the time step was taken as 20 sec. This will allow a propagation speed of approximately 777 m sec^{-1} , which is over a factor of two faster than any meteorological wave in the system.

Over south Florida, Pielke (1974) was able to compute horizontal pressure gradients along constant z levels. When the model is applied over uneven topography, horizontal pressure gradients can be calculated either by finding the gradient along the z^* surfaces

and adding a compensating term, or calculating the gradient along a true horizontal surface. Monin (1965) found that the former method introduces large truncation errors. In this model, the x and y gradients of pi are computed along the horizontal by determining the value of pi at the closest neighboring level which is below the altitude needed and calculating the pressure at this altitude hydrostatically upward according to

$$\frac{\partial \pi}{\partial z^*} = - \frac{s - z_G}{s} \frac{g}{\theta}$$

which is found by applying the "chain rule" to eq. 13. If the desired horizontal level is below the first grid point, pressure is figured hydrostatically downward.

3. NUMERICAL EXPERIMENTS

3.1 Introduction

The experiments which were performed were an attempt to discover what type of circulations could be induced by those forces simulated by the model. Of particular interest was the mountain upslope flow often observed in the mid-morning to afternoon hours (see, for example, Defant, 1951). Since the model is severely constrained by the static nature of the boundary conditions and by the scale of phenomena resolvable by the grid, it was hoped that some insight into the forcing mechanism of mountain upslope flow might be obtained.

Three experiments are discussed below. The first was quite idealized and was intended principally as a debugging aid, but is nevertheless discussed here because of certain facts it reveals about the behavior of the model. The other two experiments were attempts to simulate actual days. These days were chosen because of the relatively weak synoptic forcing which occurred, and because of the data available for comparison with model results.

3.2 Experiment A: "Witch of Agnesi" Topography

The so-called "Witch of Agnesi"¹ topography, described by

$$z_G = \frac{ah}{a^2 + r^2},$$

where a is the half-width, r is the distance from the center, and h is the height, was employed in one of these, to be called Experiment A. In this study, $h=3.5$ km and $a = 55$ km. The topography used for this experiment is shown in Figure 3. The initial wind field was directed radially outward from the center of the grid at a velocity of 1 m sec^{-1} . The Coriolis terms were set to zero for this experiment. Since there was no intention to simulate a real situation in this case, the heating function was started without any attempt to let the model reach a "steady-state". The heating function used was the same as that described below for Experiment B.

This experiment differs from the other two in that it is not intended to simulate a real case. The state of the model after five minutes of simulated time, when heating was begun is illustrated in Figure 4. A torroidal circulation seems to be characteristic of the initial conditions in the upper levels, with air generally

¹Miles & Huppert explain the origin of this term: "The curve . . . appears to have been studied originally by both Fermat and Grandi (Archibald & Court, 1964). Grandi designated it both versiora (because the curvature takes opposite signs) and, in a letter to Galileo (1718, p. 393), Versiera. Maria Agnesi studied it in her Instituzioni Analitiche (1748; see Colson 1801) and also designated it Versiera, a term that evidently has no direct translation but is similar to the Italian word avversoria, which has the first and second meanings adversary and devil. The Reverend John Colson (1801) appears to have opted for a feminine equivalent of the latter meaning and designated the curve Witch of Agnesi, by which name it is still known."

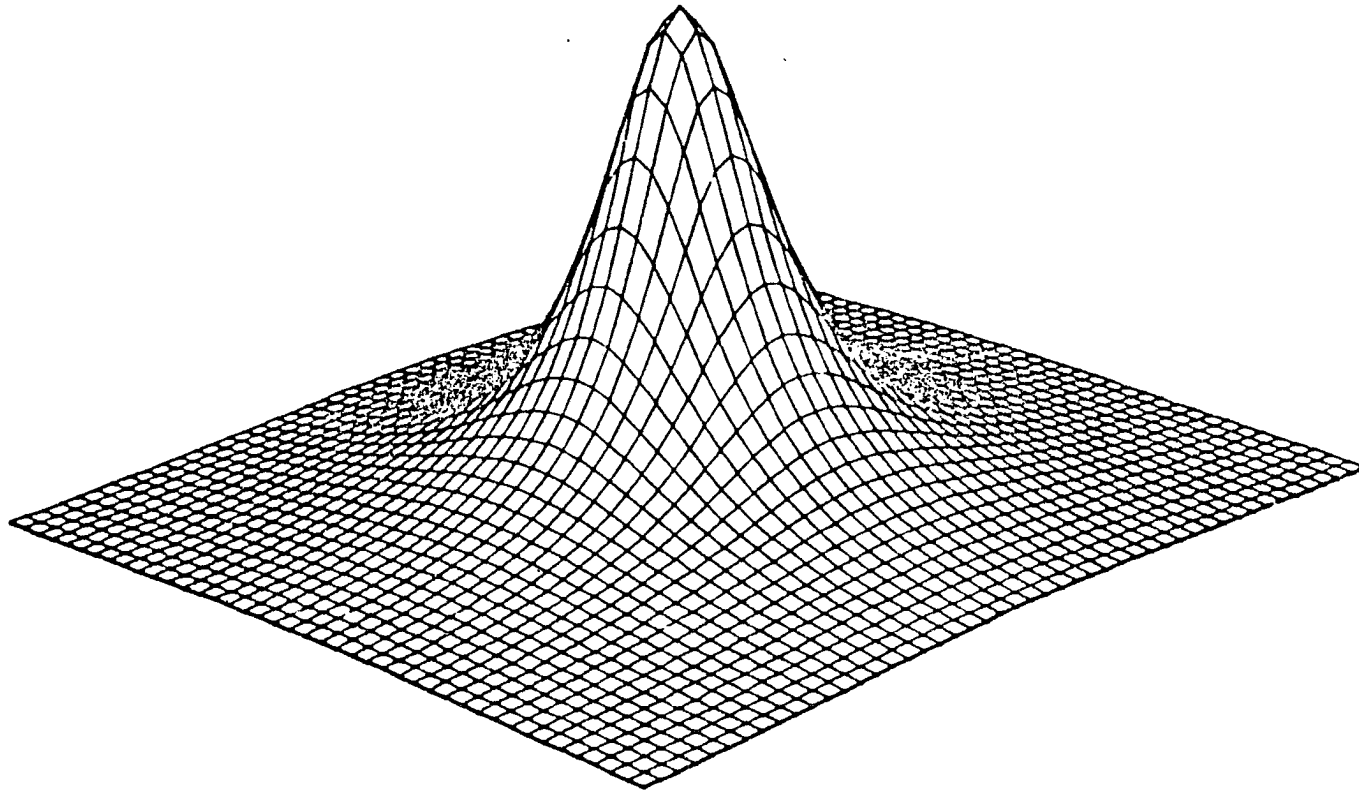


Figure 3 "Witch of Agnesi" topography (vertical scale is exaggerated).

34.9
VELOCITY(M/SEC)

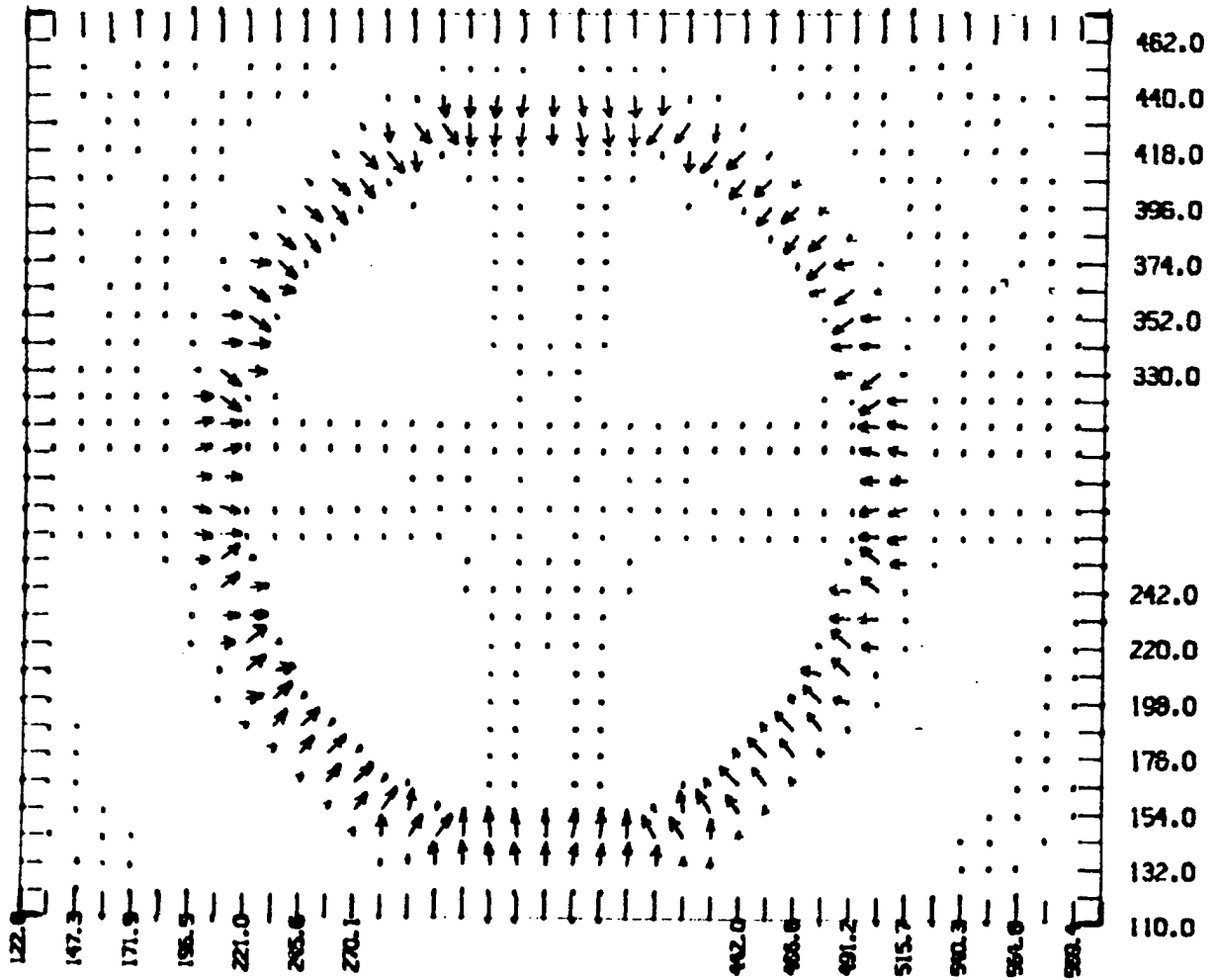


Figure 4 Vector plot of horizontal winds at interior grid-points on the $z^* = 0.03$ km surface at five minutes of simulated time. Axis labels are distances in kilometers east and north of the southwest corner of the model domain respectively. Unless otherwise noted, this and all subsequent plots of model output exclude the four gridpoint wide strip of constant topography near the perimeter.

descending over the peak and ascending at the edges. The second lowest z^* level contains the main outflow region induced by the peak area downdraft.

One disturbing feature of these results is the "quartered" nature of the flow. This is evident in the divergence and vertical velocities (Figures 5a-b) as early as five minutes into the integration. This feature lasts throughout the span of the integration. It was attributed to the influence of the boundaries. Since this experiment was completely symmetrical initially, the boundary conditions were identical on opposite sides. This type of four-celled division is not surprising for such reflective boundary conditions. This effect should be borne in mind when interpreting results from other numerical experiments. The asymmetrical nature of the flow in these experiments precludes any such obvious anomalies, but it is hoped that the stronger forcing imposed in the later experiments has relegated boundary "forcing" to a level which can be ignored.

After the heating function has been on for ten minutes (i.e. at $t = 15$) there is an indication of a secondary cell in the upper levels which consists of an updraft near the upper slope and a downdraft over the lower slope of the mountain, indicating that surface temperature changes can affect the entire depth of the model on a short time scale. It is marginally possible that information could be transmitted by advection/diffusion processes through the depth of the atmosphere in this amount of time, but it seems more reasonable to suspect that variations in the height of the material surface have induced these effects, particularly since

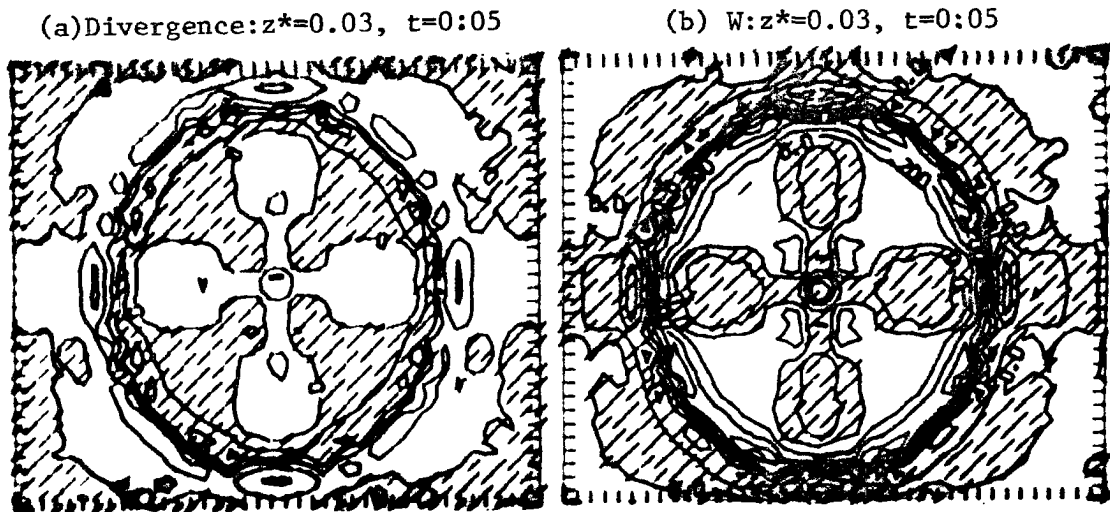


Figure 5 Contour plots at five minutes of simulated time on the $z^* = 0.03$ km surface of (a) divergence in sec^{-1} contoured from -0.4×10^{-3} to 0.2×10^{-3} in intervals of 0.1×10^{-3} (b) vertical velocity in m sec^{-1} contoured from -0.3 to 0.4 in intervals of 0.1 . In this and all subsequent contour plots, negative values are shaded.

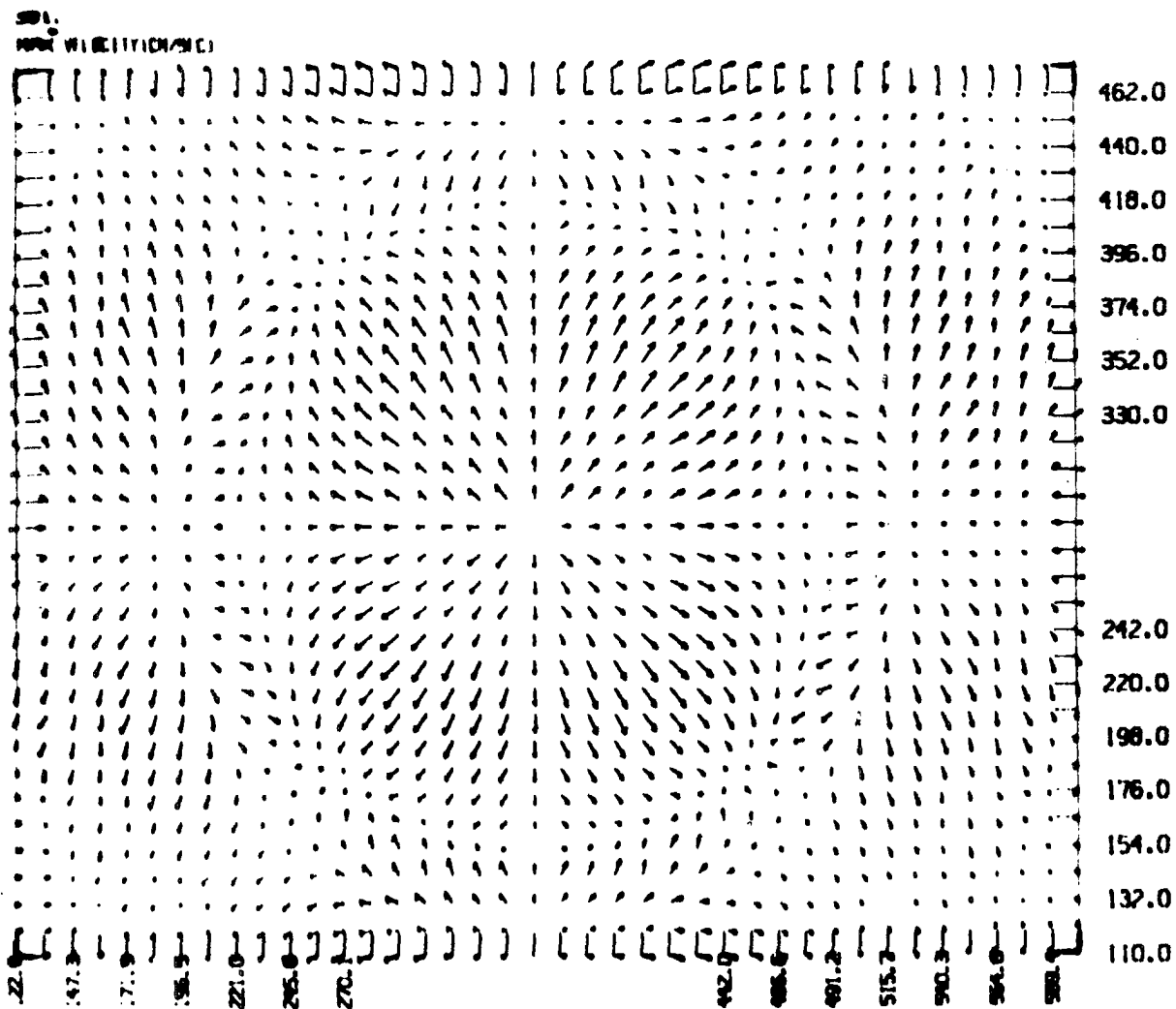
$z^* = 0.25, t = 0:15$


Figure 6

Vector plot of horizontal winds at interior grid-points on the $z^* = 0.25$ km surface at fifteen minutes of simulated time.

they seem to propagate downward in the model. The downdraft over the peak eventually reaches the lowest z^* level and by $t = 15$ (Figure 6) meets the upslope in a circular "front". By $t = 30$, the surface flow is entirely downslope. The $t = 30$ cross sectional plot (Figure 7) shows general lifting except for a mid-level column of subsidence over the peak. At this point in the heating function, most elevations are cooling, so it is not surprising that the basic flow at levels 1-5 is downslope. The return flow occurs primarily at levels four and six.

3.3 Experiment B: July 9, 1973 Simulation

Experiment B was an attempt to simulate conditions in eastern Colorado on July 9, 1973. The topography is displayed in Figures 8,9, and 10. Transparent overlays of Figures 9 and 10 are provided to assist in interpretation of later illustrations. The elevation of topography on a strip along the perimeter of the domain, five gridpoints wide was held constant as an aid in eliminating boundary noise.

This day was chosen because it was an experimental day of the National Hail Research Experiment (NHRE) for which extensive documentation was available (see Fankhauser, 1976, and Chalon, Fankhauser, and Eccles, 1976). This day was also suitable since there was little synoptic activity in the region (which because of the constant boundary conditions, the present model is not able to simulate). The wind profile which was used is displayed in Figure 11. This profile represents a subjective composite of the winds reported from the 0500 LST soundings at Denver, Grand Junction, Grover, and Sterling, and was intended to represent the synoptic-scale situation

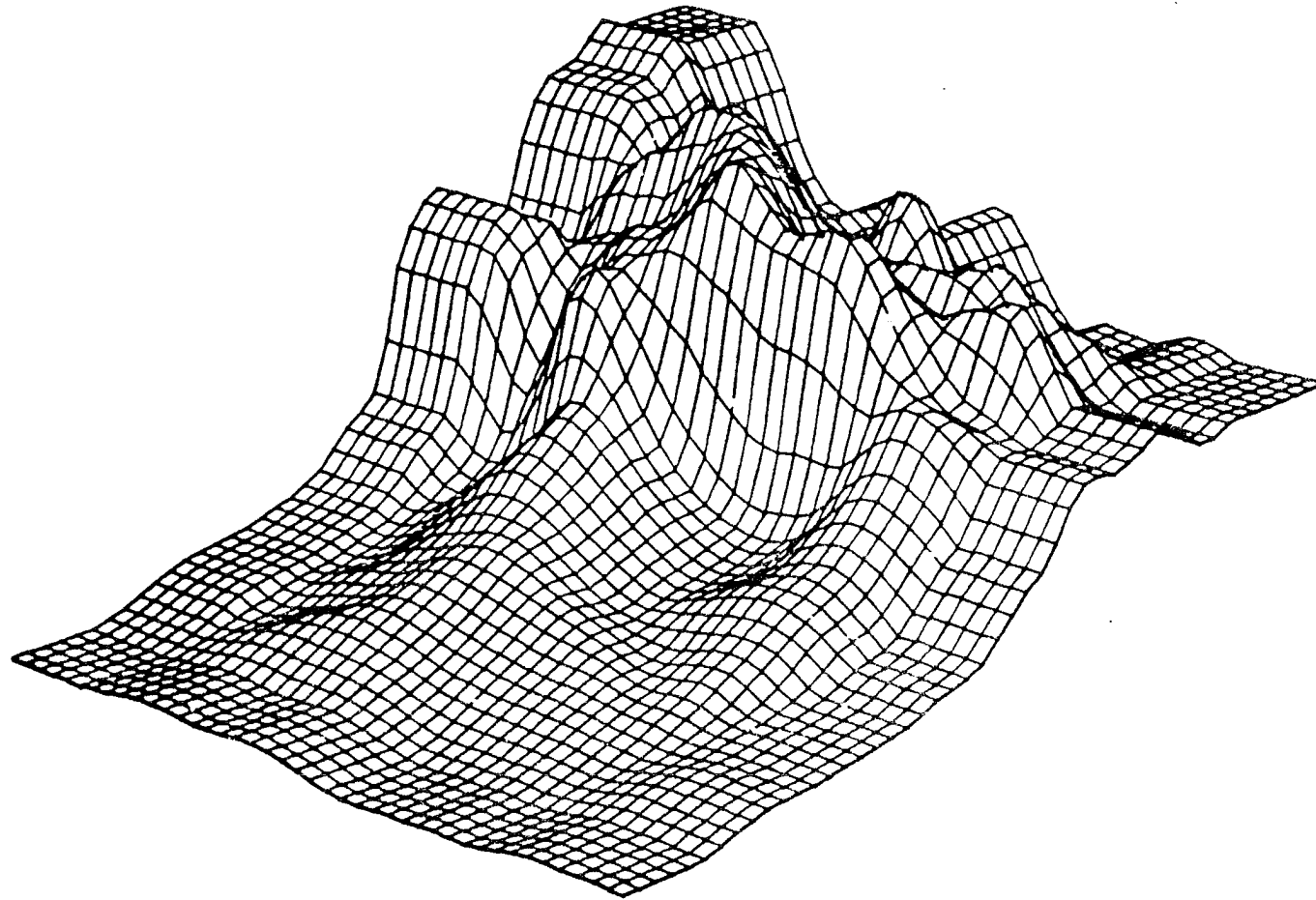


Figure 8 Topography for Experiments B and C viewed from the north-east corner of the domain (vertical scale is exaggerated).

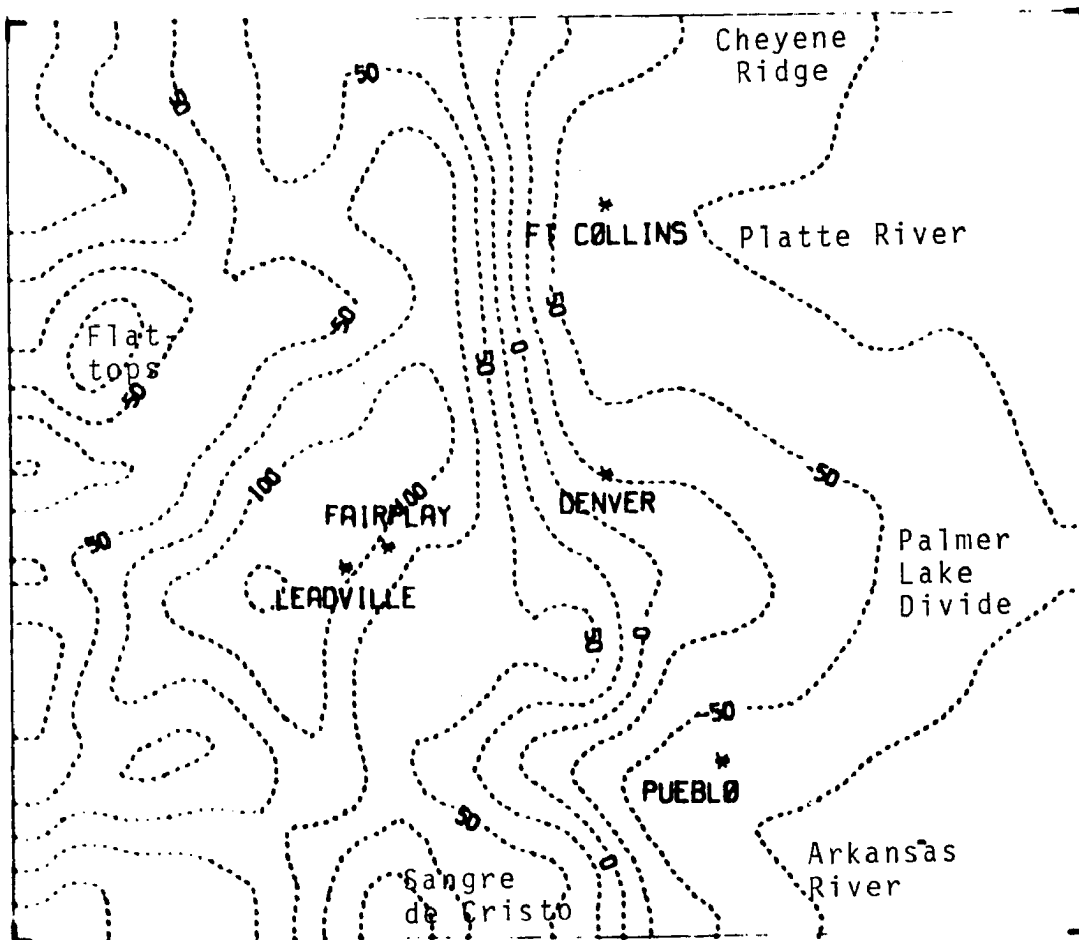


Figure 9 Contour plot of deviation of topography from average value used in Experiments B and C, contoured from -750 m to 1250 m in intervals of 250 m. Transparent overlays of this figure are provided.

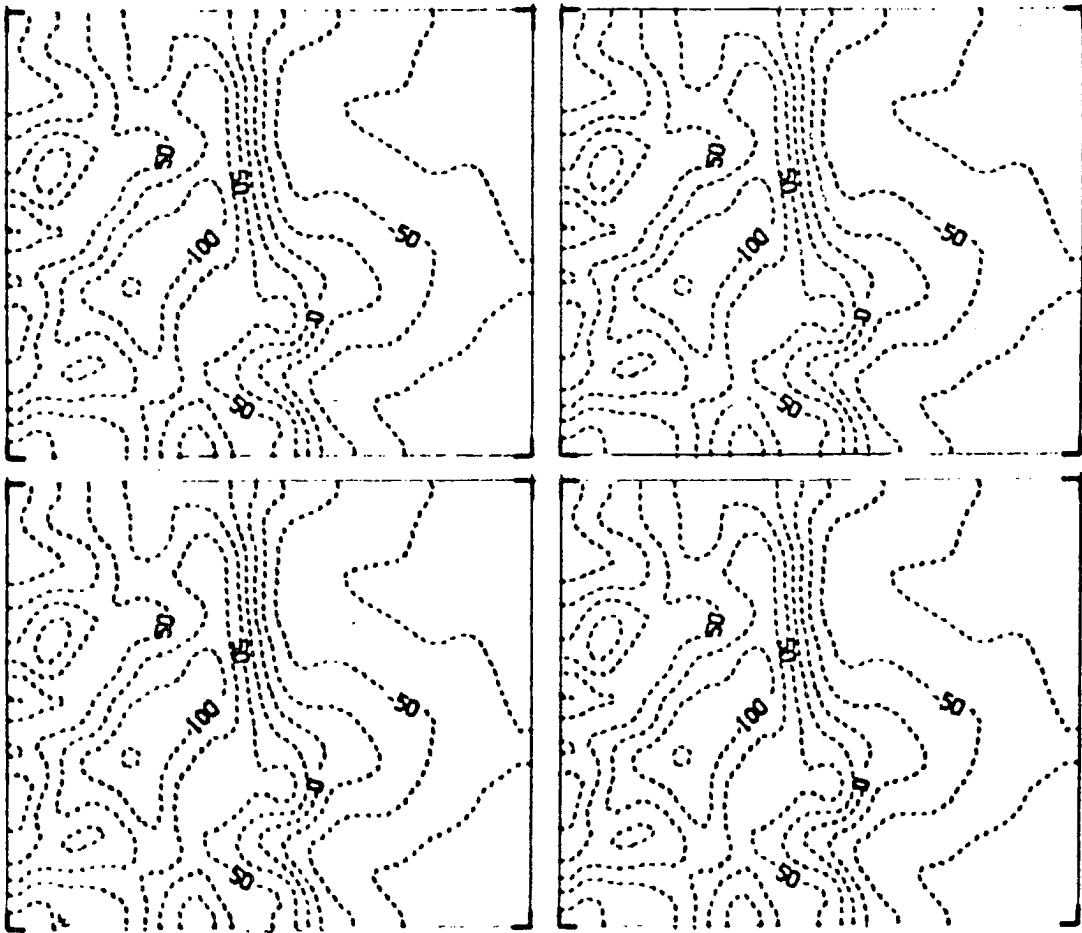


Figure 10 Contour plots of deviation of topography from the average value, used in Experiments B and C, contoured from -750 m to 1250 m in intervals of 250 m. Transparent overlays of this figure are provided.

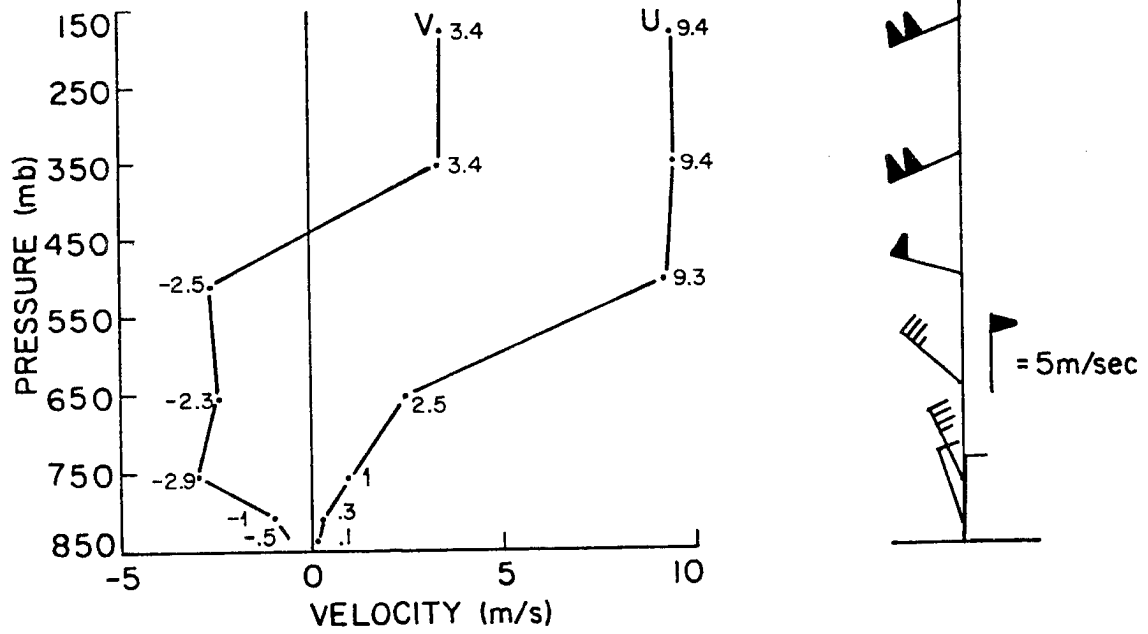


Figure 11 Initial winds used for Experiment B.

at that time. Winds in the lowest three layers of the model, which remain below the planetary boundary layer for most of the integration, are light and from the north-northwest. Winds back through the middle and upper layers and increase in speed to about 10 m sec^{-1} .

The definition of the profile of potential temperature presents a more difficult problem. Because of the complex topography over the experimental area, no single sounding was representative. It is difficult to see how a suitable composite sounding should be constructed. There are few data concerning the variation of theta with height over complex terrain. The SPACE (see Danielson and Cotton, 1977) provided an opportunity to compose cross-sectional views of theta from Grand Junction to Goodland, Kansas. The results were quite variable and therefore not definitive. Since storage and time constraints demanded a simple initialization, the approximation which appeared to be most consistent with the data was that theta surfaces should be initially horizontal. The Denver sounding was used for this purpose. The initial mixing ratio was assumed to be constant on the z^* surfaces. While this is certainly not accurate, since q serves only as a tracer, there are no significant dynamic consequences of this choice. This should be born in mind when viewing the advection of q , however. The Denver 0500 LST sounding is shown in Figure 12. This sounding shows the usual morning inversion. It is about 2 kPa deep and represents about 2.5° K difference. Above this, the atmosphere is generally adiabatic or very slightly stable, except for the area from about 50 kPa to about 34 kPa, which is almost moist adiabatic to 40 kPa and quite stable above that. The inversion occurring at about 25 kPa

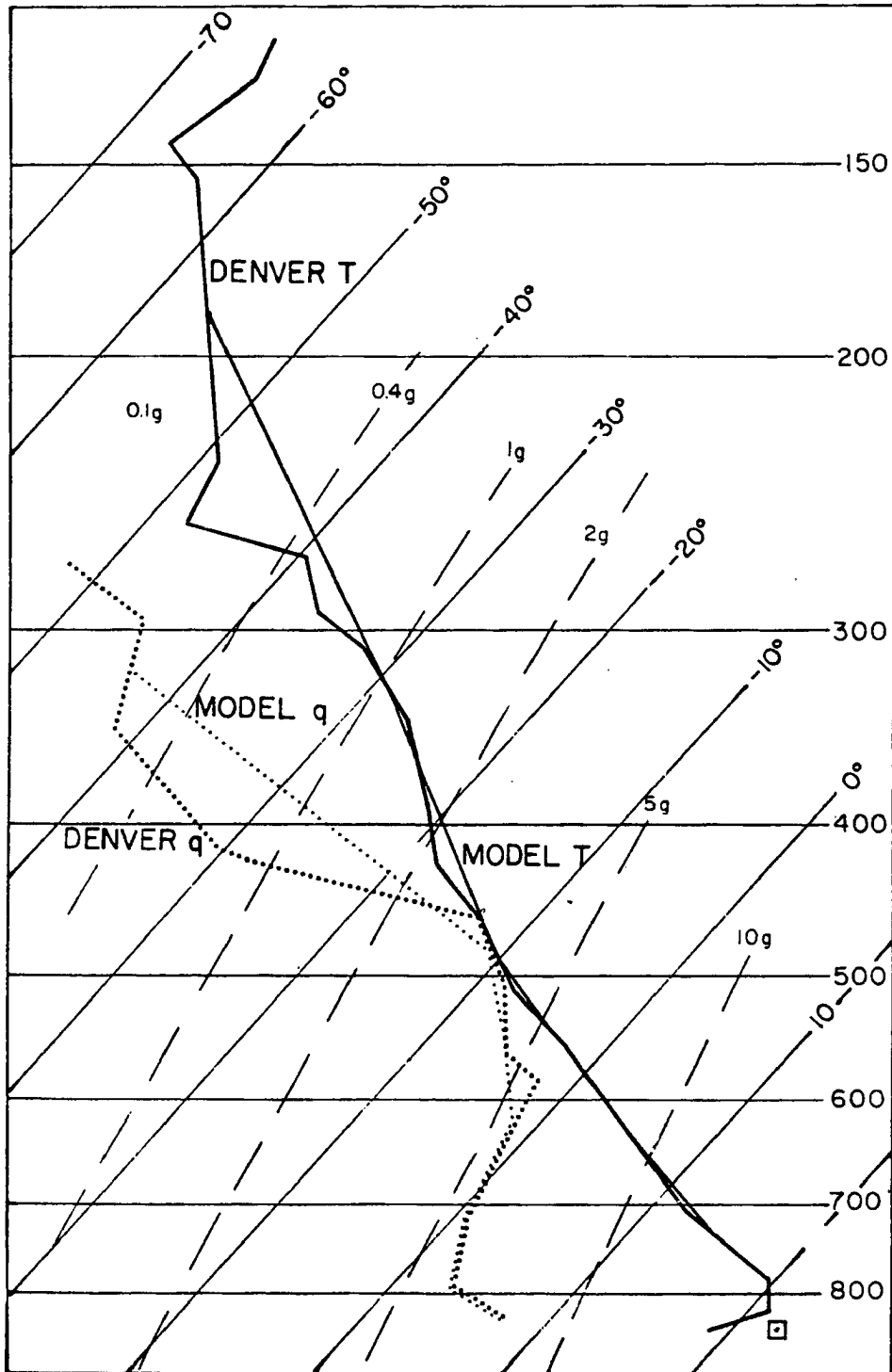


Figure 12 Skew-T, log-P plot of the thermodynamic sounding taken at 0500 LST on July 9, 1973 at Denver, and of the sounding used in the model for Experiments A and B. The boxed point shows how the morning inversion was removed.

is not resolved by the model. The lifting condensation level (LCL) was 72 kPa for the sounding. However, in the experiment the surface inversion was removed by using the surface temperature value indicated in Figure 12 by the boxed point. This effectively raised the LCL to 68 kPa. This compares favorably with the LCL of 65 kPa found for the NHRE representative sounding for this day which was taken at Sterling, Colorado at 1630 MDT.

Circulations in the model are forced by a heating function which specifies the surface potential temperature in time at given elevations. A surface energy budget model would be desirable except that a number of uncertainties arise because of the effects of variable ground cover which make the level of effort of such a modeling project beyond the scope of this work. A surface temperature "wave" has therefore been constructed which is a function of time and elevation. The shape of the curve for Experiment B was taken from Kuo (1968) who based his empirical curve on data taken in O'Neil, Nebraska. The phase, amplitude, and maximum temperature of the wave have been expressed as a function of elevation in such a way as to match data which were available for the day in question. These data and the surface temperature curves produced by the model are shown in Figure 13. The fit is far from exact, and there are, of course, no slope direction considerations. It should be noted that the effective "morning" is unrealistically long. However, this would be expected to have more effect on the timing of the resulting circulations than on their qualitative nature. It will be noted that the

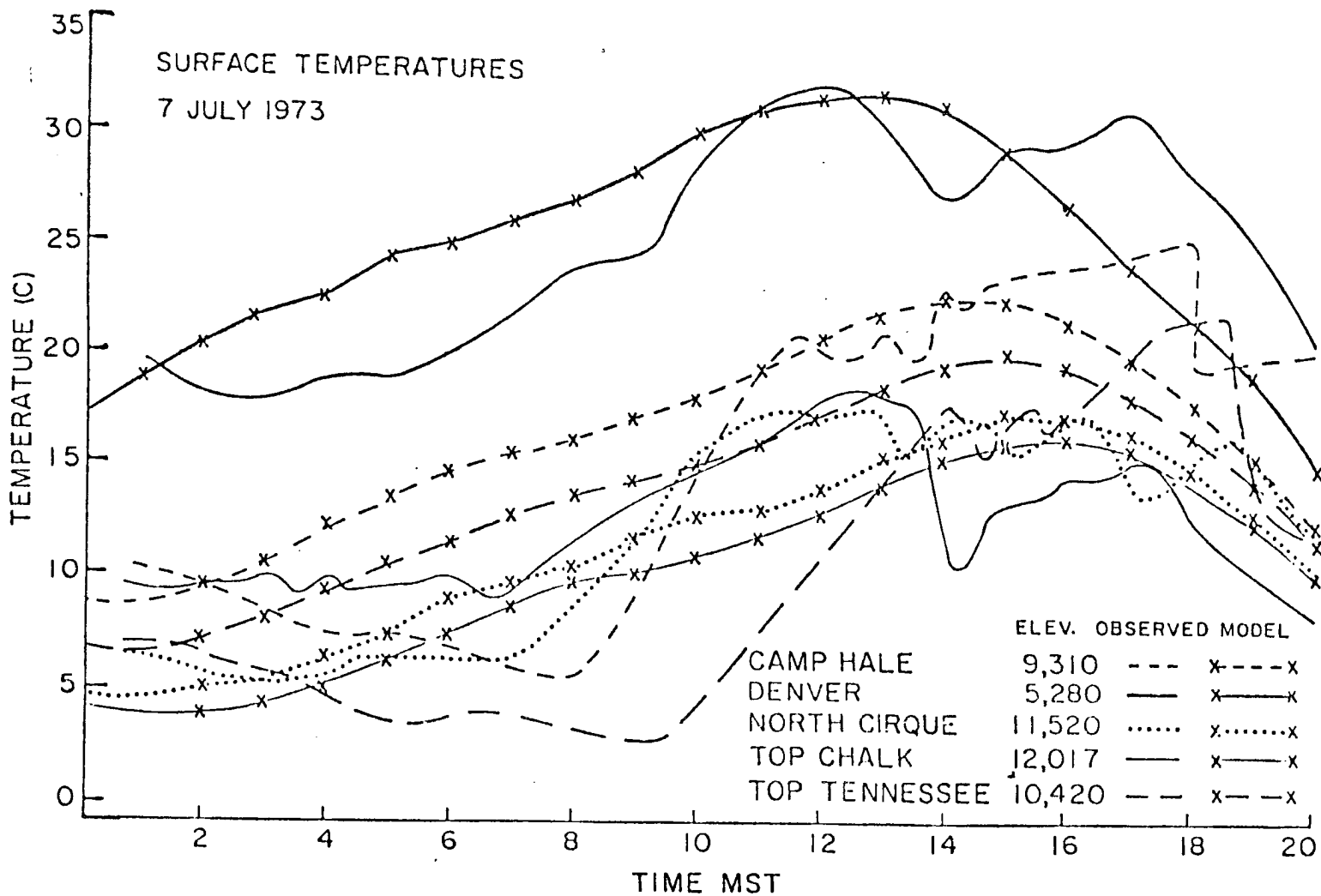


Figure 13 Observed and modeled surface temperatures for five locations within the model domain at various elevations for Experiments A and B.

lower elevations reach their maximum temperature about two and one half hours before the highest elevations. Further, the lower elevations have a larger range (about 15° C) than higher elevations (which have about a 10° C range), and, of course, a higher average temperature. Using this method, an east-facing slope has the same temperature as a west-facing slope, even during the morning when a solar-facing slope experiences enhanced heating. After the model has reached a quasi-steady state, the surface thetas are changed linearly in time over a period of 100 time steps in such a way as to produce the proper "starting" theta at each grid point.

Figure 14 shows the total kinetic energy in the model for each of the three experiments. This provided the basis for the declaration of "steady state", as discussed previously. The absolute values of the average kinetic energies are, of course, related to the strength of the initial winds. In both the last two experiments, it can be seen that strong fluctuations in energy damp out within about six hours of simulated time, and it is supposed that this represents the adjustment of the model to a change in forcing. A smaller perturbation is seen in both experiments when the surface begins to cool (at about 13 hours simulated time).

Although an attempt was made to choose a day which was not strongly forced by the large scale, the behavior of the wind over the experimental area determined from the NWS maps for the day was dominated by the movement of an inverted trough which at 0500 LST on July 9 was stretched from northeast New Mexico into western Kansas. There was a weak surface high pressure area which,

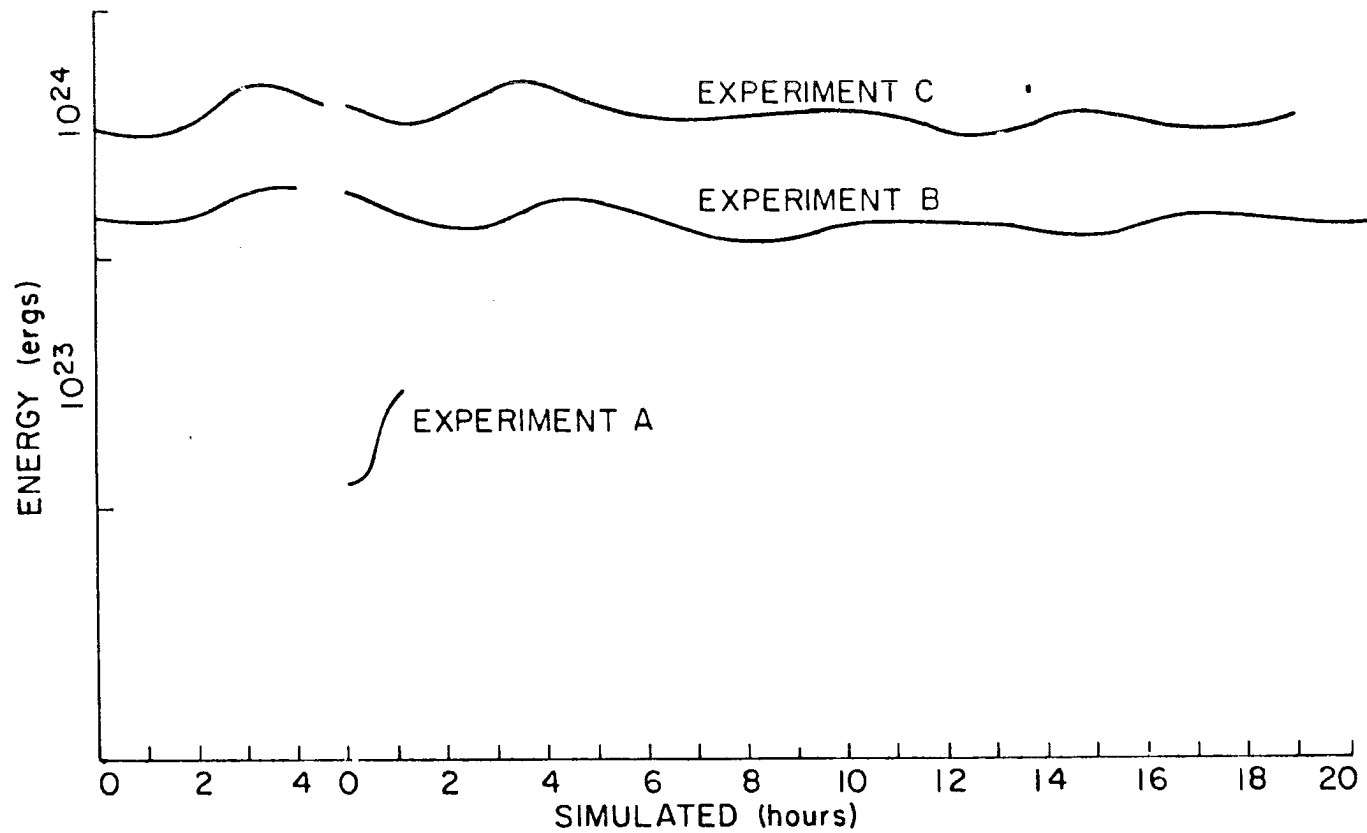


Figure 14 Semi-logarithmic plot of total kinetic energy in the model for each of the experiments during initialization and simulation.

as the day progressed, increased in strength and moved southeastward (Figure 15). Simultaneously, the low pressure area moved eastward. This caused the winds both at the surface and aloft to shift in a clockwise manner and gain an upslope component. As is usual for the area, there was a moisture gradient increasing eastward. Northeast Colorado experienced confluence near the surface and divergence aloft in the afternoon (Chalon, et al) which was associated with the development and southward movement of several "multi-cell" hail storms over the NHRE area.

The flow pattern which was predicted at the time that quasi-steady state was assumed, i.e., when the heating function was begun, persisted in its major features throughout the integration, changing only in the magnitude of the flow and, particularly over the plains, in its spatial location. The heating function was started at 0100 LST. In the lowest three layers, which initially all lie below the planetary boundary layer, areas of relative topographic maxima were characterized by a lower planetary boundary layer, by divergence, and by negative vertical velocity (Figure 16a-c). Topographic minima showed opposite effects. The boundary layer at this time ranged from 0.4 km to about 1.3 km. Divergence varied from -0.3×10^{-3} to 0.3×10^{-3} , creating vertical velocities of $\pm 0.4 \text{ m sec}^{-1}$ in the lowest layers. At the fourth level, the lowest level which is above the planetary boundary layer, the vertical velocity patterns over the mountainous regions are similar to the lower patterns, while over the plains convergence occurs over topographic maxima and divergence over minima (Figure 17a-b). At the fifth level, $z^* \approx 4 \text{ km}$, the divergence

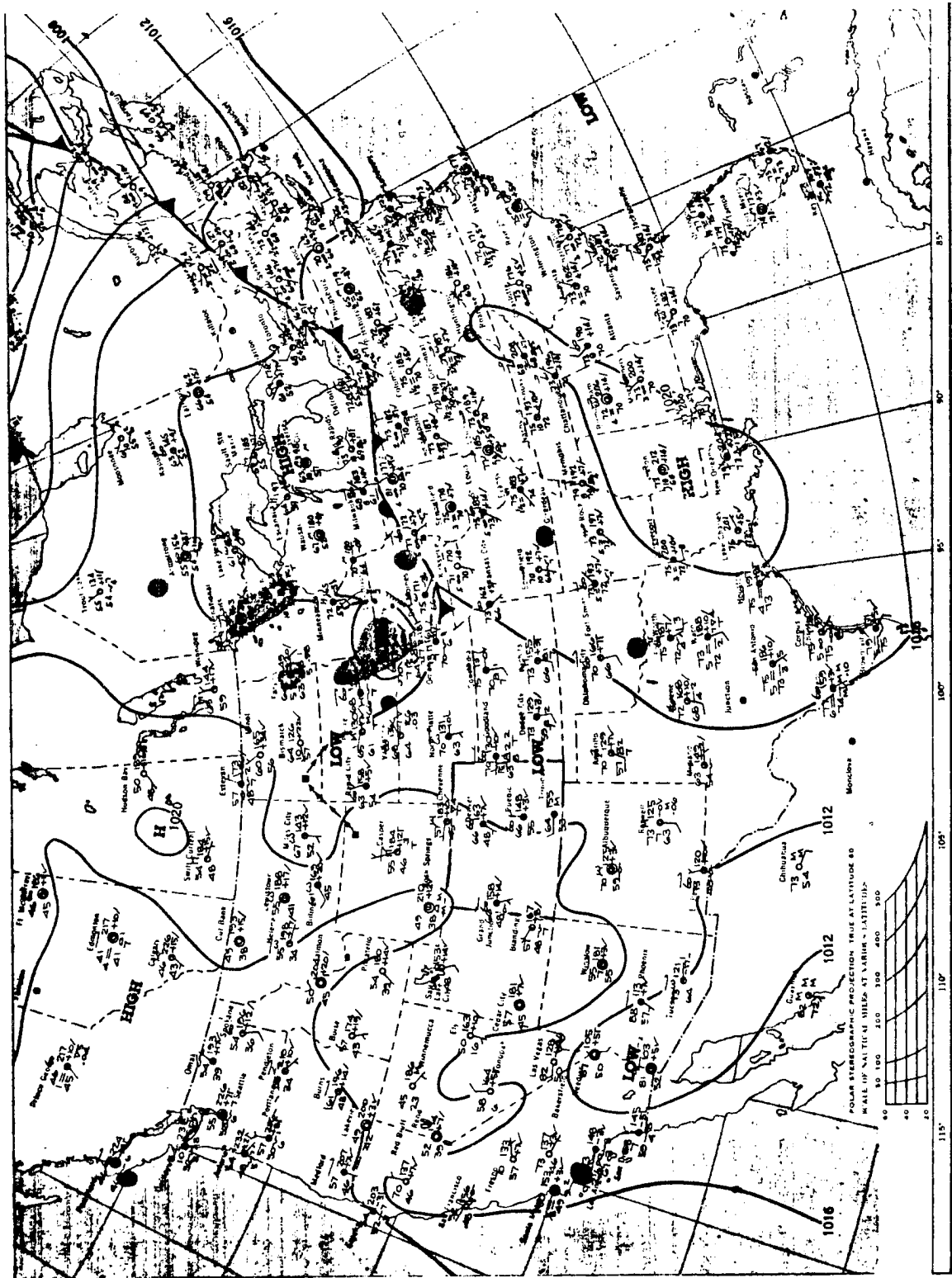
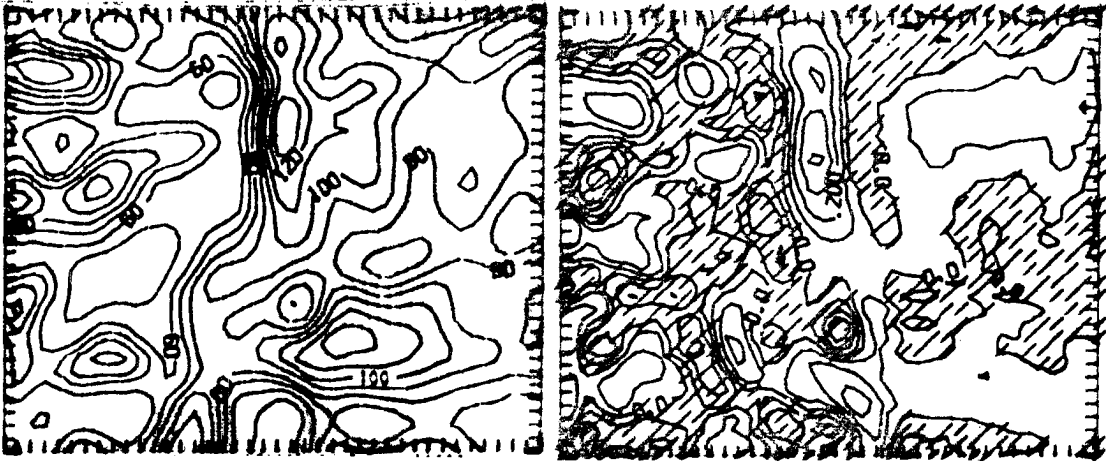


Figure 15 Surface weather map for the United States at 0500 LST on July 9, 1973.

(a) H: t=2:30

(b) w: z*=0.03, t=2:30



(c) Divergence: z*=0.03, t=2:30

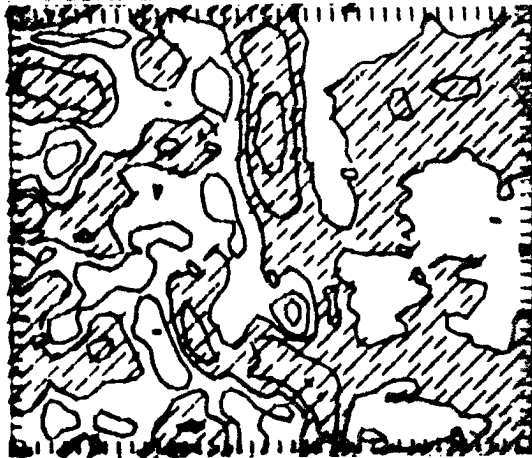
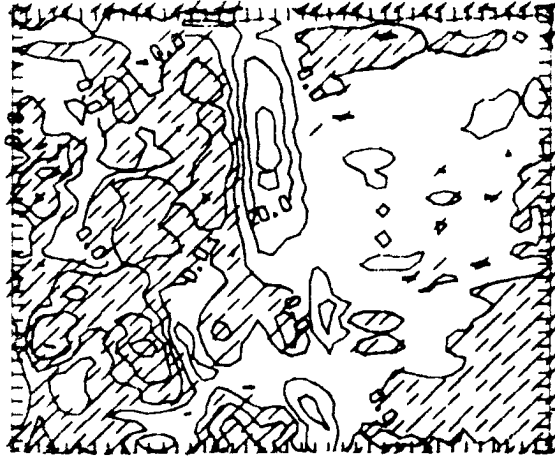


Figure 16

Contour plots at 0230 LST of (a) the height of the planetary boundary layer in decameters contoured from 40 to 130 in intervals of 10 (b) vertical velocity at $z^* = 0.03$ km in m sec^{-1} contoured from -0.4 to 0.4 in intervals of 0.1 (c) divergence at $z^* = 0.03$ km in sec^{-1} contoured from -0.2×10^{-3} to 0.3×10^{-3} in intervals of 0.1×10^{-3} .

(a) w : $z^*=2.0$, $t=2:30$



(b) Divergence: $z^*=2.0$, $t=2:30$

(c) Divergence: $z^*=4.0$, $t=2:30$

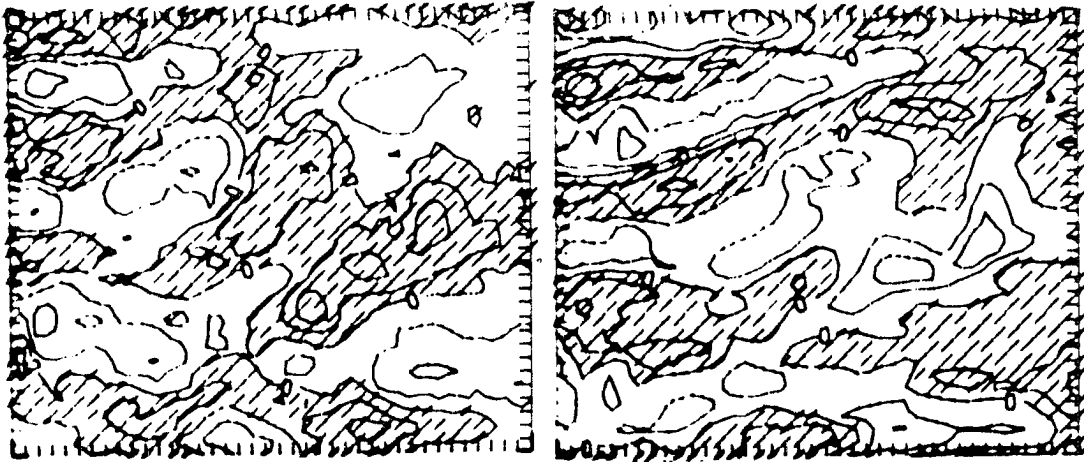


Figure 17 Contour plots at 0230 LST of (a) vertical velocity at $z^* = 2.0$ km in $m \text{ sec}^{-1}$ contoured from -3.0 to 3.0 in intervals of 1.0 (b) divergence in sec^{-1} at $z^* = 2.0$ km contoured from -1.6×10^{-3} to 1.6×10^{-3} in intervals of 0.8×10^{-3} (c) divergence in sec^{-1} at $z^* = 4.0$ km contoured from -0.2×10^{-3} to 0.2×10^{-3} in intervals of 0.1×10^{-3} .

pattern is again reversed, showing a similarity to the lowest layers. At this level, however, one can note in the divergence plot (Figure 17c) an organization of divergence into east-west oriented bands. These seem to be related to topographic extrema which, by chance, are loosely oriented in this manner. Thus, at this level, the divergence seems to be more strongly affected by relative topographic features than absolute elevations. The sixth level of the model shows relatively small changes in space and time. This type of flow is indicative of a downslope regime. Some of the lower level divergence patterns may be related to the tendency of the flow to split around peaks and channel up valleys, particularly the Colorado River Valley (Figure 18), creating areas of divergence and convergence respectively.

It will be noted that the flow shown in Figure 18 is very different from the low-level winds used to initiate the model (Figure 11). Indeed this flow which forms the effective initial conditions for the model shows almost no similarity to the winds observed at this time, thus making comparisons with observations difficult and perhaps irrelevant. At this point in the model development, comparisons with climatological data might be most useful.

In his analysis of mean NHRE soundings, Wetzel (1973) found levels of significant discontinuity of wind, temperature, and moisture features at 74 kPa (about 1.25 km above the surface) and at 54 kPa (about 3.6 km above the surface). These were presumed to correspond to the heights of the planetary boundary layer and a mechanical boundary layer frictionally mixed as air crosses the

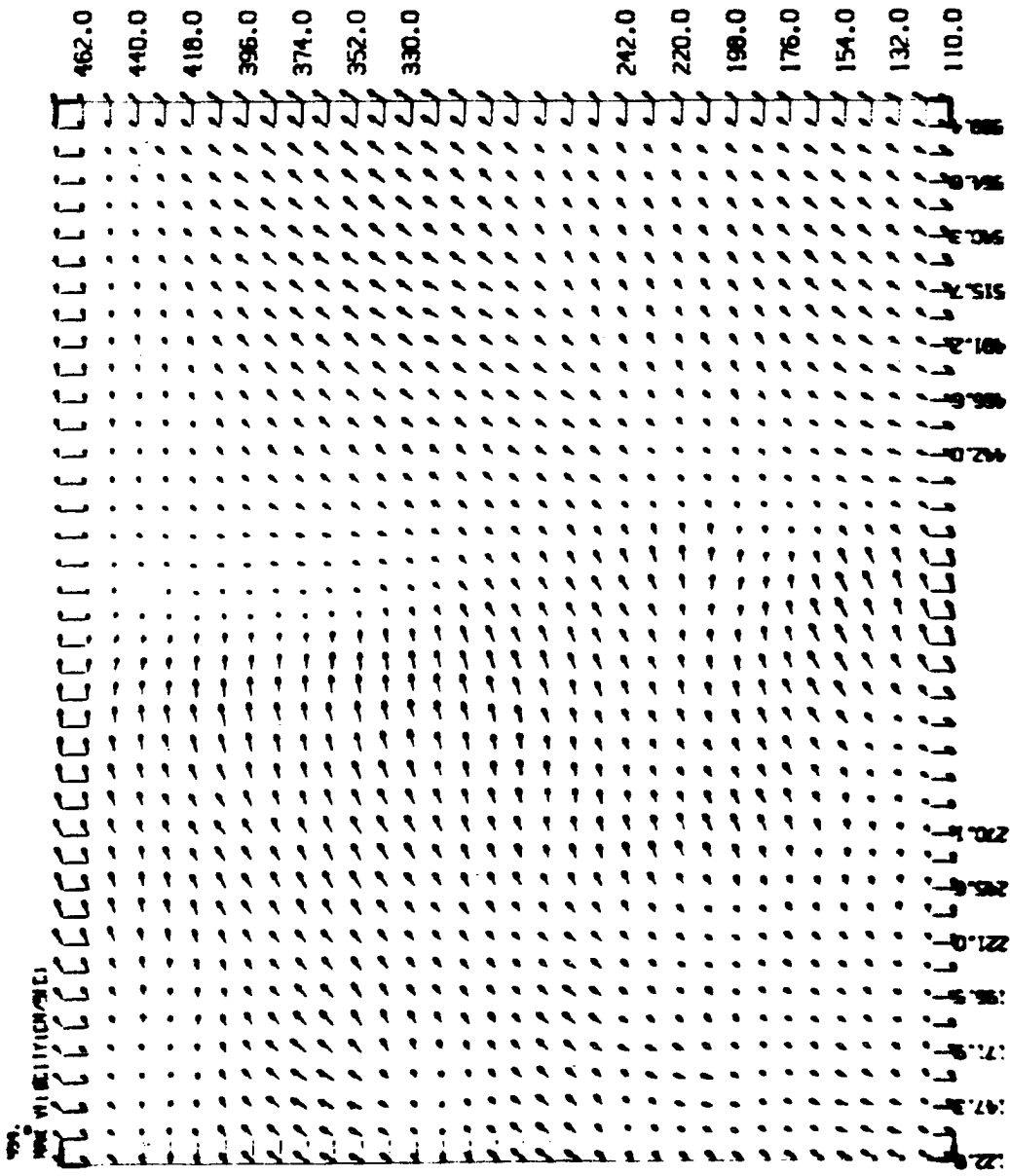


Figure 18 Vector plot of horizontal winds at interior grid-points on the $z^* = 0.03$ km surface at 0330 LST.

mountains. The model indicates that there is a flow discontinuity between 0.8 km and 2.0 km and between 2.0 km and 4.0 km. The first of these probably corresponds to the top of the planetary boundary layer. The second seems to agree well with the findings of Wetzel, but caution should be exercised since a similar discontinuity can be seen in Experiment A, which has very different topography and mixing characteristics.

A striking feature of both this experiment and Experiment C is the north-south oriented strip of convergence and positive vertical velocity which lies approximately between Ft. Collins and Denver. This can be seen in Figure 19a to correspond to a very deep planetary boundary layer. A similar feature is found in the Arkansas River Valley near the mountains. It would appear that the strong convergence regions are induced by steep gradients of topography (Figure 19b). The opposite effect can be seen in peaks with steep slopes. This suggests that the vertical velocity is affected by the vertical divergence taking place on lee slopes.

The moisture field is initially drier over the mountains and relatively moist over areas of positive vertical velocity. As the integration proceeds, the moisture gradients generally smooth out until about noon, with some drying occurring above the planetary boundary layer (Figure 20a-d). Because the initial moisture is almost constant in layers 2-4, it is difficult to trace the origin of moisture gradients in these layers. Wetzel (1973) found in his study of NHRE data that there was an early afternoon increase in moisture above the planetary boundary layer, particularly on dry days. One of the sources he postulated for this increase was

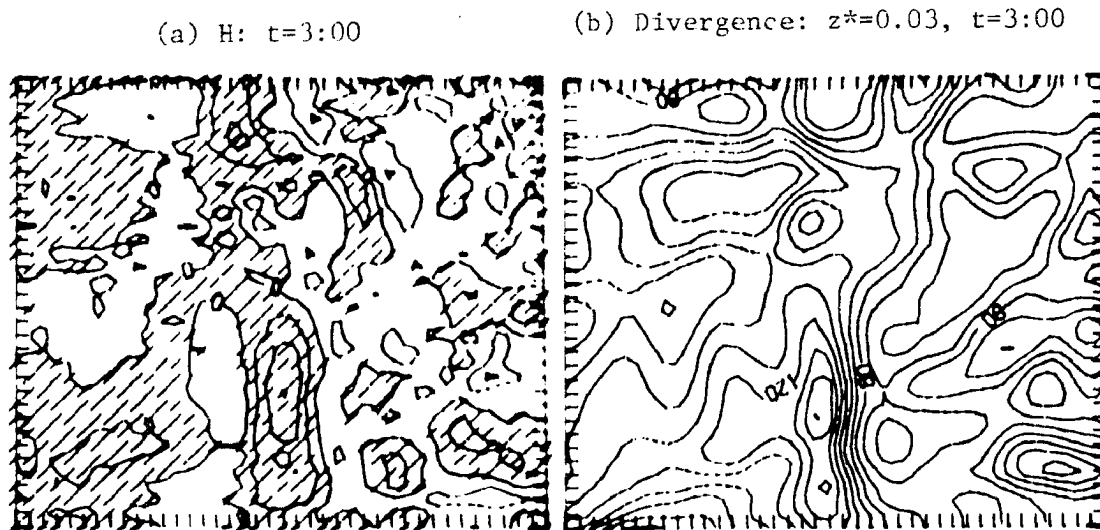


Figure 19 Contour plots at 0300 LST on the $z^* = 0.03$ km surface of (a) the height of the planetary boundary layer in decameters contoured from 50 to 150 in intervals of 10 (b) divergence in sec^{-1} contoured from -0.24×10^{-3} to 0.16×10^{-3} in intervals of 0.8×10^{-4} .

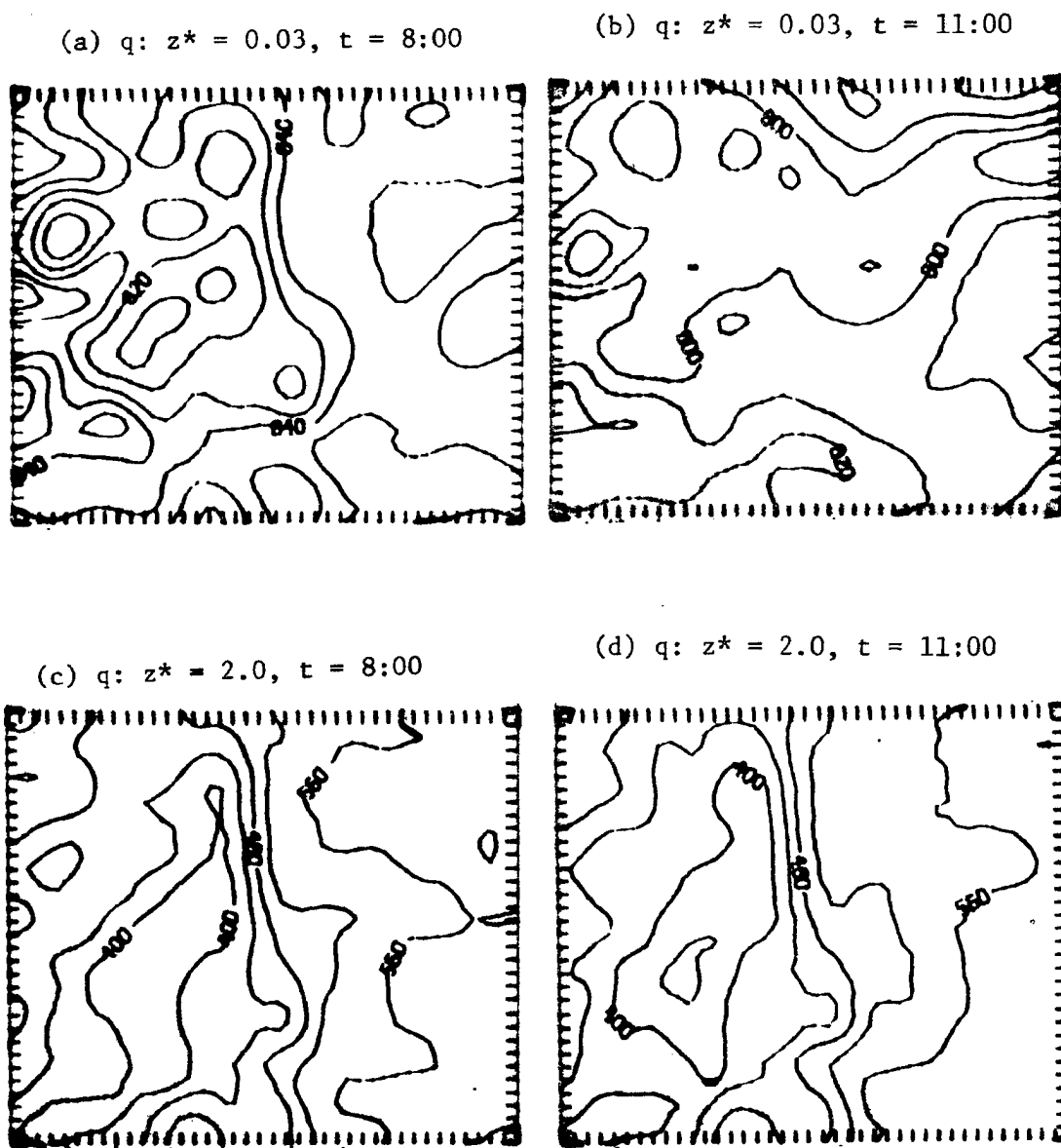


Figure 20

Contour plots of mixing ratio in grams metric ton^{-1}
 (a) at 0800 LST on the $z^* = 0.03$ km surface
 contoured from 800 to 860 in intervals of 10
 (b) at 1100 LST on the $z^* = 0.03$ km surface
 contoured from 770 to 820 in intervals of 10
 (c) at 0800 LST on the $z^* = 2.0$ km surface
 contoured from 360 to 560 in intervals of 40
 (d) at 1100 LST on the $z^* = 2.0$ km surface
 contoured from 320 to 600 in intervals of 40.

mountain evapo-transpiration. He calculated that this would account for about 20% of the increase, if distributed between 74 and 25 kPa and that, if confined to a smaller depth, "its effect could be decisive". The model contains no provision for this source, and an increase of 20% over several hours would certainly reverse the drying trend.

At 0630 LST, one can note a trend for deepening of the planetary boundary layer throughout the domain, presumably from the flux of heat from the surface. Also at this time, one can see an eastward movement and expansion of the region of negative vertical velocity which lies east of the Denver-Ft. Collins line (Figure 21a-c). This is associated with a large increase in convergence in this area (Figure 21d). Eastward propagation of lines of convection have been noted in this region. The study by Wetzel (1973) employs a radar climatology to show this, so that the propagation is not seen until clouds have developed sufficiently to produce echoes. The mean initiation time is about 1300 LST. The fact that this and several other episodes of propagation occur in the model indicate that this propagation may be aided by processes not requiring the release of latent heat.

The flow appears to be connected with local topographic features over the plains, as opposed to being dominated by the mountain-plains differences. Above the planetary boundary layer, the velocity of the flow along the plains ridges shows a definite maximum of about 11 m sec^{-1} . An hour later, the negative vertical velocity band is reforming east of the Denver-Ft. Collins line (Figure 22a-c). This is associated with a decrease in divergence.

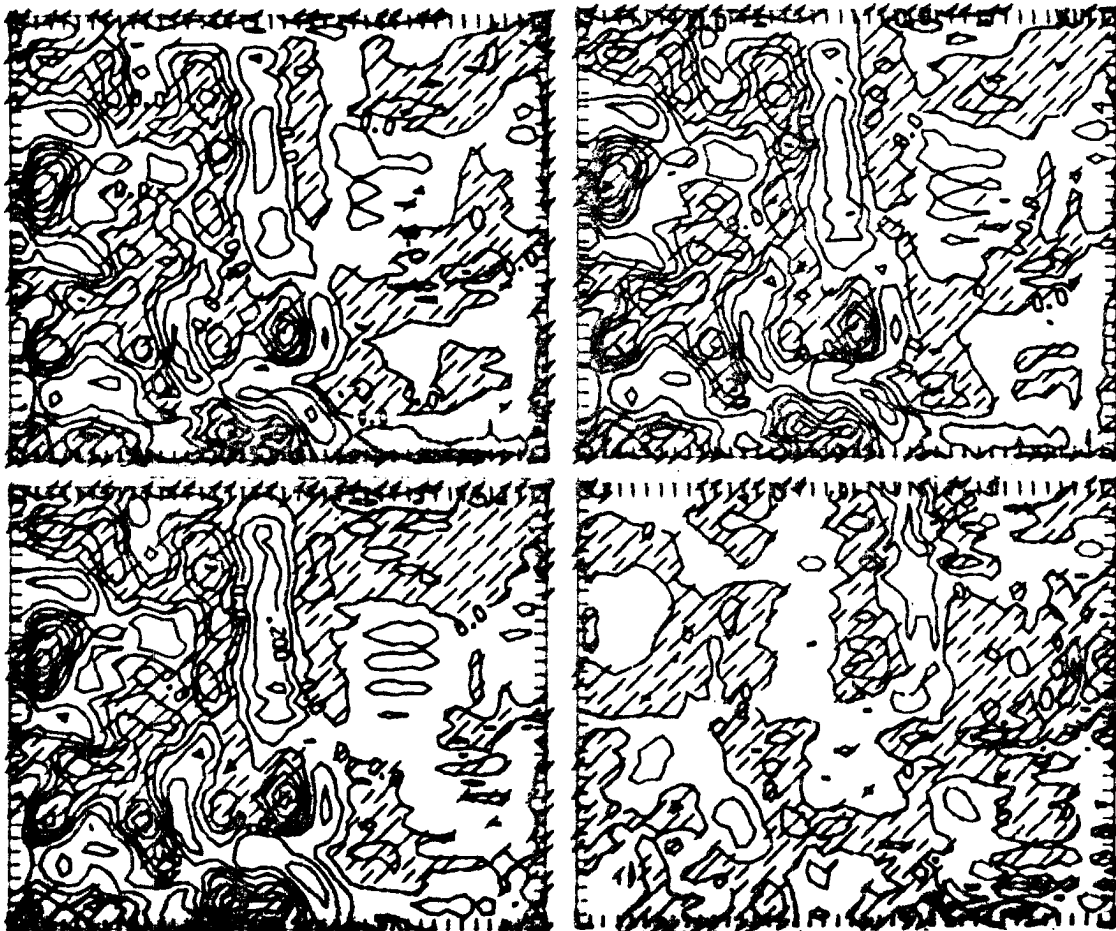
(a) $w: z^* = 0.03, t = 5:30$ (b) $w: z^* = 0.03, t = 6:00$ (c) $w: z^* = 0.03, t = 6:30$ (d) Divergence change: $z^* = 0.03$

Figure 21 Contour plots on the $z^* = 0.03$ km surface of vertical velocity in m sec^{-1} contoured from -0.5 to 0.3 in intervals of 0.1 at (a) 0530 LST (b) 0600 LST (c) 0630 LST and of (d) the thirty minute change in divergence at 0600 LST in sec^{-1} contoured from -0.6×10^{-4} to 0.6×10^{-4} in intervals of 0.3×10^{-4} .

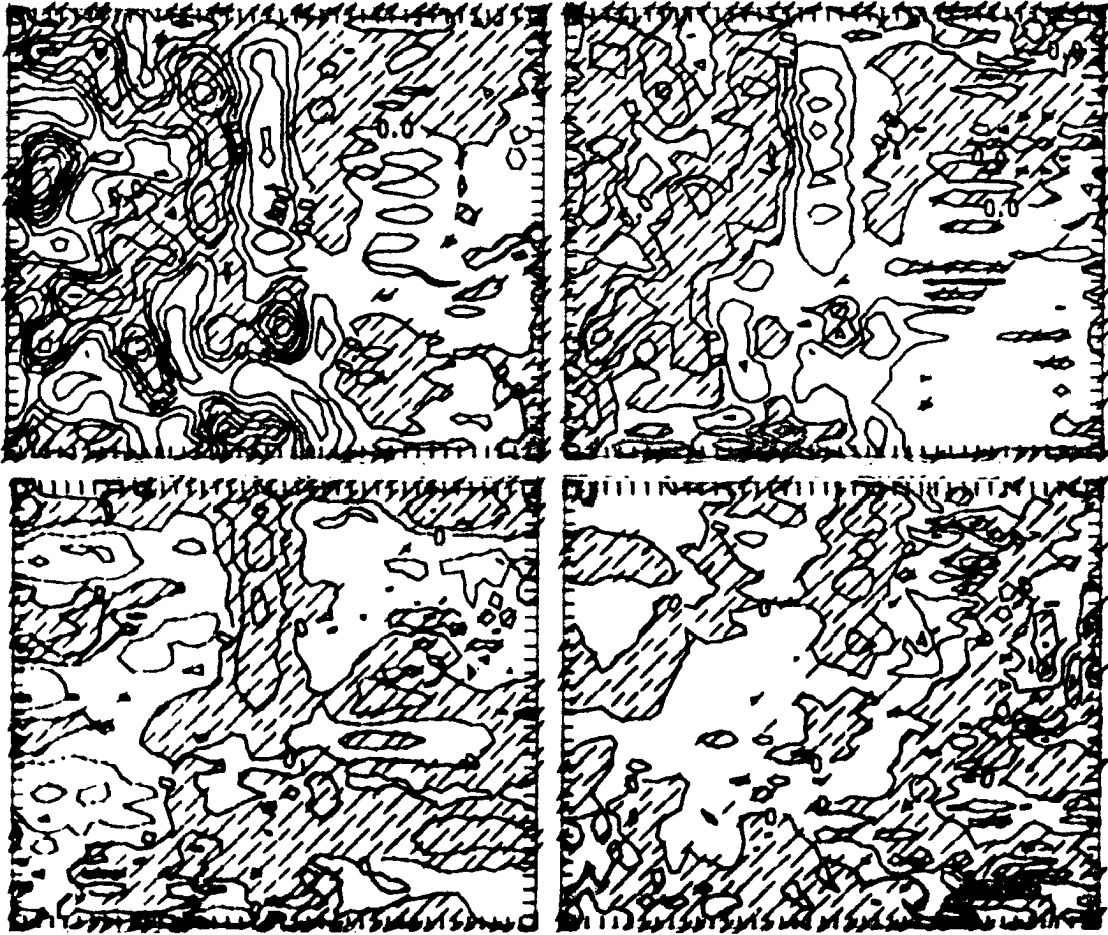
(a) w : $z^* = 0.03$, $t = 7:00$ (b) w : $z^* = 2.0$, $t = 8:30$ (c) Divergence: $z^* = 2.0$, $t = 8:30$ (d) Divergence Change: $z^* = 0.03$

Figure 22

Contour plots of (a) vertical velocity in m sec^{-1} at 0700 LST on the $z^* = 0.03$ km surface contoured from -0.5 to 0.3 in intervals of 0.1 (b) vertical velocity in m sec^{-1} at 0830 LST on the $z^* = 2.0$ km surface contoured from -3.0 to 3.0 in intervals of 1.0 (c) divergence in sec^{-1} at 0830 LST on the $z^* = 2.0$ km surface contoured from -0.14×10^{-3} to 0.14×10^{-3} in intervals of 0.7×10^{-4} (d) the thirty minute change in divergence in sec^{-1} at 0700 LST on the $z^* = 0.03$ km surface contoured from -0.9×10^{-4} to 0.6×10^{-4} in intervals of 0.3×10^{-4} .

Most of the area over the mountainous regions in the lowest layers is showing an increase in divergence. However, the highest peaks in this area are showing a decrease (Figure 21d). This is understandable, since the lower elevations heat sooner and more strongly than higher elevations. It is interesting that the positive vertical velocity west of the Denver-Ft. Collins line extends throughout the depth of the model, while the associated convergence exists only through the $z^* = 2.05$ km level. This north-south line seems to induce a series of vertical velocity lines in the lowest level over the plains. This is much less evident at the next level. The series of lines takes on a two-celled or roll character. This type of circulation was also noted by Dirks (1969) and Wetzel (1973). Dirks related it to the lee precipitation minimum and was able to show numerically that it is forced in a two dimensional model by the slope of the great plains.

The north-south line of positive vertical motion east of Ft. Collins which can be seen in Experiment C as well (see Section 3.4), coincides approximately with an area which often produces lines of afternoon thundershowers. This area of active convection was noted by Henz (1974) and showed a mean initiation time for radar echoes of about 1500 MDT. The east-west oriented convergence patterns noted earlier in the $z^* = 4$ km level now begin to influence the 2.05 km level (Figure 22c).

At 0830 LST, the enhanced vertical velocity along the Denver-Ft. Collins line has propagated southward and displays some "cell" structure. The magnitude of the vertical circulation has not changed appreciably from the initial conditions, maintaining

values ranging from -0.3 m sec^{-1} to 0.3 m sec^{-1} . Since the wavelength of the cells is the same as the grid-spacing (Figure 23), one cannot place a great deal of confidence in the numerical representation of these features, but the results suggest that there is a tendency to concentrate energy on scales smaller than the grid-spacing. Below the planetary boundary layer, the convergence area over the Platte River Valley spreads out in area and increases in magnitude. Above the planetary boundary layer, the divergence is increasing. Both above and below the boundary layer, winds over these areas are turning from north-northwest to northwest.

The observed winds at 0800 LST were generally weak and unorganized at the surface, but did experience a general clockwise turning of about 20° at most stations. This was probably associated with the synoptic situation discussed above. The low-level convergence and availability of moisture caused morning cloud cover to develop over the plains as seen in the ATS-3 0922 LST satellite imagery for the day (Figure 24a). The circulations predicted by the model could be significantly altered if radiation changes caused by this cloud cover could be incorporated in the surface heating function.

At 1030 LST, one notes another predicted occurrence of the eastward propagation of the negative vertical velocity region (Figure 25a-c). Nothing similar can be found over the mountainous areas, where the circulation seems to be tied to the topography. The magnitude stays relatively constant at $\pm 0.3 \text{ m sec}^{-1}$. Above

(a) w : $z^* = 0.03$, $t = 8:30$

(b) w : $z^* = 0.03$, $t = 9:30$

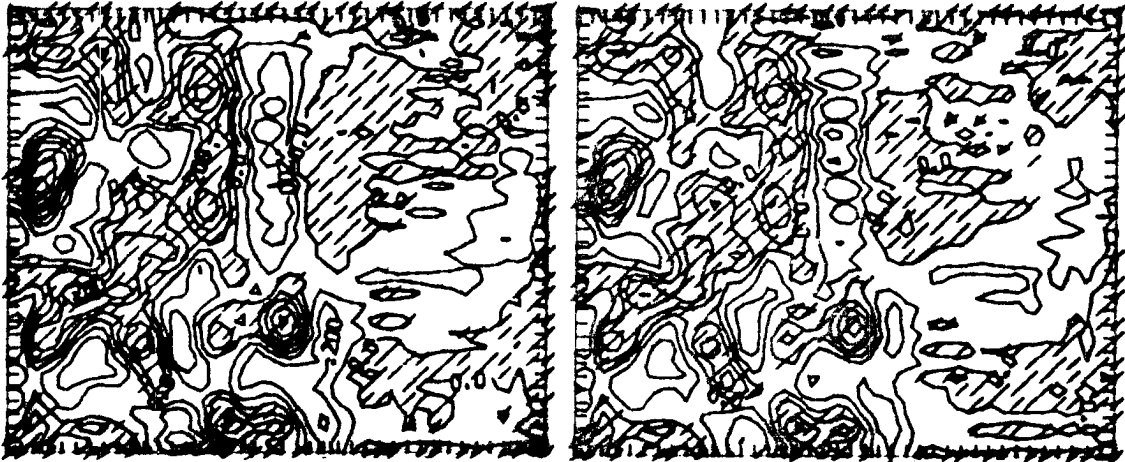


Figure 23

Contour plots on the $z^* = 0.03$ surface of
(a) vertical velocity at 0830 LST contoured from -0.5 to 0.3 m sec^{-1} in intervals of 0.1 m sec^{-1}
(b) vertical velocity in m sec^{-1} at 0930 LST contoured from -0.4 to 0.3 in intervals of 0.1

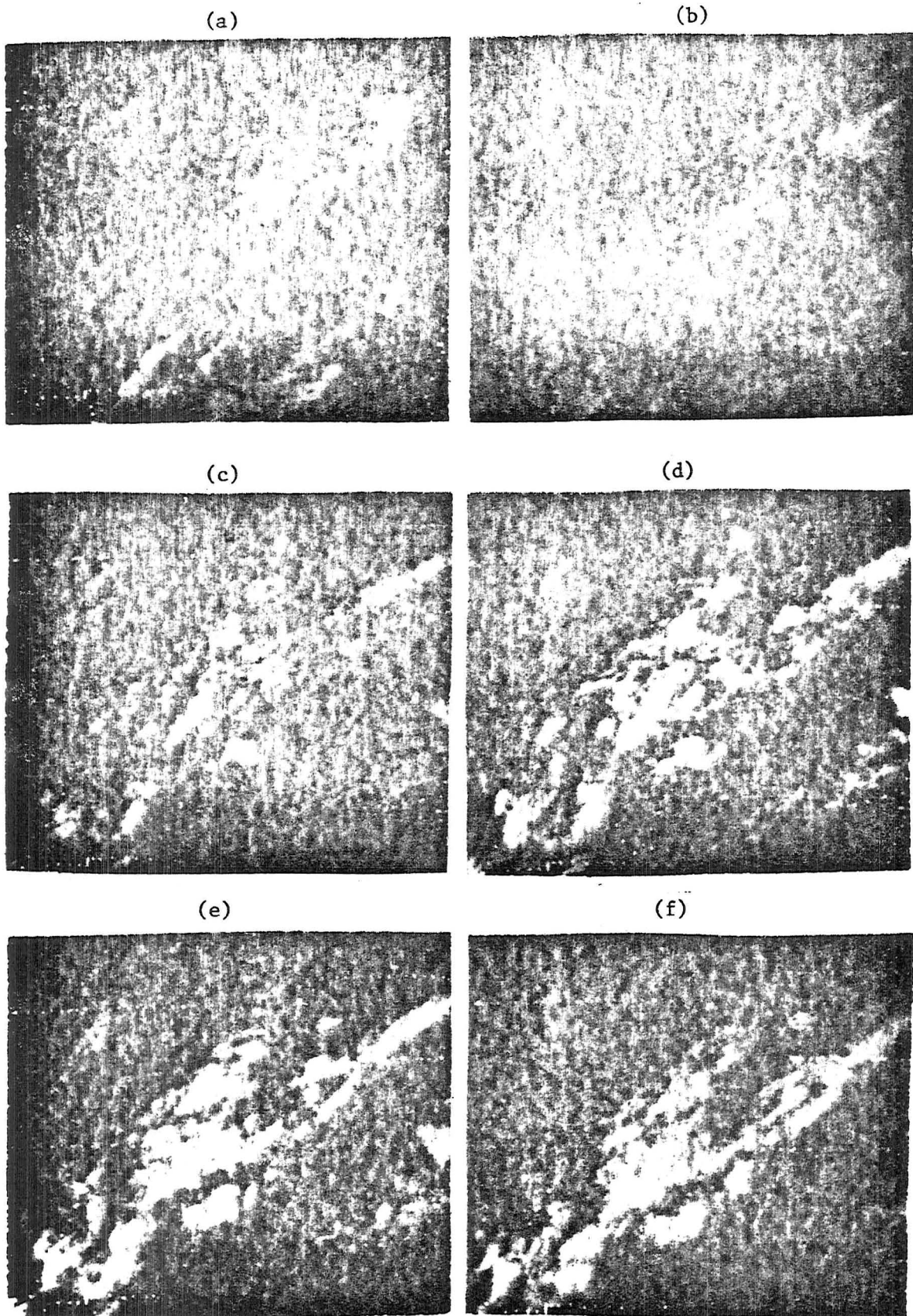
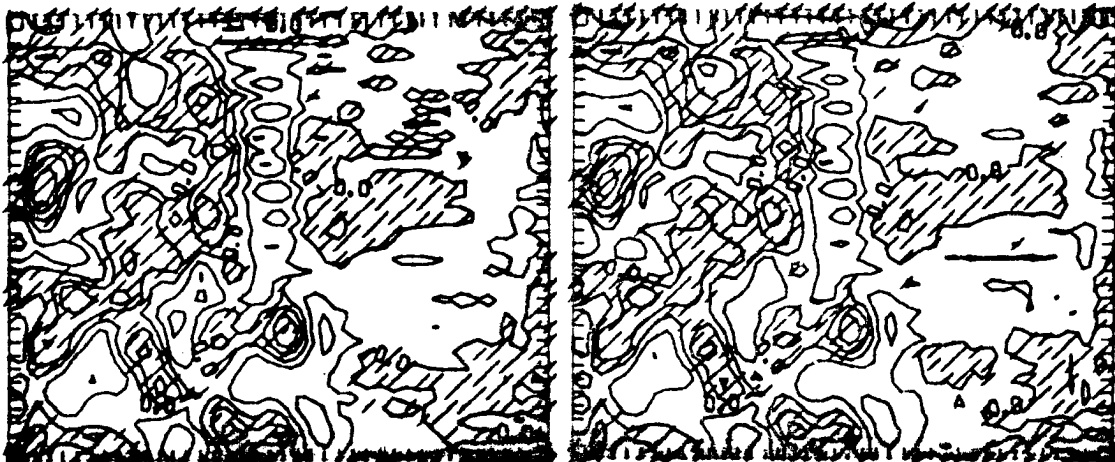


Figure 24 Satellite imagery from ATS-3 taken on July 9, 1973
at (a) 0922 LST (b) 1115 LST (c) 1326 LST
(d) 1405 LST (e) 1504 LST (f) 1602 LST.

(a) w: $z^* = 0.03$, $t = 10:00$

(b) w: $z^* = 0.03$, $t = 10:30$



(c) w: $z^* = 0.03$, $t = 11:00$

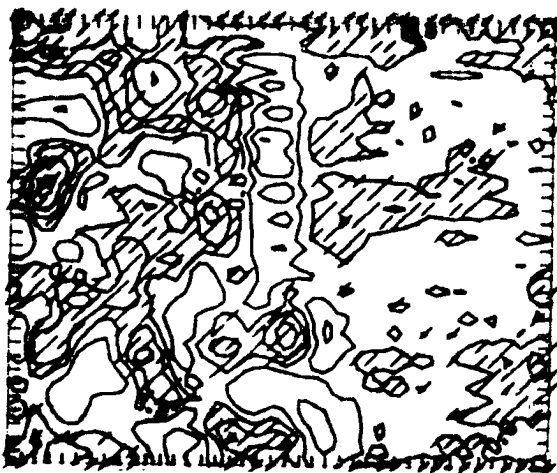


Figure 25

Contour plots of vertical velocity in m sec^{-1} on the $z^* = 0.03$ km surface contoured from -0.3 to 0.3 in intervals of 0.1 at (a) 1000 LST (b) 1030 LST (c) 1100 LST.

the planetary boundary layer, the downslope regime seems to be weakening. The depth of the planetary boundary layer over the Arkansas Valley has deepened and by 1030 LST is about equal to that over the Platte River Valley.

As the surface heat flux continues through 1130 LST, the downslope regime begins to weaken. Areas of positive vertical velocity in the lowest layers erode the negative vertical velocity areas over the plains (Figure 26a-b). Above the boundary layer, the pattern is one of general subsidence over the mountains and rising motion over the plains. The persistence of the east-west divergence orientation can be seen in Figure 27a-b.

By 1115 LST, satellite imagery shows that a line of convection has developed over the mountains east of the Continental Divide (Figure 24b). The Limon radar data taken at 1114 LST also shows the beginnings of mountain convection (Figure 28a). By 1150 LST (Figure 28b), the cells observed west of Denver have moved a few kilometers eastward and have built substantially northward. These cells decay and remain relatively stationary according to the 1201 LST plot (Figure 28c), while the cells west of Colorado Springs remain stationary and build. Of the two cells observed west of Ft. Collins at 1150 LST, the larger one builds quite rapidly and moves eastward, over 10 km in 11 minutes, while the smaller cell builds slightly and remains stationary. The general trend seems to be that early mountainous cells on this day were tied to the topography, except for those which developed strongly enough to become independent of topographic forcing, which could then move rapidly eastward.

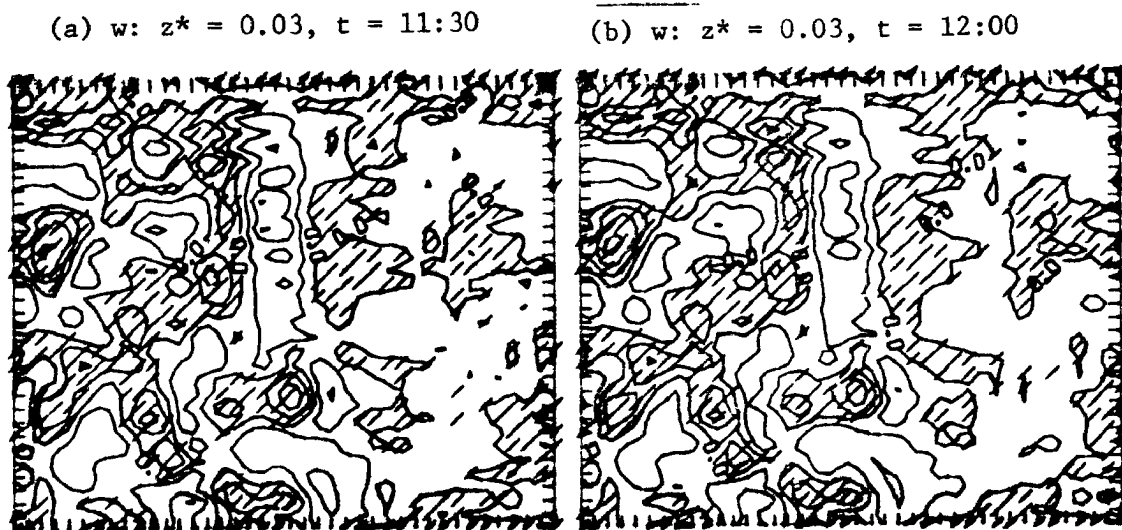


Figure 26 Contour plots of vertical velocity in $m \text{ sec}^{-1}$
on the $z^* = 0.03$ km surface contoured from
-0.3 to 0.3 in intervals of 0.1 at
(a) 1130 LST (b) 1200 LST.

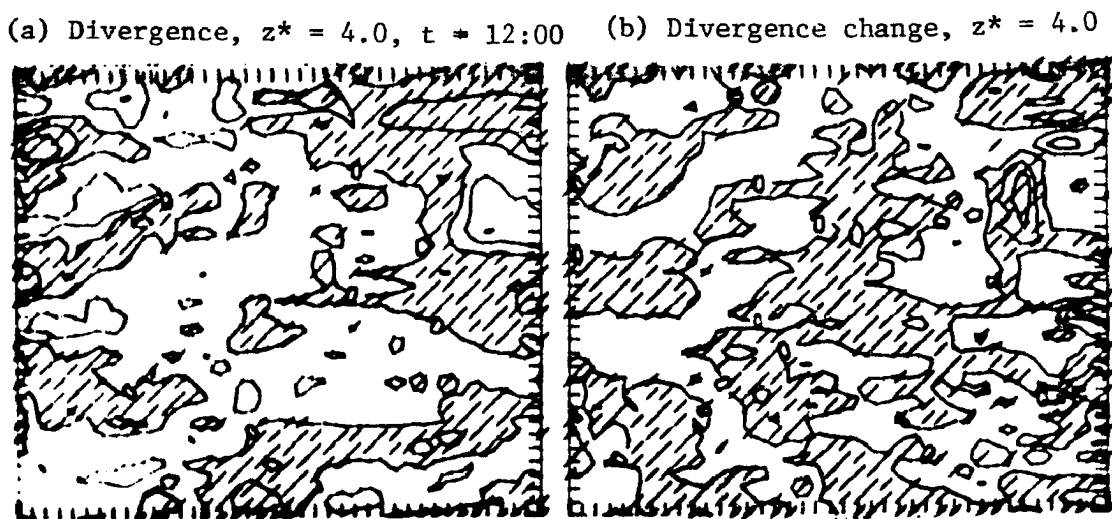


Figure 27 Contour plots on the $z^* = 4.0$ km surface at 1200
LST of (a) divergence contoured from -0.18×10^{-3}
to 0.18×10^{-3} in intervals of 0.9×10^{-4}
(b) the thirty minute change in divergence
contoured from -0.12×10^{-3} to 0.8×10^{-3}
in intervals of 0.4×10^{-4} .

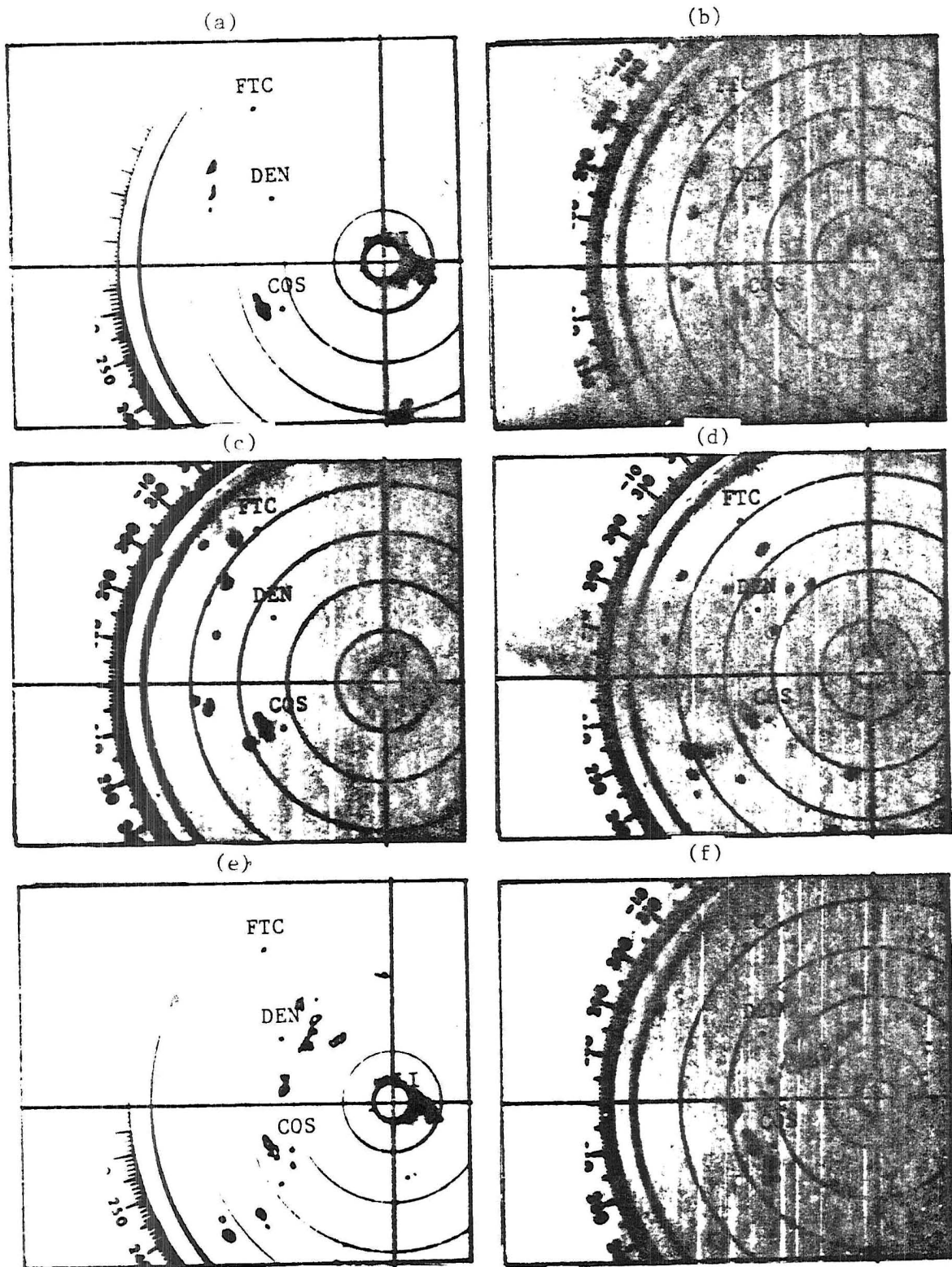


Figure 28

Radar data taken at Limon, Colorado on July 9, 1973
 at (a) 1114 LST (b) 1150 LST (c) 1201 LST
 (d) 1415 LST (e) 1458 LST (f) 1525 LST.

The observed surface winds continue to shift clockwise, but bear little relation to the model winds at 1100 LST. The observed winds were slightly faster (5 to 10 m sec⁻¹) and more organized than at 0800 LST, being generally northerly. Mid-level winds also show some clockwise shift. At 20 kPa, the winds over eastern Colorado show little change, but over western Colorado, shift from westerly to northwesterly in response to the high pressure area pushing up from the south.

The simulated winds in the lower layers are westerly over the plains, except for a southerly component over the Palmer Ridge (Figure 29). Magnitudes are about 5-10 m sec⁻¹ except for areas of minimum speeds which occur in the river valleys of the plains. Simulated winds at $z^* = 2.0$ km were similar to lower winds, but about 2 m sec⁻¹ faster. Winds at $z^* = 4.0$ km displayed a southerly component over the Palmer and Cheyenne Ridges. Predicted winds at $z^* = 6$ km were predominately from the west at about 15 m sec⁻¹.

By 1300 LST, the process of the incursion of positive vertical velocity into areas of negative vertical velocity in the lowest layers is occurring over the mountainous areas, as well as the plains. Since, as mentioned above, the plains surface heating is both more vigorous and peaks sooner than mountain surface heating, it would be expected that downslope circulations will weaken first over the plains. The simulated north-south line of negative vertical velocity east of the Denver-Ft. Collins line begins to build again and stretches southward, reaching the Arkansas River Valley by 1400 LST. At this time there is a general

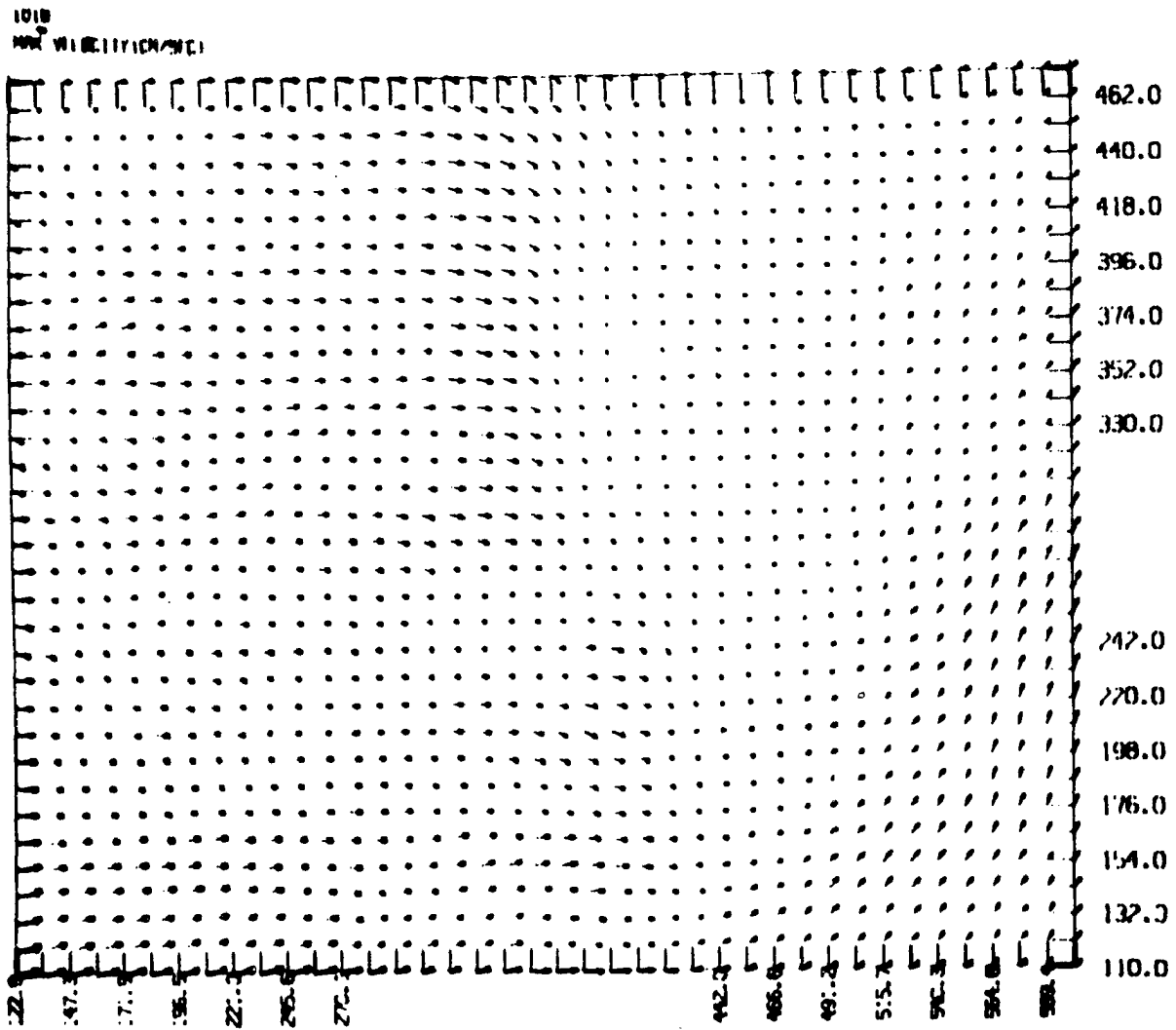


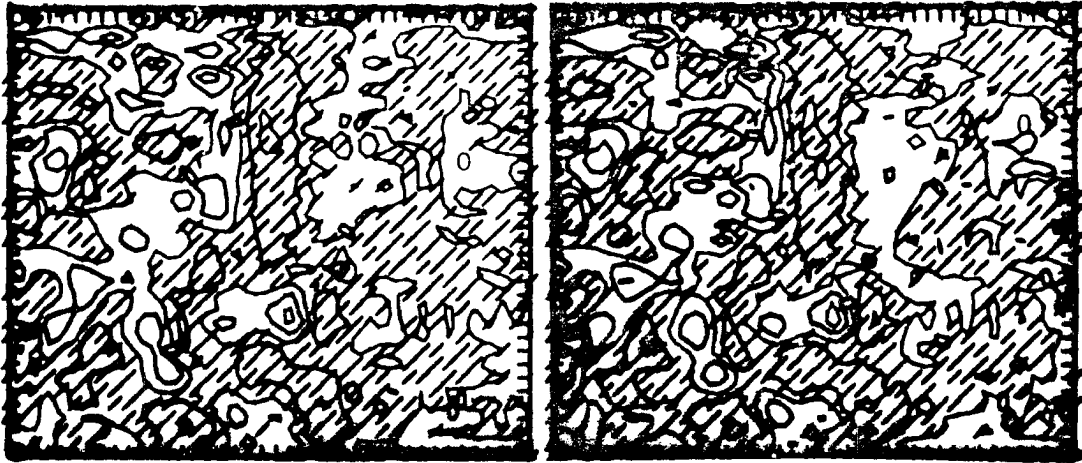
Figure 29 Vector plot of horizontal winds at interior grid-points on the $z^* = 0.03$ km surface at 1230 LST.

increase of convergence over the mountains and a decrease over the plain, consistent with the continued weakening of the downslope regime.

The Limon radar data show that the plains storms east of Denver display a southward propagation and development along a north-south line around this time. (Compare the 1415 LST plot, Figure 28d, with the 1458 LST plot, Figure 28e.) Examining the plots for 1458 LST and 1525 LST, we see the same north-south movement or propagation in the cells north and northwest of Limon (Figure 28f). These observations are consistent with the findings of the NHRE project for this day (Chalon, et al 1976). The Limon radar indicates that this was characteristic of cell movement over a larger spatial and temporal interval than that studied by the NHRE project. The convective line noted in the 1115 LST ATS-3 photograph by 1326 LST has increased in activity (Figure 24c). Also at this time one can notice a line of convection stretching northeast from the four corners area. The cloud-free area northwest of this is in the same area as the "channeling" predicted by the model which was forced by the topography. In little more than half an hour, convection throughout the experimental area has become dramatically enhanced. The eastward progression of certain features in the lowest layers of the model can be seen by following the feature marked "O" in Figure 30. This movement is quite slow (about 4 m sec^{-1}) and could be entirely explained by advection. One should note, however,

(a) Divergence: $z^* = 0.03$, $t=13:30$

(b) Divergence: $z^*=0.03$, $t=14:15$



(c) Divergence: $z^*=0.03$, $t=15:15$

(d) Divergence: $z^*=0.03$, $t=16:15$

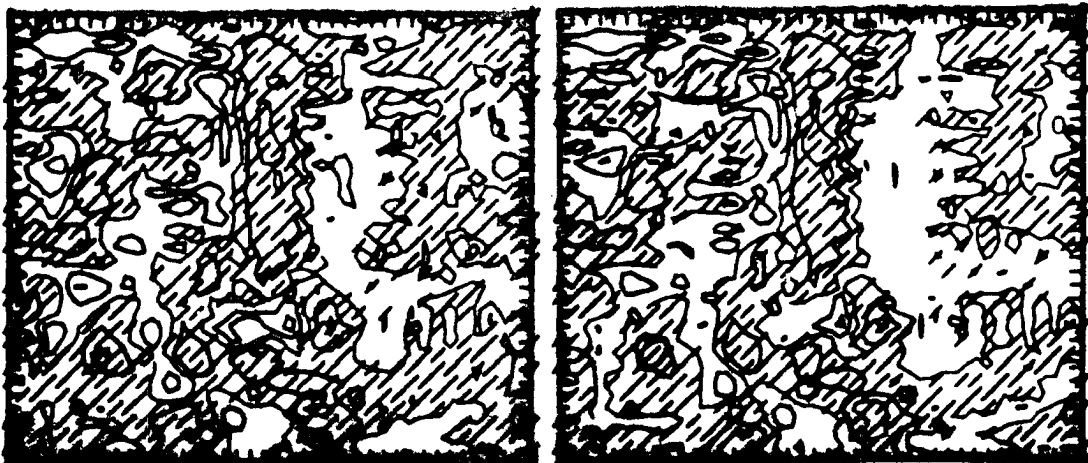


Figure 30

Contour plots of divergence on the $z^* = 0.03$ km surface contoured from -0.14×10^{-3} to 0.14×10^{-3} in intervals of 0.7×10^{-4} at (a) 1330 LST (b) 1415 LST (c) 1515 LST (d) 1615 LST.

that this type of movement occurs only over the plains. Mountain features continue to be tied to the topography.

The gradients in the moisture field begin to increase at 1515 LST and a drying below the boundary layer and moistening above can be noted (Figure 31a-d). This was attributed to the general albeit weakened downslope transport of drier air in the lower layers and opposite flows above the boundary layer. This upper level moistening occurs about two hours after the moistening observed by Wetzel (1973). The 1504 LST ATS-3 image suggests the enhancement of propagation of the mountainous convection over the Cheyenne and Palmer Ridges (Figure 24e). By 1602 LST (Figure 24f), the convection over the mountains is observed to be noticeably dissipating while that over the plains area seems to be increasing in vigor.

The observed surface winds at 1400 LST continued to respond to synoptic forcing, shifting to northeasterly over the northern plains, and having speeds of about 10 m sec^{-1} . The predicted winds showed very little change in speed or direction in this period. The 1515 LST vector plot (Figure 32) shows the beginnings of a simulated southerly jet-like flow in the lower levels, which by 1616 is more strongly developed. The predicted negative vertical velocity begins to develop again during this time increasing in magnitude and area. The north-south line character of the vertical velocity begins to give way to dominance of the flow by local ridge and valley effects. This tendency continues through 1915 LST when the north-south negative vertical velocity line begins to build briefly, but starts to dissipate again

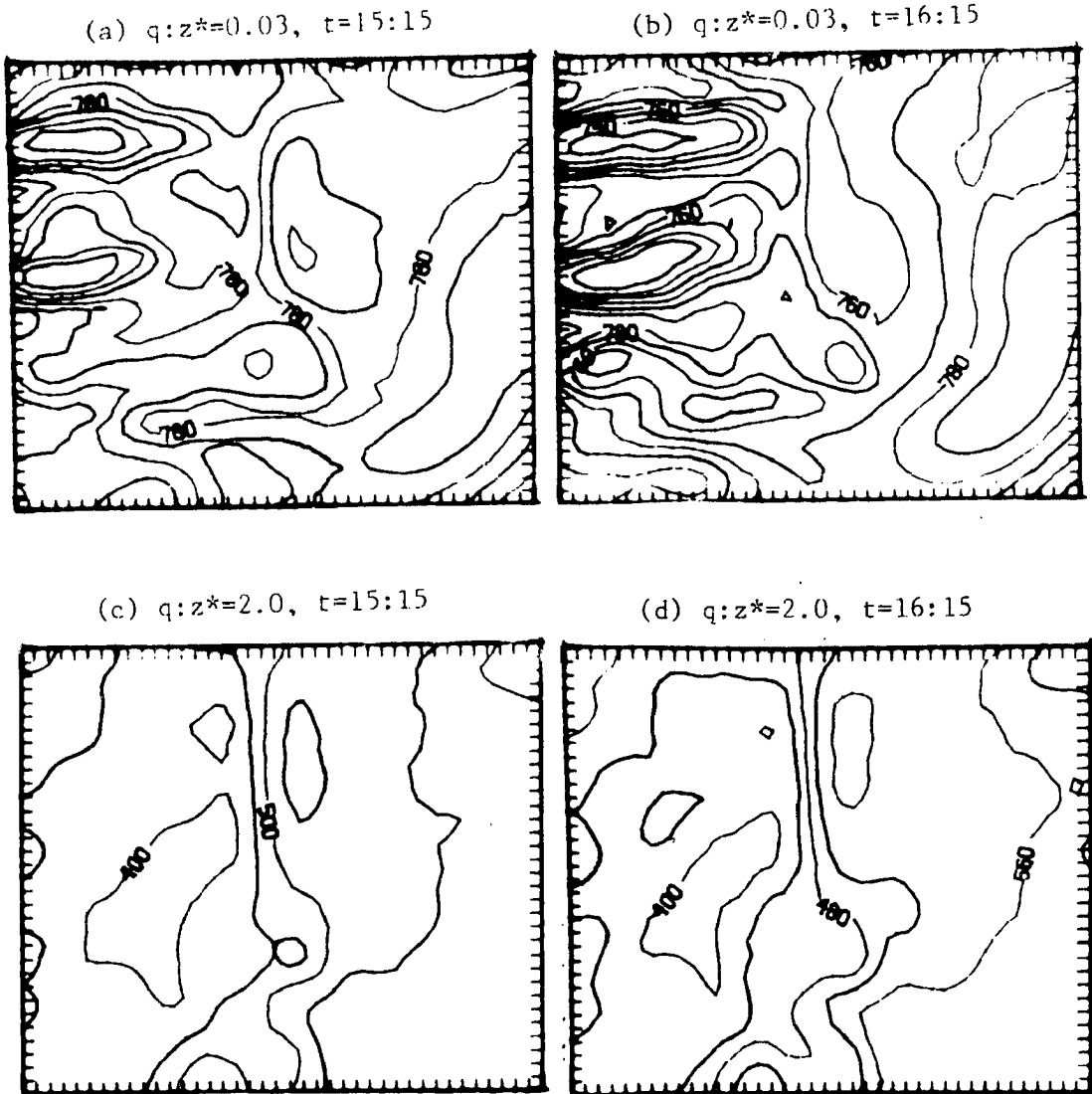


Figure 31 Contour plots of mixing ratio in grams metric ton⁻¹ (a) on the $z^* = 0.03$ km surface at 1515 LST contoured from 740 to 810 in intervals of 10 (b) on the $z^* = 0.03$ km surface at 1615 LST contoured from 720 to 800 in intervals of 10 (c) on the $z^* = 2.0$ km surface at 1515 LST contoured from 350 to 600 in intervals of 50 (d) on the $z^* = 2.0$ km surface at 1615 LST contoured from 360 to 600 in intervals of 40.

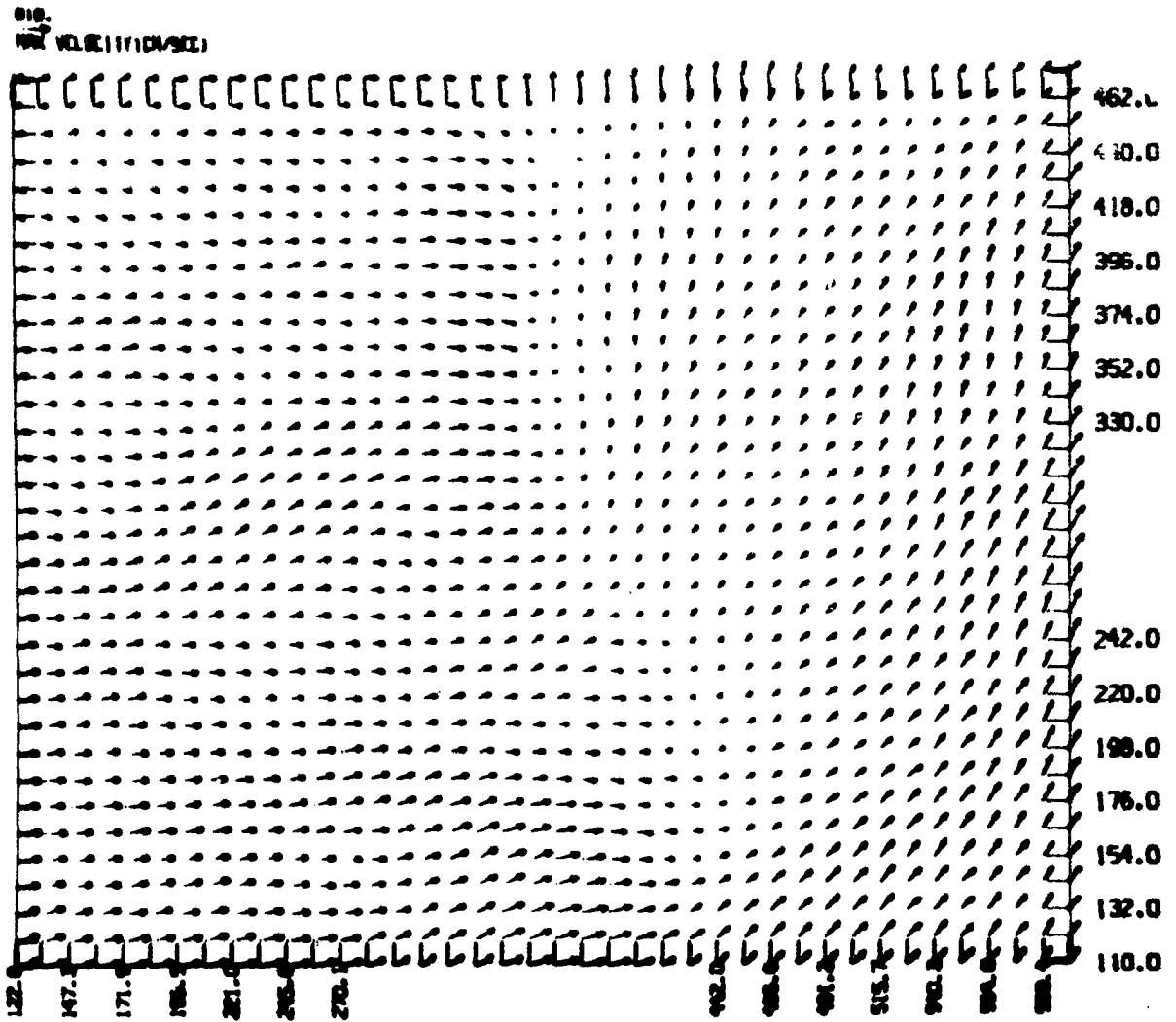


Figure 32 Vector plot of horizontal winds at interior grid-points on the $z^* = 0.03$ km surface at 1515 LST.

within an hour. The low-level jet-like flow at this time is at its maximum speed (about 5 m sec^{-1}). Two centers of cyclonic flow appear along this line (Figure 33) but do not appear to be correlated with any significant pressure anomalies (Figure 34 a b) and may simply be induced by a tendency for upslope flow.

The suggestion of the occurrence of a low-level jet in the lee of the Rockies may bear some relationship to the increased occurrence of severe thunderstorms in that region. It has been long-noted that the low-level jet and occurrences of nocturnal thunderstorms are well-correlated over the great plains (Pitchford and London, 1962; Bonner, 1968). Relatively little work has been done on jets closer to the Rockies, primarily because the strong local forcing by topography makes interpretation of climatological data difficult. If the eastward propagation of convection noticed by Dirks (1969) and others is valid, it would not be unexpected to find a jet-like flow in an area of enhanced convection earlier in the day, particularly when much local forcing has been removed by smoothing the topography in the model. It is important to note two things concerning this jet-like flow. First, the flow is only about five meters per second, and only gives an appearance of a jet because of the contrast with surrounding points with regard to both direction and speed. Secondly, it should be noted that one of the prominent explanations for the occurrence of great-plains low-level jets is the decoupling from surface frictional effects through the establishment of nocturnal inversions. The explanation for the jet-like flow observed in the model must invoke a different mechanism. Wexler (1961) suggested an alternative

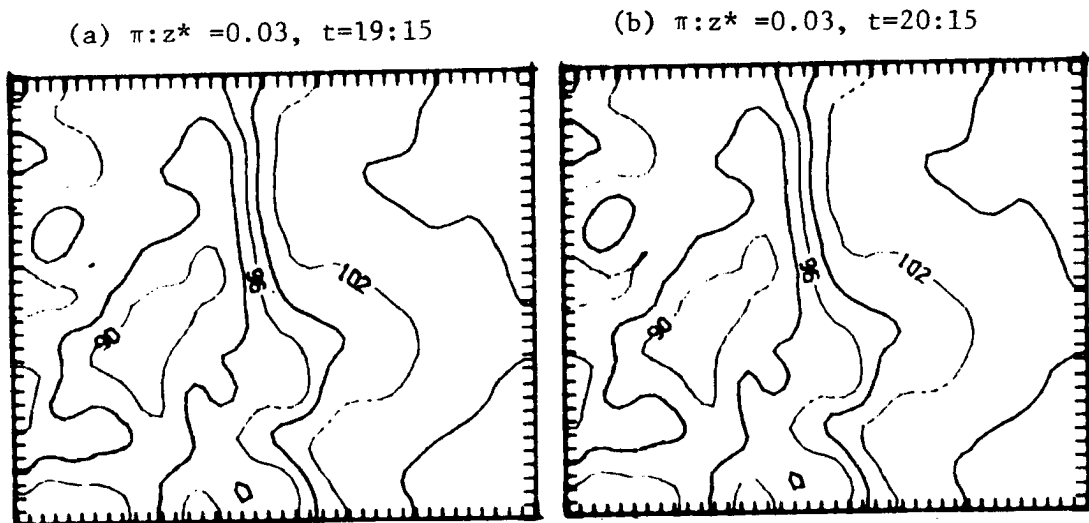


Figure 34 Contour plots of the Exner function in Joules kilogram⁻¹ °K⁻¹ on the $z^* = 0.03$ km surface contoured from 87 to 105 in intervals of 3 at (a) 1915 LST (b) 2015 LST.

explanation which, with some modification, might serve to explain this result. As the flow crosses the ridge it increases in velocity; and when it suddenly reaches the plains, experiences a sharp drop in velocity which could cause the occurrence of ageostrophic forcing, including a turn toward the lower pressure in the north associated with the heating of the Cheyenne Ridge (Figure 35). Note that this jet-like flow occurs east of the steepest topographic gradient encountered by the flow as it crosses the mountains.

By 2115 LST, the planetary boundary layer has reached its maximum depth (about 3.5 km). One can also notice at this time another episode of eastward movement of the negative vertical velocity area accompanied by a large increase in convergence. The low-level jet-like flow begins to weaken at this time. During this period, the lower levels experience a general moistening while above the boundary layer, there is a drying tendency. The observed winds at 2100 LST were rather disorganized at the surface but appeared to be influenced both by the southward progression of the high pressure area and the onset of downslope circulations at some locations. Upper and mid-levels showed little change from the 1700 LST situation in either the observed or predicted winds.

At 2215 LST, the simulated positive vertical velocity again begins to overtake areas of negative vertical velocity, moving in a generally eastward direction (Figure 36a-b). The magnitudes remain about $\pm 0.3 \text{ m sec}^{-1}$. The topography of the plains once again begins to dominate the north-south line organization of the vertical velocity, both above and below the boundary layer. By

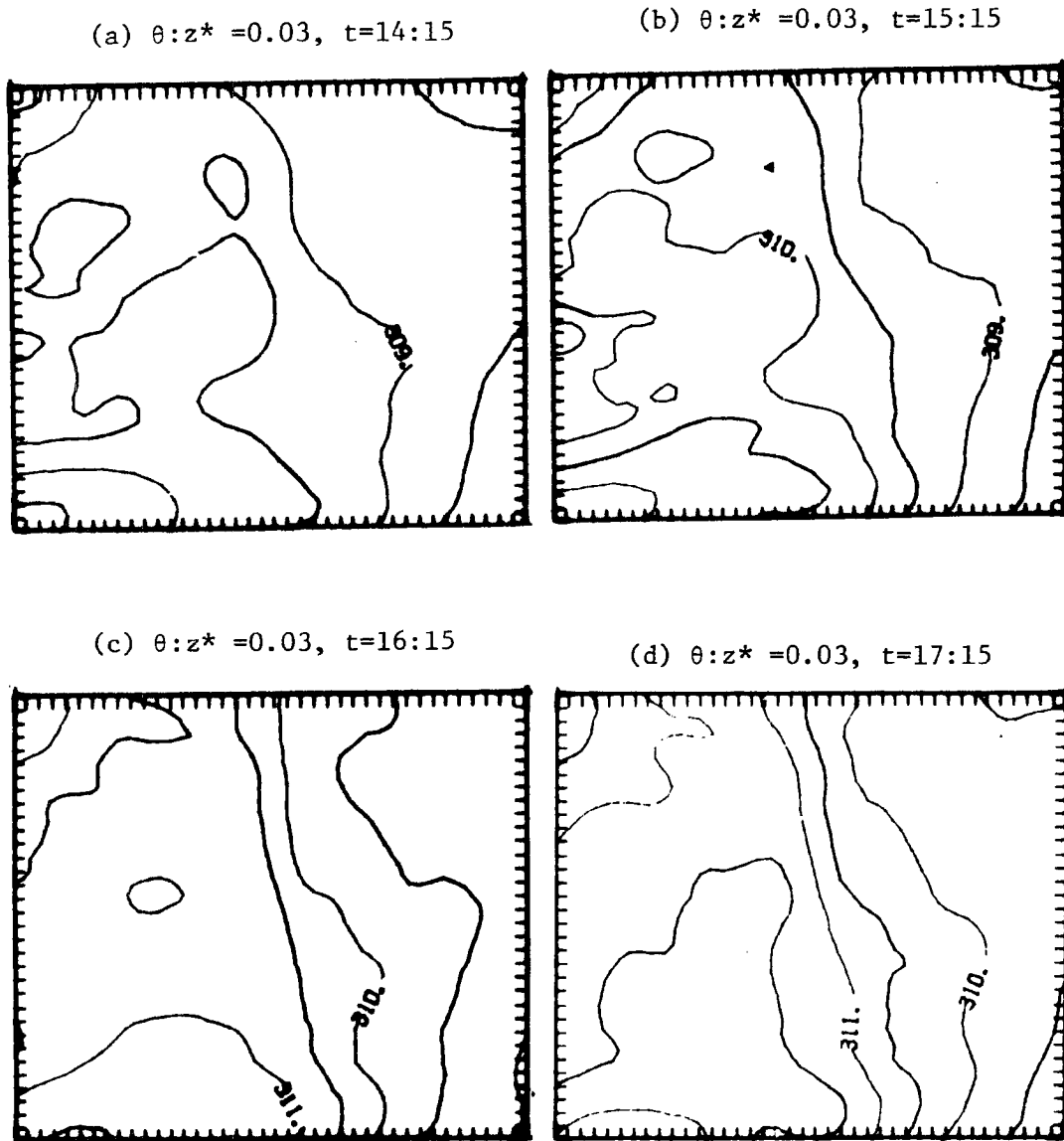


Figure 35 Contour plots of potential temperature in $^{\circ}\text{K}$ on the $z^* = 0.03$ km surface contoured from 308 to 312 in intervals of 0.5 at (a) 1415 LST (b) 1515 LST (c) 1615 LST (d) 1715 LST.

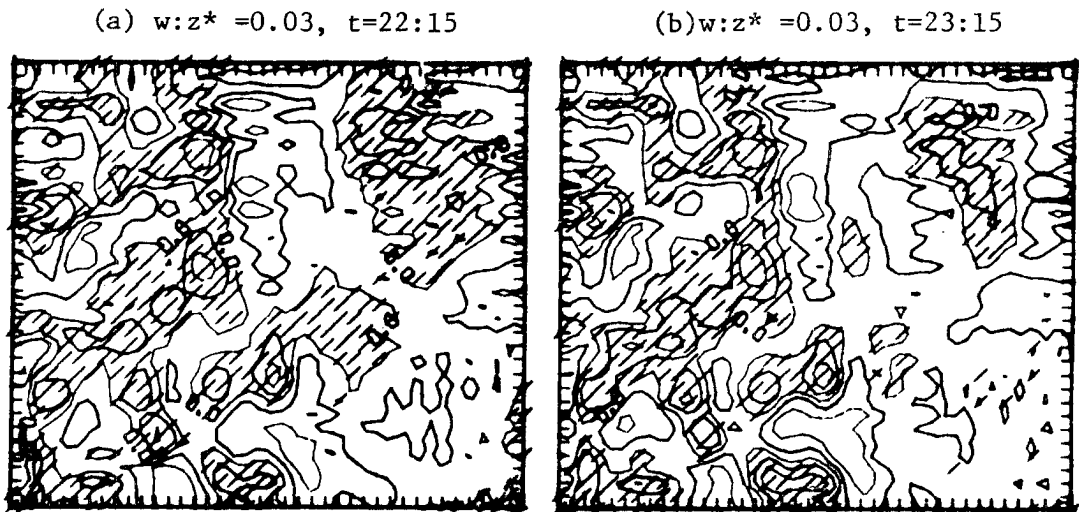


Figure 36 Contour plots of vertical velocity in m sec^{-1} on the $z^* = 0.03$ km surface contoured from -0.2 to 0.3 in intervals of 0.1 at (a) 2215 LST (b) 2315 LST.

2315 LST, positive vertical velocity has virtually overtaken the plains; while, the jet-like flow has turned eastward and become indistinguishable.

There is little further change in the flow. The planetary boundary layer decreases in depth as the surface cools. The down-slope regime circulation: the divergence over the peaks, and convergence in valleys, increases in magnitude. The integration was terminated at 2545 LST.

3.4 Experiment C: August 4, 1977 Simulation

The third experiment was an attempt to investigate the role of the ridge/valley circulation in the genesis of mesoscale convective systems observed on August 4, 1977. This date was chosen because of the extensive data available as well as the extensive analysis that has been done (George, 1978) in connection with the SPACE. The day was not strongly forced synoptically, but convective cells of size and intensity which were conducive to eastward propagation (including a tornado sighting and other severe weather) occurred (Danielson and Cotton, eds., 1977). The winds over the study area at 0500 LST were quite non-uniform. It was decided to use winds from the Limon sounding (Figure 37) since these were most typical of the observed winds later in the day. It will be noted that though this wind profile veers in a manner very similar to that in Experiment B, the winds are generally much stronger, being about 5 m sec^{-1} in the lower layers and increasing to about 18 m sec^{-1} aloft. The temperature soundings were quite similar throughout the study area, so the 0500 LST Limon sounding provided the basis

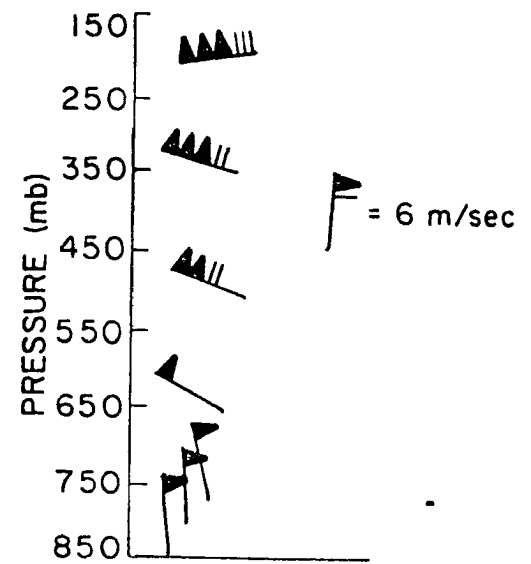
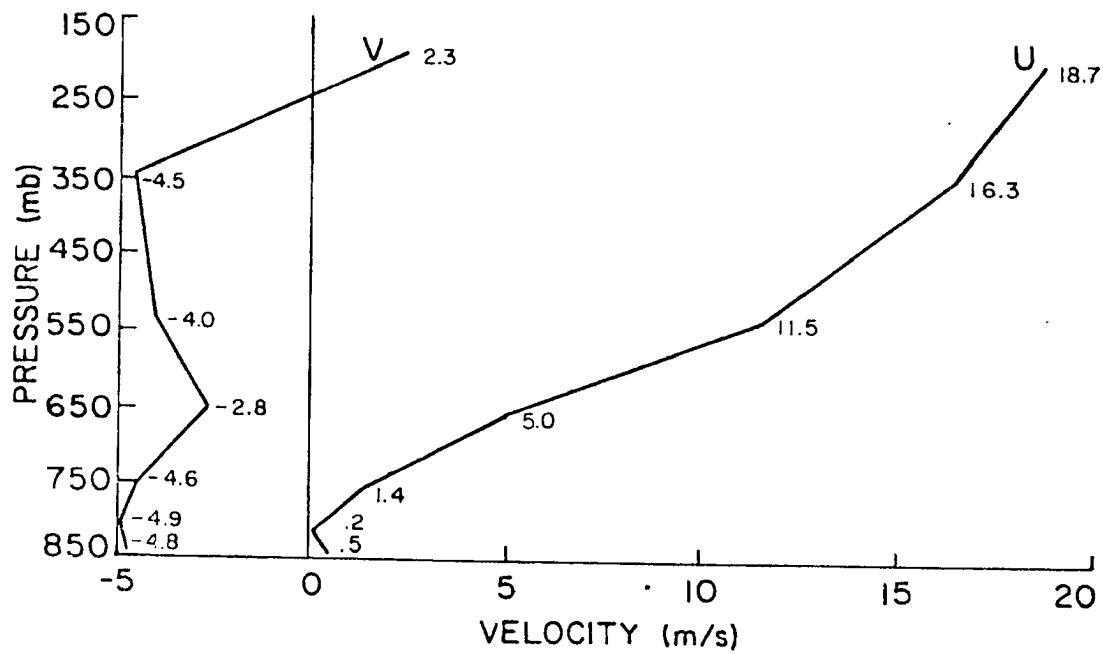


Figure 37 Initial winds used for Experiment C.

for that initialization as well (Figure 38). This sounding features a morning inversion of about 5° C, 4 kPa thick which, as shown in Figure 38, was removed for the simulation. The air is quite stable immediately above this and is overlain by a slightly stable layer extending to about 67 kPa. Above this there is an adiabatic layer up to about 52 kPa. The air is generally moist adiabatic until about 25 kPa and stable above this. Because of the coarse resolution in the upper levels of the model, the observed temperature was 3° to 5° C cooler than the model above 32 kPa. Below 50 kPa, this sounding showed stability characteristics similar to the sounding for Experiment B (Figure 12), although it was about 2° C warmer. Between 50 kPa and 30 kPa the lapse rate of potential temperature for Experiment C was less than that for Experiment B, while the opposite situation occurred above 30 kPa.

It was found in the results from Experiment B that some ambiguity occurred in the interpretation of the moisture convergence. Since, in layers 2-4 the mixing ratio was relatively constant, it was difficult to conjecture on the source of moisture anomalies in these levels. Taking into account the fact that moisture in this model is merely a "tracer", it was decided to significantly change the moisture profile in order to provide more distinction among the layers. The result is shown in Figure 38.

The heating profile which was used along with data to which the curves were fit (in a manner described above) is shown in Figure 39. This function is somewhat more realistic than that in Experiment B since it has a much shorter period of increasing surface temperature. It should be noted that, because of this,

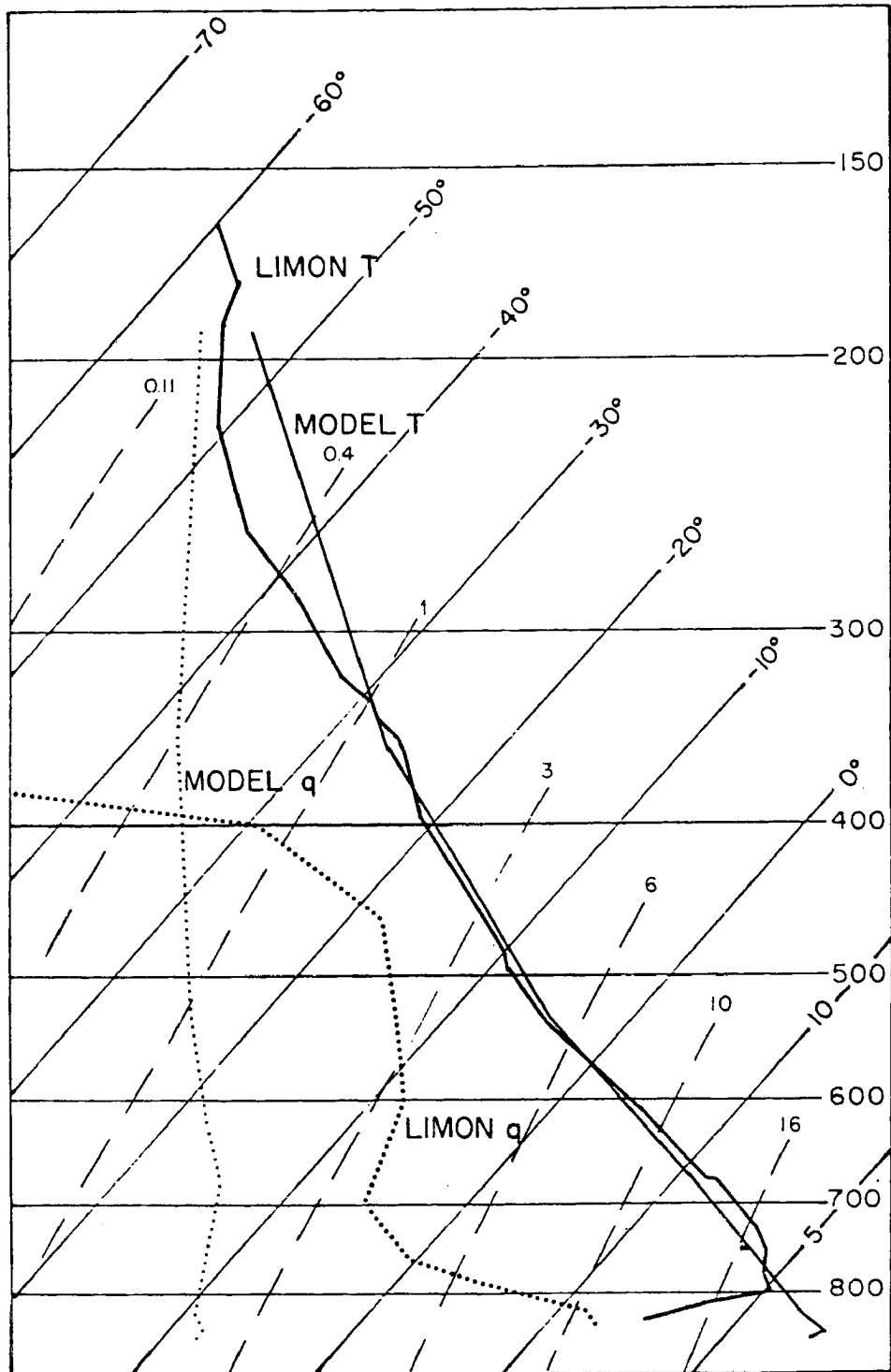


Figure 38 Skew-T, log-P plot of the thermodynamic sounding taken at 0500 LST on August 4, 1977 at Limon and of the sounding used in the model for Experiment C.

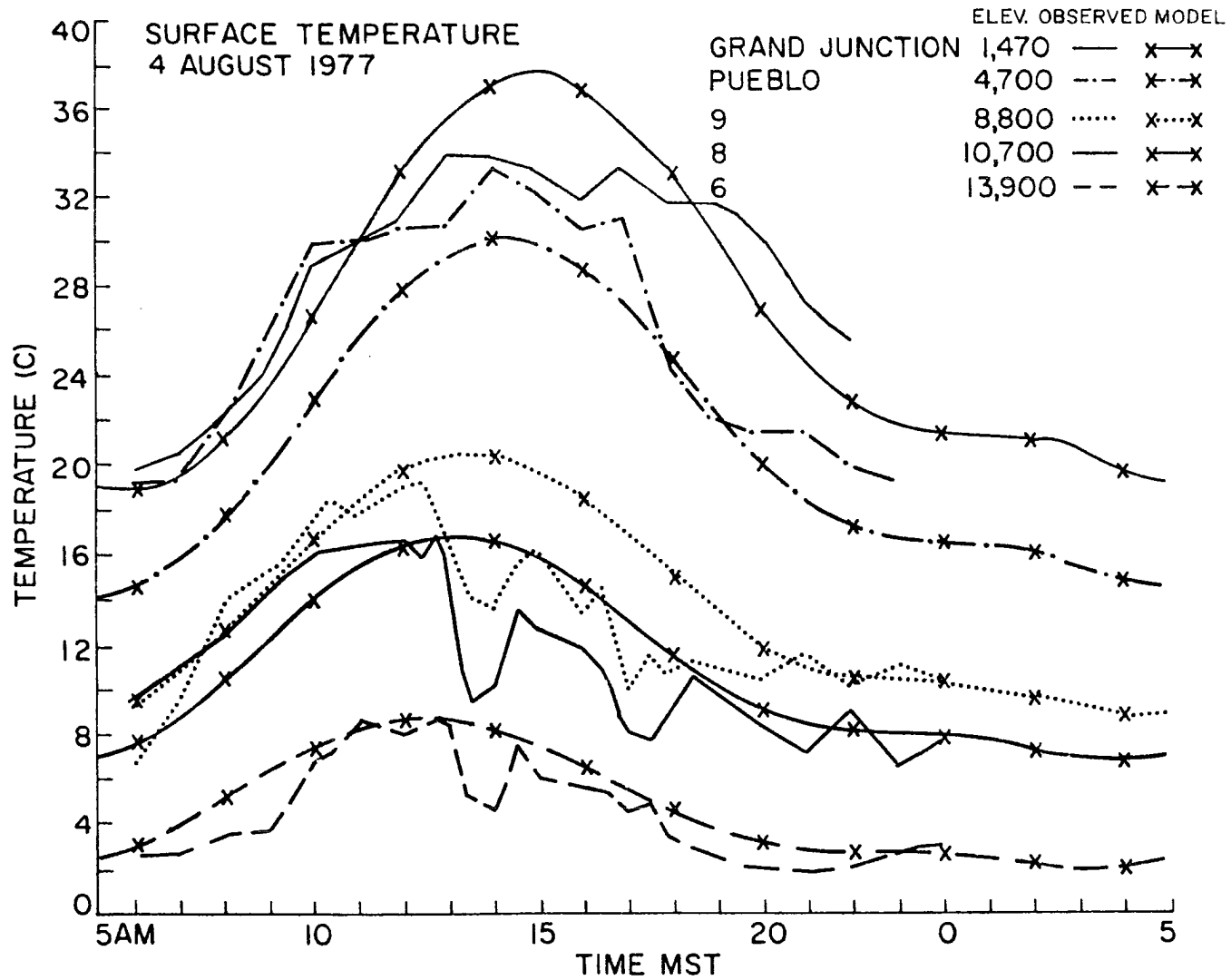


Figure 39

Observed and modeled surface temperatures for five locations within the model domain at various elevations for Experiment C. Numbered locations refer to NCAR Portable Automated Mesonet surface stations used during the SPACE.

Experiment C begins its heating at 0400 LST, while Experiment B started at 0100 LST. Experiment C has a maximum temperature about 2° C warmer in the lower elevations than Experiment B. The higher elevations have very similar maximum temperatures. Maximum temperatures in the lower elevations are reached about two hours after the maximum in higher elevations; the reverse of the situation in Experiment B.

An exhaustive description of events on August 4, 1977, observed in connection with the SPACE can be found in George, 1978. Below is a synopsis of these events, especially as they pertain to the experimental area.

The synoptic situation on August 4, 1977 bears many similarities to that on the Experiment B study day. A low pressure area was situated over the Texas-Oklahoma panhandle at 0500 LST (Figure 40). A high pressure area began to push southward east of the Rockies and the low pressure area moved southeastward as the day progressed. The effects of these two systems combined to provide the area with easterly and northeasterly winds, accompanied by a strong influx of moisture by 1800 LST. The upper winds were predominately zonal over the area of interest. Two high pressure areas off the California coast and south of El Paso induced some upper air moisture transport into the experimental region.

The initial flow in the model, before steady state obtains, resembles the downslope regime of Experiment B over the mountainous regions. Over the plains, however, convergence and positive vertical velocity (about 0.4 m sec^{-1}) dominate, except

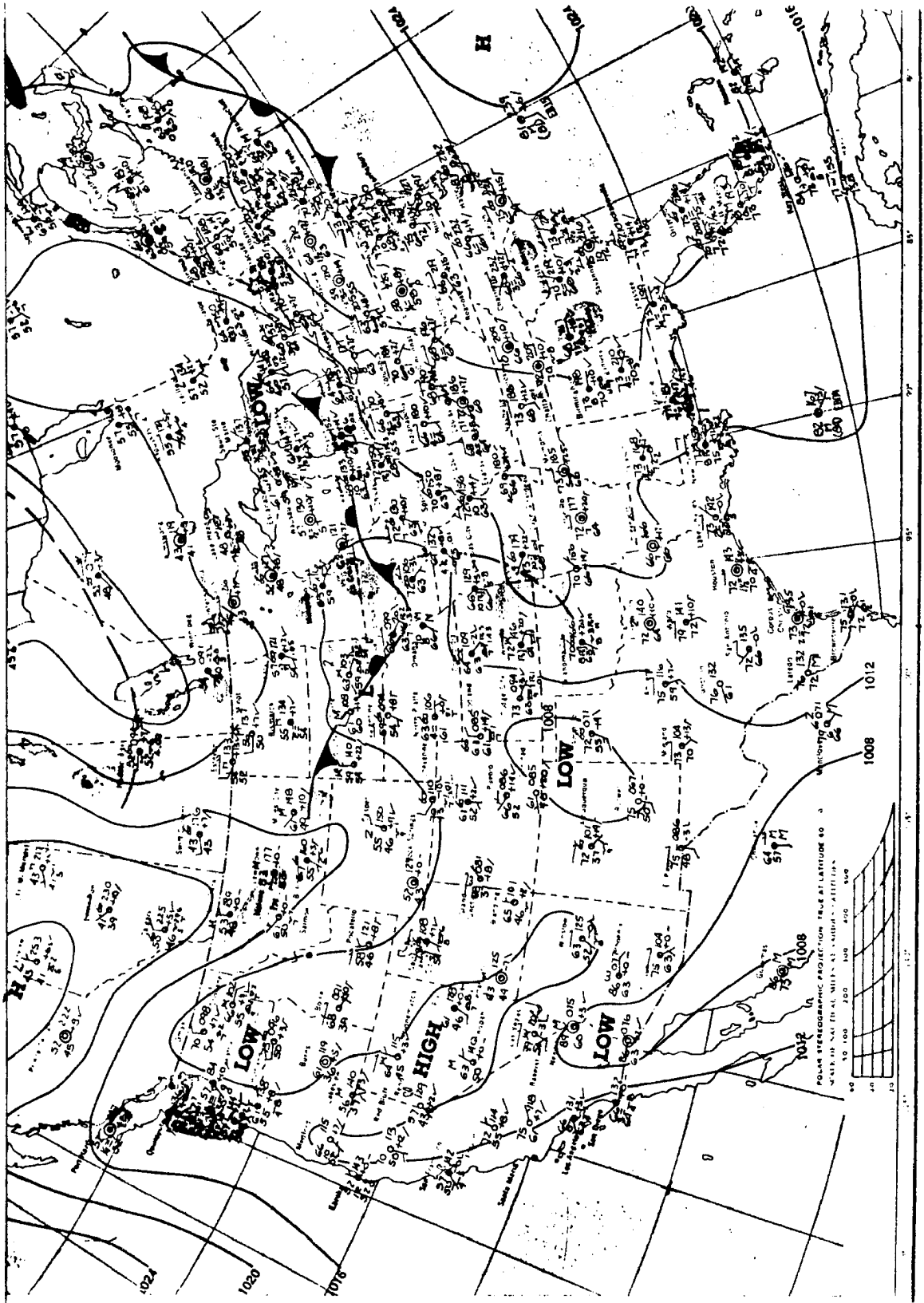


Figure 40 Surface weather map for the United States at 0500 LST on August 4, 1977.

over the Platte River Valley (Figure 41a-b). As mentioned, the observed surface winds were light and variable, but generally from the north. The initial model winds (Figure 37) were characteristic of the observed winds aloft.

The CSU surface mesonet system which was employed for the SPACE on this day (see Danielson and Cotton, eds., 1977) provides a more detailed view of the meteorological occurrences over the experimental area. At 0500 LST, the contrast between the air being brought in by the low pressure area to the southeast and by the high to the northwest generated a stationary front. The area north of Limon and south of Denver and Goodland, Kansas was characterized at the surface by northerly winds and air which was cooler and drier than the more southerly air mass, which had an easterly component in the surface winds. The satellite imagery for the day shows Colorado to be, for the most part, cloud-free at 0600 LST.

After the heating function is begun, a thin line of convergence and positive vertical velocity develops along the Platte River Valley (Figure 41c-d). The Palmer Lake Divide is dominated by negative vertical velocity and divergence. Below the boundary layer, the change in divergence is oriented along a north-south line, while above it, the change in divergence seems more determined by topographic features, being largest above the Palmer Lake Divide. The distribution of moisture shows some similarity to that obtained in Experiment B. The mountainous areas of the model are driest at the surface and, above the boundary layer, there is a general tendency for drying. One can

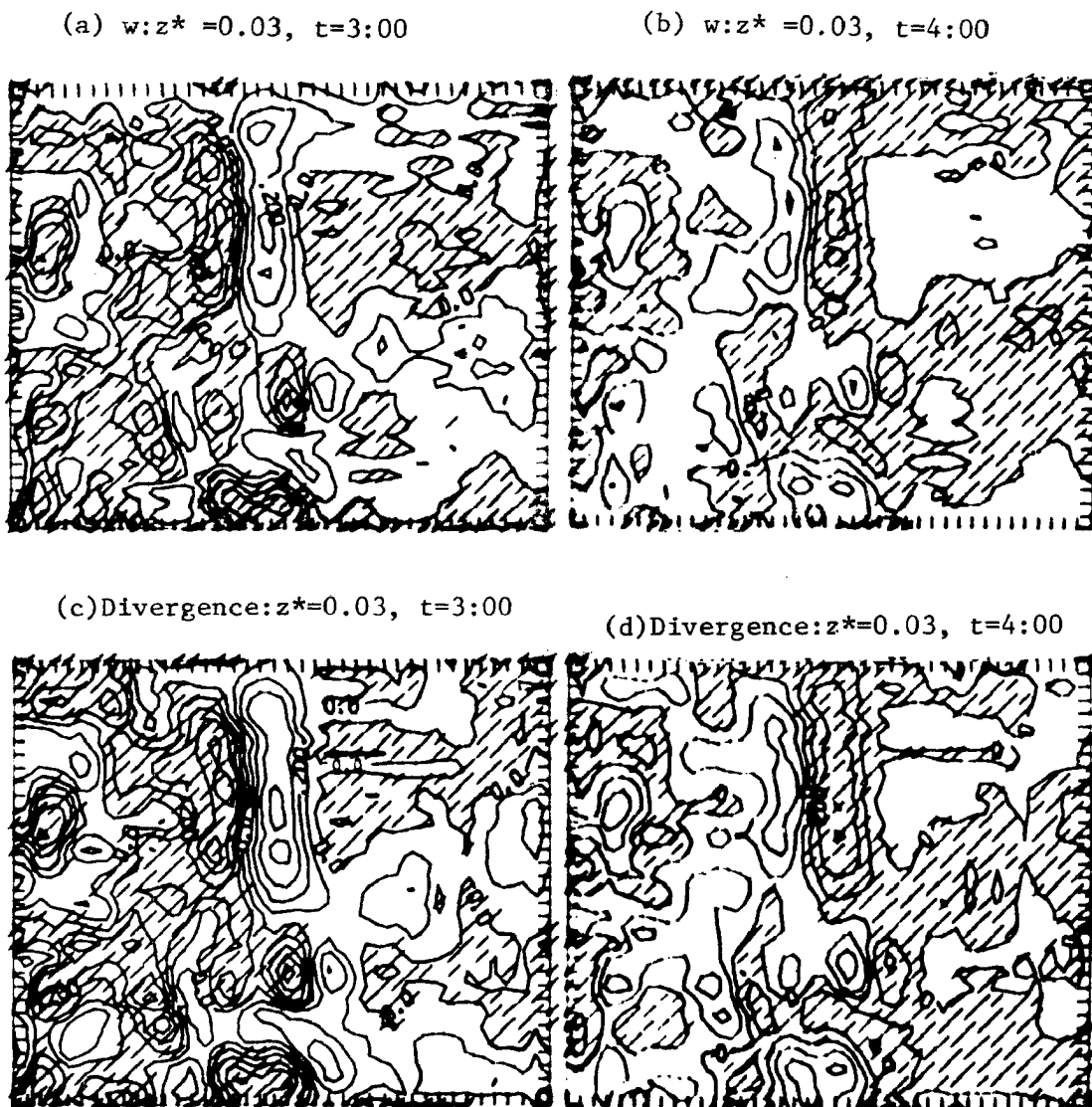


Figure 41

Contour plots on the $z^* = 0.03$ km surface of
 (a) vertical velocity in m sec^{-1} at 0300 LST
 contoured from -0.4 to 0.4 in intervals of 0.1
 (b) vertical velocity in m sec^{-1} at 0400 LST
 contoured from -0.4 to 0.4 in intervals of 0.1
 (c) divergence in sec^{-1} at 0300 LST contoured
 from -0.3×10^{-3} to 0.3×10^{-3} in intervals of
 0.1×10^{-3} (d) divergence in sec^{-1} at 0400
 LST contoured from -0.3×10^{-3} to 0.3×10^{-3}
 in intervals of 0.1×10^{-3} .

note an area of intense negative vertical velocity (-0.5 m sec^{-1}) west of the Colorado Springs area associated with a local topographic maximum. This was also noted in Experiment B and indicates the influence of the (strongly smoothed) Pike's Peak area.

By 0500 LST, the familiar pattern of divergence over ridges and convergence over valleys has become quite clear (Figure 42a). Again, the areas of strong vertical velocity seem to be associated with steep topography gradients; having values of $\pm 4.0 \text{ m sec}^{-1}$ above the boundary layer and $\pm 0.4 \text{ m sec}^{-1}$ below it. The flow above the boundary layer at this time is one of subsidence over the mountainous areas and rising motion over the plains (Figure 42b). A north-south line seems to be developing at 0600 LST but this gives way to more topographic forcing by 0800 LST (Figure 42c-d). At this time, the area covered by negative vertical velocities below the boundary layer is increasing and magnitudes have increased to about $\pm 0.6 \text{ m sec}^{-1}$. Also, at 0800 LST, the moisture field below the boundary layer is at its driest stage.

Above the boundary layer, the winds over the Palmer Lake Divide are shifting from westerly to northwesterly. This windshift tendency has affected the lowest level by 0900 LST. The region covered by negative vertical velocities is retracting at this time and the north-south line orientation of vertical velocities begins to appear again (Figure 43a-b). This erosion of negative vertical velocities continues until at 1000 LST the plains are dominated by positive vertical velocities, the mountains by negative vertical velocities, above the boundary layer (Figure 43c). Also above the boundary layer, drying continues throughout the domain. Below,

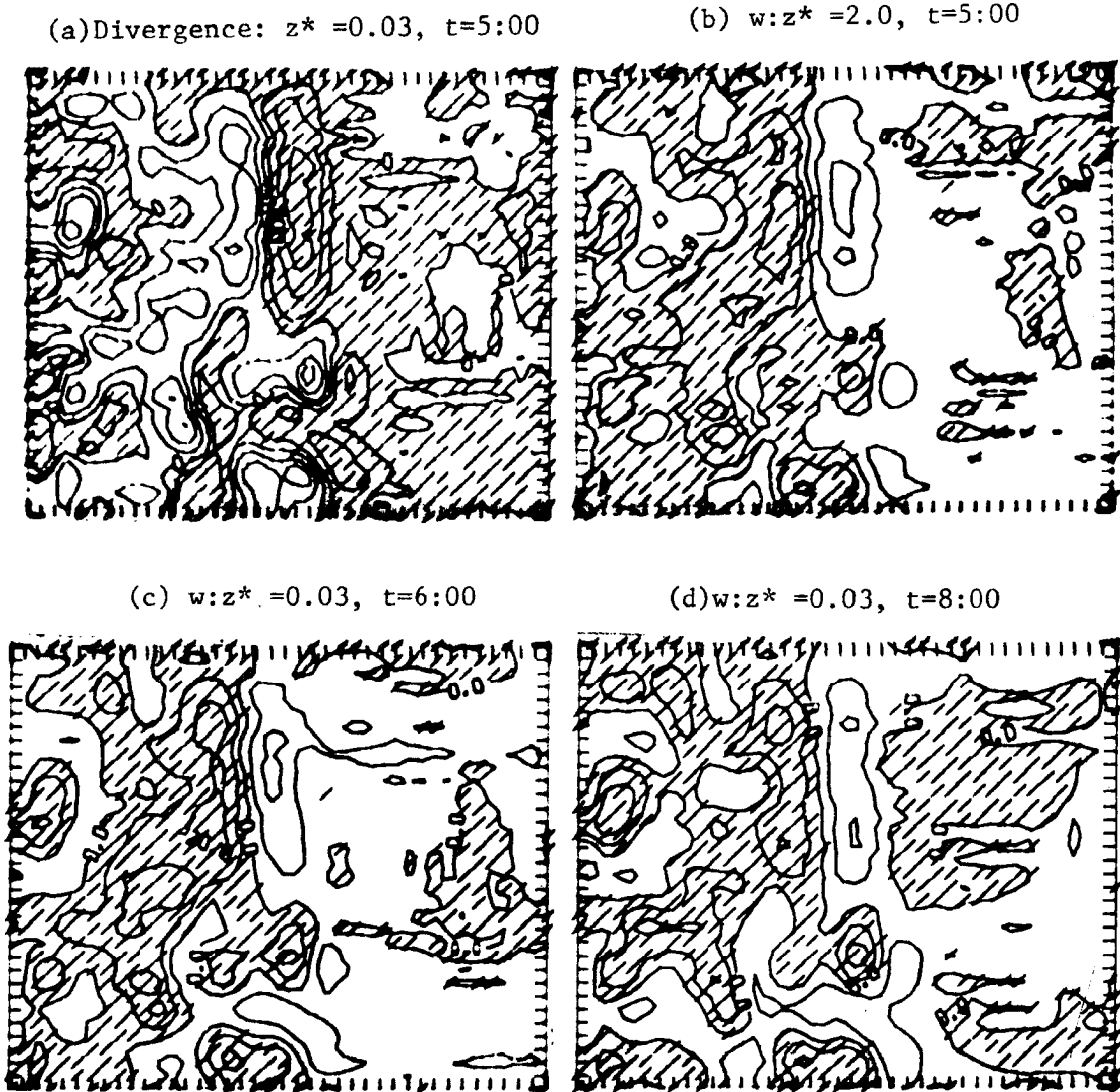


Figure 42 Contour plots of (a) divergence at 0500 LST on the $z^* = 0.03$ km surface in sec^{-1} contoured from -0.3 to 0.3 in intervals of 0.1 (b) vertical velocity in m sec^{-1} on the $z^* = 2.05$ km surface at 0500 LST contoured from -4.0 to 4.0 in intervals of 1.0 (c) vertical velocity in m sec^{-1} at 0600 LST on the $z^* = 0.03$ km surface contoured from -0.3 to 0.3 in intervals of 0.1 (d) vertical velocity in m sec^{-1} on the $z^* = 0.03$ km surface at 0800 LST contoured from -0.9 to 0.6 in intervals of 0.3 .

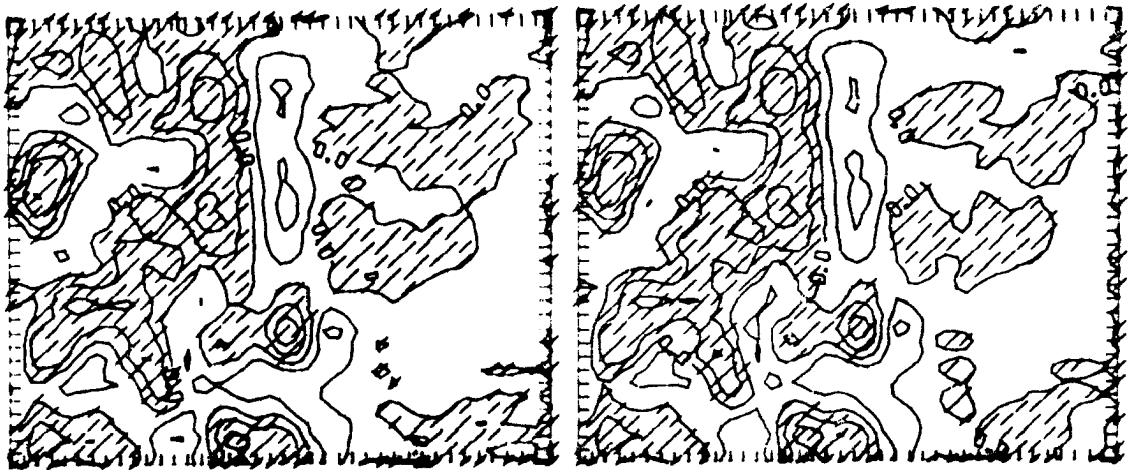
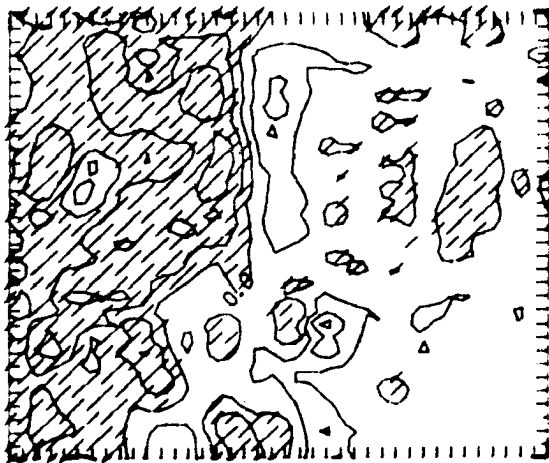
(a) $w:z^* = 0.03$, $t=9:00$ (b) $w:z^* = 0.03$, $t=9:30$ (c) $w:z^* = 2.0$, $t=10:00$ 

Figure 43

Contour plots of vertical velocity in m sec^{-1}
 (a) at 0900 LST on the $z^* = 0.03$ km surface
 contoured from -0.9 to 0.6 in intervals of 0.3
 (b) at 0930 LST on the $z^* = 0.03$ km surface
 contoured from -0.6 to 0.6 in intervals of 0.3
 (c) at 1000 LST on the $z^* = 2.0$ km surface
 contoured from -4.0 to 6.0 in intervals of 1.0 .

there is a brief period of moistening at about 0900 LST, but after that the lower layers continue to dry and become more uniform in distribution until about 1700 LST.

The SPACE mesonet system reveals that by 0900 LST, thunderstorms had developed west of Limon. In the eastward regions, away from the influence of the storms, the entire area experienced a clockwise windshift, enhancing the easterly component, and underwent cooling and drying. This process of cooling, drying, and of anti-cyclonic windshift continued through 1200 LST except in the areas underneath thunderstorms which underwent stronger cooling and experienced moistening of the air. Satellite imagery for this time reveals that convection began to develop over the mountainous areas near 1200 LST (Figure 44a). This is confirmed by SPACE cloud observations.

A strong north-south orientation of the simulated vertical velocity field below the planetary boundary layer is apparent by 1030 LST, forming into a two-celled circulation over the plains (Figure 45). The circulation at $z^* = 4$ km shows an east-west orientation, similar to that observed in Experiment B. By 1200 LST, the negative vertical velocity areas above the plains are building eastward (Figure 46a-b). However, the largest changes in divergence are occurring over the mountains. Negative vertical velocities are also increasing in area above the boundary layer. The Palmer Lake Divide continues to maintain weak positive vertical velocities ($< 0.3 \text{ m sec}^{-1}$). The observed surface winds at 1100 LST had increased in magnitude to about 10 m sec^{-1} which is close to

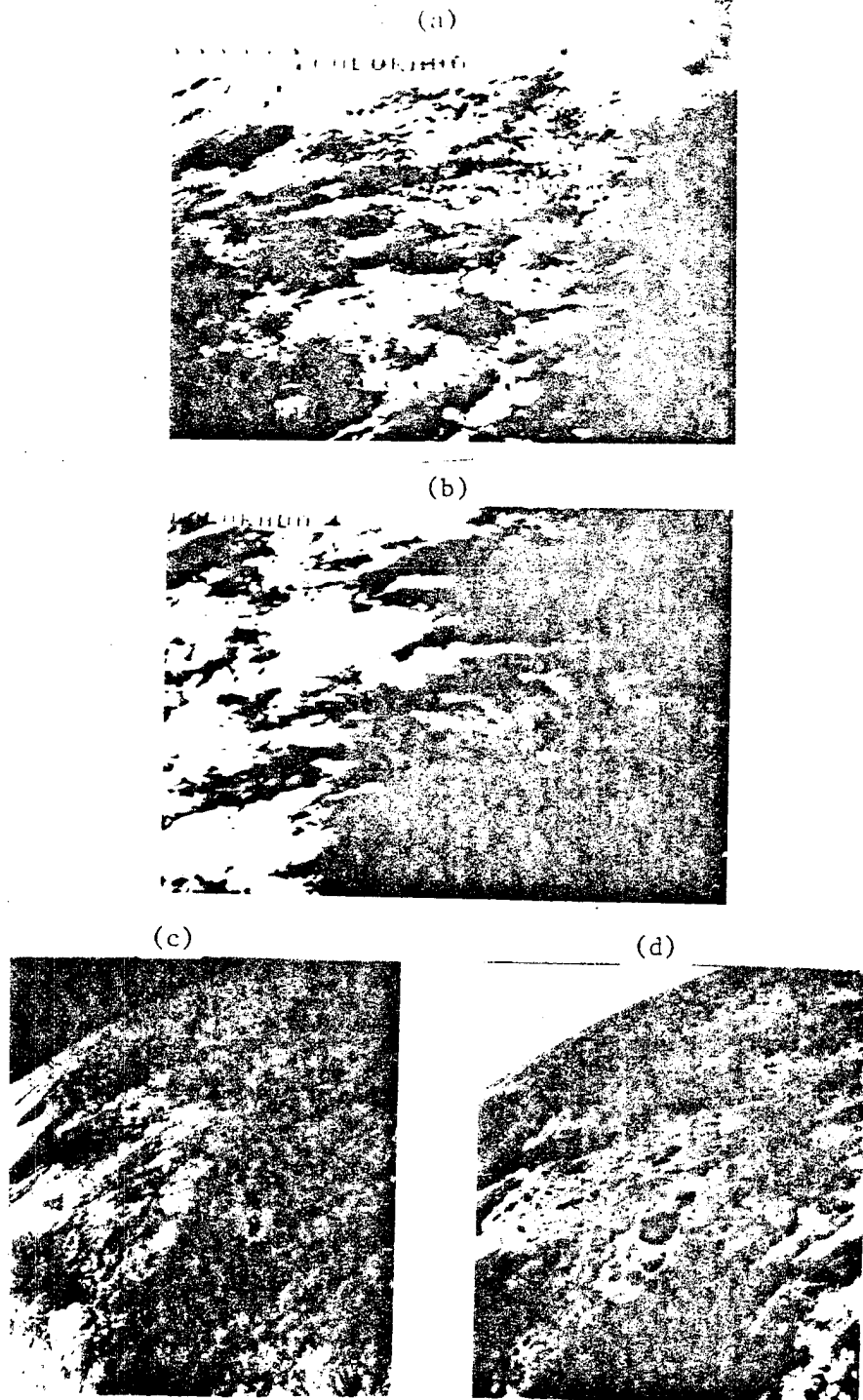


Figure 44 Satellite imagery taken on August 4, 1977 at
(a) 1200 LST (b) 1445 LST (c) 1800 LST
(d) 2100 LST (infrared data).

$w:z^* = 0.03, t=10:30$

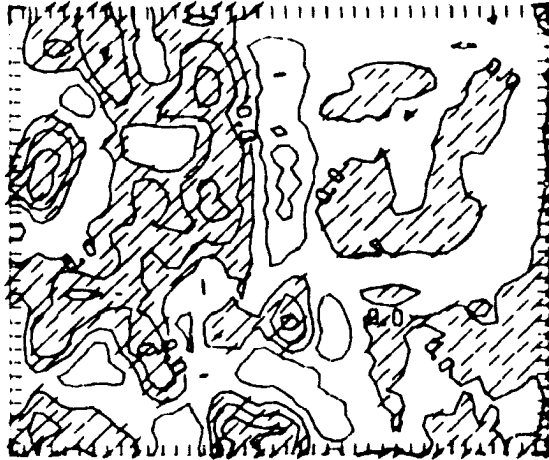


Figure 45 Contour plot of 1030 LST of vertical velocity in $m\ sec^{-1}$ on the $z^* = 0.03$ km surface contoured from -0.6 to 0.6 in intervals of 0.3 .

(a) $w:z^* = 0.03, t=11:30$

(b) $w:z^* = 0.03, t=12:00$

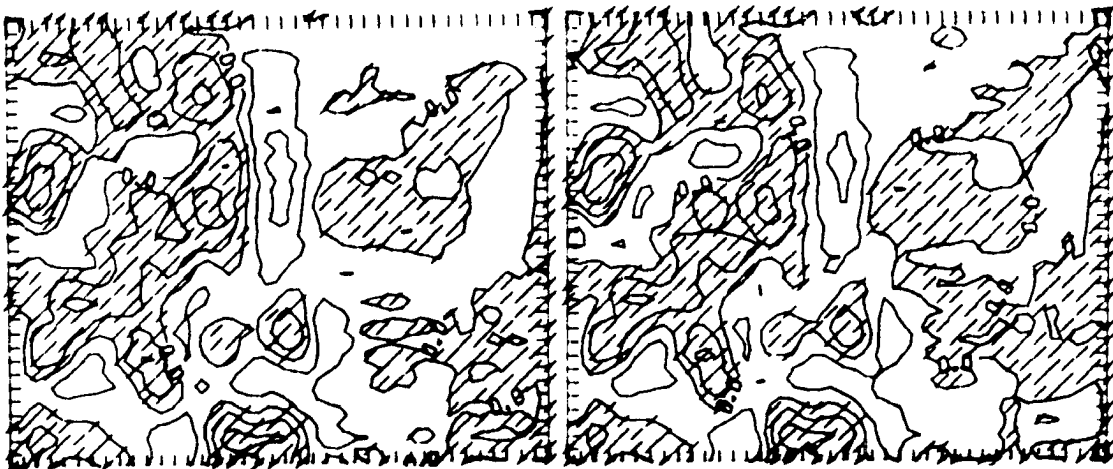


Figure 46 Contour plots of vertical velocity in $m\ sec^{-1}$ on the $z^* = 0.03$ km surface (a) at 1130 LST contoured from -0.8 to 0.8 in intervals of 0.4 (b) at 1200 LST contoured from -0.9 to 0.6 in intervals of 0.3 .

the average speed of the simulated winds at this time. (The maximum simulated surface wind speeds were about 18.5 m sec^{-1} .)

The north-south line of negative vertical velocity east of the Denver-Ft. Collins line develops in the lower layers through 1300 LST and an hour later, begins to move eastward. Magnitudes remain constant at about $\pm 0.6 \text{ m sec}^{-1}$. Above the boundary layer, the vertical velocities are beginning to weaken in magnitude, having values in the range $\pm 3.0 \text{ m sec}^{-1}$. By 1500 LST the plains are dominated by positive vertical velocities. There are enclaves of negative vertical velocities over the Palmer Lake Divide below the boundary layer and near the eastern edge of the domain above it (Figure 47a-b). The boundary layer is deepening throughout this period and reaches a depth of about 1.8 km near 1800 LST. The domain experiences a moistening trend beginning about 1500 LST above the boundary layer and about 1700 LST in the lowest layer.

According to the SPACE mesonet system, at 1500 LST in the areas which had endured thunderstorm passage, winds in the northern part of the experimental area shifted back to assume a generally northeasterly configuration. Winds in the extreme south, which were least affected by the thunderstorms, were consistently easterly. Since these easterlies were synoptically forced, there is no corresponding flow predicted by the model. Satellite imagery shows an extension of convection eastward over the plains approximately in the areas of the Cheyenne Ridge (Figure 44b) and Palmer Lake Divide (not visible in the figure) at 1445 LST. This is near the time that an eastward propagation of the vertical circulation takes place in the model. The Limon radar also

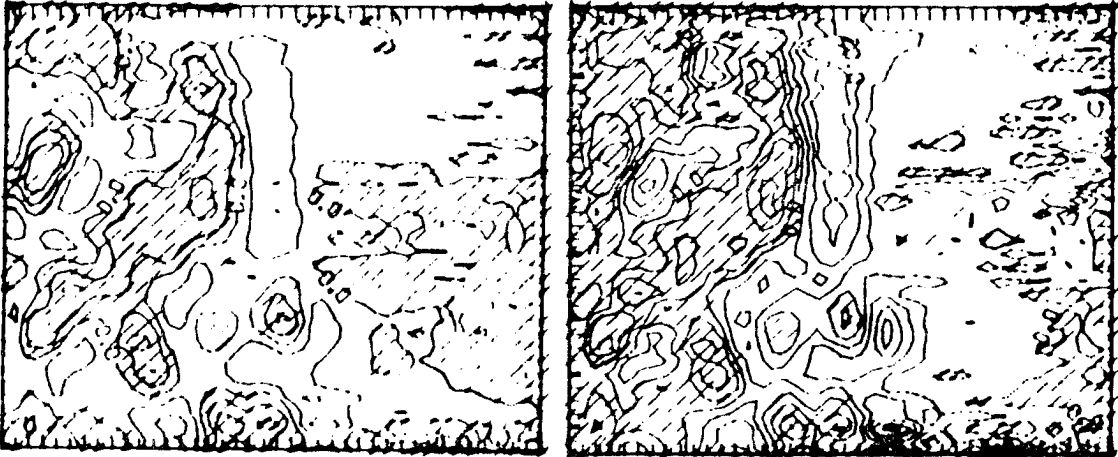
(a) $w:z^* = 0.03$, $t=15:00$ (b) $w:z^* = 2.0$, $t=15:00$ 

Figure 47 Contour plots of vertical velocity in m sec^{-1} at 1500 LST (a) on the $z^* = 0.03$ km surface contoured from -0.4 to 0.4 in intervals of 0.2 (b) on the $z^* = 2.0$ km surface contoured from -3.0 to 5.0 in intervals of 1.0 .

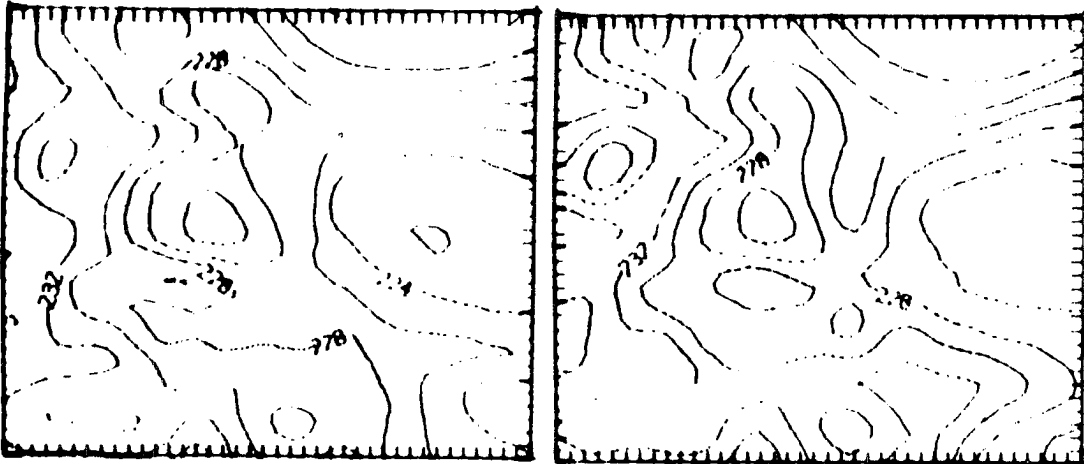
(a) $q:z^* = 0.03$, $t=17:00$ (b) $q:z^* = 0.03$, $t=19:00$ 

Figure 48 Contour plot of mixing ratio in $\text{grams metric ton}^{-1}$ on the $z^* = 0.03$ km surface contoured from 220 to 234 in intervals of 2 at (a) 1700 LST (b) 1900 LST.

reported a development of thunderstorm activity over the Palmer Ridge, though this occurred slightly later (1600 LST) than the propagation predicted by the model. Part of the delay may be accounted for by the time required for convection to develop to the point where it is detectable by radar.

A tornado was reported near Kiowa, Colorado (northeast of Colorado Springs) at 1545 LST. One can note a maximum of positive vertical velocity of 0.4 m sec^{-1} which is predicted by the model east of Colorado Springs (Figure 47), at 1500 LST. Though the spatial correlation of the predicted maximum w with the tornado sighting is poor, the vertical velocity maximum does not decrease until 1700 LST, making the temporal correlation reasonable. As noted before, these maxima of vertical velocity appear to be associated with steep topography gradients, and the splitting of the flow around peaks, leading one to speculate about the relation between the divergence around Pike's Peak and the preferred region of tornado genesis downwind. The flow-splitting would be expected to lead not only to convergence and associated vertical velocities, but also to an increase of vorticity. The process may also be enhanced by proximity of the region to the Palmer Lake Divide.

The areal coverage and intensity of negative vertical velocity over the plains increases from 1700 LST to 1900 LST. It is overtaken by positive vertical velocities, oriented in a north-south manner, beginning about 1900 LST above the boundary layer and about 2000 LST below it. A maximum depth for the boundary layer of 3.0 km is reached at about 2100 LST. The largest plains area of negative vertical velocity over the Palmer Lake Divide is

attacked from the south by the positive vertical velocity associated with the Arkansas River Valley. This process continues through 2200 LST, when the north-south orientation of the vertical velocity field becomes dominant. The planetary boundary layer during this time is becoming more horizontally uniform in depth. At 2300, it begins to diminish in depth.

The surface winds over the plains at 2100 LST were observed to be southerly at the northern stations of the domain and generally easterly towards the south. Satellite imagery pictures the convection as reaching the Kansas border by 2100 LST (Figure 44c-d). Moistening continues to increase in the lower layers, particularly in the northeast section of the domain (Figure 48a-b), but a drying trend occurs above the boundary layer from about 2200 LST onward.

Near 2400 LST the simulated north-south oriented lines of negative vertical velocity begin to weaken in the areas located over the major ridges. There is little further change. The height of the boundary layer continues to decrease. The vertical velocity field becomes more dominated by topography, as opposed to a north-south line orientation, while positive vertical velocity prevails over the plains. The east-west orientation of the vertical velocity and divergence fields at $z^* = 4$ km also gives way to a topographically forced circulation. The integration was ended at approximately 0300 LST the next day.

3.5 Comparison of results of Numerical Experiments B and C

The two simultaneous experiments had very similar temperature profiles and similar wind directions in the lower layers. Upper level winds in Experiment B had a southerly component and those in Experiment C a northerly component. The initial wind speeds were rather larger in Experiment C, and the surface temperature functions were quite different, as discussed. It is not surprising that in some respects the results of these two experiments were similar and in others they were decidedly different.

The occurrence of a jet-like flow in only one experiment might be partially explained by the lower average wind speed resulting in practically calm winds in the lee of the slopes. This would aid the thermally-induced wind turning process suggested above.

The early behavior of the moisture field can generally be described as drying throughout the domain in both experiments until about 1500 LST. This would indicate a mixing at all layers with air aloft, consistent with the dominance of the downslope regime, and perhaps the effects of numerical diffusion. In both experiments, there is an increase in moisture above the boundary layer beginning about 1500 LST, and below the boundary layer about 1700 LST. This comes several hours after the downslope regime begins to weaken, and probably represents both advective and diffusive mixing with lower layers as well as transport from the (static) boundaries. Since transport from lateral boundaries is the only source of moisture for the lower layers, this might explain the tardiness of the moistening there. The upper two

layers experience almost no change in mixing ratio, other than a smoothing out of gradients. This indicates that there is little mixing with lower layers during the integration. After the initialization procedure, however, the lower levels were significantly drier (0.8 g kg^{-1} at the lowest level) than the initial values, indicating a strong mixing process occurred during initialization.

The first indications of significant weakening of the down-slope circulation appear at about 1130 LST in Experiment B and about 1000 LST in Experiment C, presumably because of the shorter wavelength of the heating cycle in the latter experiment. It is also true that mountain maximum temperatures lag the plains maxima in Experiment B, which would be expected to retard upslope tendencies somewhat.

Winds speeds in Experiment B at the surface were about half of those in Experiment C. Wind directions were very similar over the mountains where, presumably, topography effects were dominant. Over the plains, however, Experiment B winds tended to be from the southwest while Experiment C winds were generally from the northwest. These directions are most consistent with winds in the fifth and sixth model layers, again pointing out that there was an unrealistically large mixing of the winds aloft downward to the surface.

The first incident of eastward propagation of the vertical velocity field in Experiment B occurs near 0630 LST, but is delayed in Experiment C until about 0930 LST. Since the causal mechanism for this propagation has not been determined, it is difficult to postulate reasons for the timing of this progression

of events, but it can be noted that in both cases, propagation commences approximately midway between minimum and maximum temperatures at the surface.

Vertical velocities were about 30% higher in Experiment C reflecting the increased convergence from both higher winds and a higher amplitude heating function. The vertical velocity field over the mountains was very similar in direction in the two cases until about 1500 LST, reflecting the dominance of topographic forcing there. After 1500 LST, the areas of negative vertical velocity associated with mountain peaks were predicted to extend significantly farther down the slopes in Experiment B than in Experiment C. This is probably a result of the fact that the surface temperature function in Experiment B varies less strongly with height than that used in Experiment C.

Near noon, several areas of negative vertical velocity on the lee slopes are spreading northward in Experiment C. There is no comparable occurrence in Experiment B, despite the fact that surface winds in Experiment B would seem to be more conducive to this spreading. Differences in the heating function would seem to be the most likely cause for discrepancies between the experiments in timing and intensity of events. Positive vertical velocities almost dominate the plains in Experiment C by 1500 LST, while Experiment B always retains significant areas of negative vertical velocity. After 1800 LST the gradients of vertical velocity are much smaller in Experiment B. The extension and breakup into a cellular structure of the line of positive vertical velocity

west of the Denver-Ft. Collins line occur nearly simultaneously in the two experiments, at about 0800 LST.

In both experiments the depth of the planetary boundary layer begins to increase at about 0630 LST, and reaches its maximum value around 2100 LST. At this time, the height of the boundary layer is about 3.5 km in Experiment B and 3.0 km in Experiment C. The magnitudes of surface convergence in Experiment B are less than half of those in Experiment C until about noon, after which convergences in the two experiments are similar. This indicates that surface heating rather than convergence probably accounted for the greater depth in Experiment B. Although Experiment C had a higher amplitude of surface heating, it had a much shorter wavelength so that surface heating operated over a longer period in Experiment B. The three or four rawinsondes launched daily were not sufficient to provide reliable values for the time or magnitude of the maximum boundary layer depth in either the NHRE or the SPACE. The available data suggest that the boundary layer in the experimental region might reach a depth of 2.0-2.5 km at about 1700-1900 LST. If the growth of the boundary layer in the model had been terminated during this period, say by the establishment of a nocturnal inversion, the depth would have reached a value of about 2.8 km.

4. DISCUSSION, SUMMARY, AND CONCLUSIONS

4.1 Discussion of Results

As mentioned above, there was some correspondence of the model output with observations. The organization of predicted vertical velocity along north-south oriented lines was seen in radar observations on July 9, 1973, as well as climatologically, to proceed in a manner similar to that predicted by the model. Several episodes of eastward propagation of north-south oriented lines of vertical velocity were simulated over the plains, and it was noted that this behavior was observed both on the study days and climatologically. In the model, mountainous areas of positive vertical velocity remained relatively stationary, while observed isolated cumulonimbi were able to move eastward if they developed sufficiently. The findings of Henz (1974) indicated the existence of several mountainous areas of preferred storm genesis. These localized areas of enhanced convective development associated with Long's Peak and Pike's Peak were not simulated as maxima in vertical velocity largely because features of this small horizontal extent were smoothed out of the model topography. The magnitudes of the winds were reasonable throughout the simulation, but this is not surprising in view of the initial conditions used.

It was heartening to see that, in both runs, the time of observed onset of convection coincided with a distinct weakening of the downslope regime.

Some of the most often-noted summertime phenomena, however, fail to be strongly evident in these simulations. Especially troublesome is the absence of an upslope circulation near the time of maximum heating. In an effort to understand why the atmosphere behaves in this manner, it is instructive to consider the defects of the model with regard to their ability to affect upslope circulations.

The model is rather coarse in its vertical resolution, and notably has only three vertical levels in the boundary layer. This is particularly a problem over the area investigated, since the boundary layer undergoes wide fluctuations of depth in passing from mountainous to plains regions. Pielke, in his sea-breeze study was not troubled by this problem, though his vertical resolution was somewhat greater. One would expect that the effect of insufficient boundary-layer resolution would be to distort the shape or magnitude of the upslope, rather than suppress it altogether if it was sufficiently forced. The westerly surface winds produced during the initialization process, presumably by mixing down momentum from aloft, increased winds speeds to the point that very strong forcing would have been required to turn the winds. This failure of the model to simulate the decoupling of the boundary layer flow from the free atmosphere suggests another possible explanation for the failure of the model to produce upslope. Upslope normally occurs when mountain thermal circulations, capped by the boundary layer, are required to draw air from the plains, by continuity considerations (see Defant, 1951). This

circulation is usually confined to a layer about 200 m thick. If the lower levels are free to interact with the upper level flow, as appears to be the case in the model, mountain thermal circulations will no longer be constrained to draw air from the plains. The strong effects of lateral boundary conditions in Experiment A were also pointed out, but in the upstream differencing method used, only inflow boundaries can affect the interior of the domain, so that lateral boundary conditions would either be helpful or indifferent to upslope. The upper boundary condition produced a material surface height which was rather noisy, containing many $2\Delta x$ waves. Moreover, the results of Experiment A indicate that at least initially, the material surface can produce large vertical velocities in the upper layers, and there were indications that this could affect the entire depth of the model. Considering the moisture field as a passive tracer, however, it would appear that there is little vertical advection in the upper two time-dependent model levels after quasi-steady-state is reached. The lack of correspondence between a material surface and the real atmosphere, as well as the difficulty this boundary condition engenders in the initialization process indicate that a search for an alternative upper boundary condition would be advisable.

The fact that the downslope regime which was observed in cases B and C was weakest during the time of maximum heating suggests that perhaps the sought-for upslope would have occurred if the heating function had been greater in magnitude. It should be noted, however, that the heating function was based on observed

data and was realistic in amplitude (see, for example, Pielke and Mehring, 1977). Orville (1964) was able to obtain an upslope with considerably more subdued thermal forcing, though the models are not entirely comparable. Orville's model was two-dimensional which severely limits the possible reactions to a pressure gradient. The results might also be explained if the pressure gradient produced by realistic heating over the scale of this three-dimensional domain requires some further forcing, such as synoptic-scale support or the release of latent heat, to produce a strong upslope flow.

As noted earlier, there are several unrealistic features of the heating function used. The effective time of sunrise, i.e. the approximate time of surface temperature increase, is several hours earlier than actual sunrise. This was a consequence of forming a "closest fit" with the data. It is presumed that this might modify the timing or amplitude of the resulting forcing, but it is unlikely that it affected the qualitative nature of the results. The phase of the diurnal temperature wave is a function of elevation. When the plains maximum lags the mountain temperature maximum, as in Experiment B, there should be an effective enhancement of the mountain-plains thermal gradient at the later maximum, which should tend to encourage an upslope flow.

The model heating function contained no provision for enhanced heating of solar-facing slopes. This should have been of minimal importance near mid-day and would have enhanced heating of westward facing slopes during the afternoon heating maximum. However, during the morning hours, inclusion of a slope heating effect could

be expected to produce an early upslope tendency, which might have been able to combat the build-up of westerly momentum observed early in the experiment.

It also should not be overlooked that such slope heating may well provide local enhancement of upslope flow, on scales not resolved by the model. The finest horizontal resolution of the model is 11 km, and the topography is strongly smoothed on a scale larger than this. Thus it would seem possible that the model might produce a stronger upslope if it could include the integrated effects of many locally forced upslope circulations.

The lack of moisture in the model would not seem to be a primary cause in the encouragement of propagation of disturbances. The role of latent-heat related density currents in the propagation and steering of thunderstorms has been the subject of theoretical speculation and numerical modeling and seems well-established (see, for example, Mongreif and Miller, 1976). It is true, however, that Orville found that the inclusion of latent heat effects encouraged the development of upslope flow in certain situations. Wetzel (1973) also found in a climatological study that the solar-driven circulation was suppressed on dry days.

The fate of thunderstorms, which were observed to develop over the mountains in areas of enhanced vertical velocity, could be profoundly affected by their interaction with areas of rising motion or subsidence over the plains, such as those predicted by the model. If a downdraft-induced density current causes a storm to propagate into an area where vertical velocity is enhanced by topographic or thermal forcing, the results could be synergistic.

4.2 Comparison with Other Selected Models

Comparisons among numerical models can easily lead one to lose sight of the real phenomena being investigated. It is possible, however, to gain a greater degree of understanding of the particular characteristics of the models by such comparisons. In this spirit, one should note first that previous models simulating mountain-plains circulations have been two-dimensional and rather idealized. A review and discussion of some early attempts is given in Fosberg (1967). Most of the more sophisticated recent simulations are not directly comparable with the present model. Orville's continuing series of models, for example, had a much finer grid mesh (100 m). The "mountain" was 1 km high and had a 45° slope--certainly steeper than slopes found in the present model. This had the effect of producing a large thermal gradient over a relatively short horizontal distance. The temperature wave amplitude was comparable to that used here (7° C in the plains), however, the two-dimensional nature of the model forced any upslope flow to lie in a plain normal to the "ridge line".

Clark (1976) has run a model using the deep equations of Ogura and the co-ordinate transformation system of Gal-Chen (1973). His grid-spacing was also rather fine (600 m) and his Witch of Agnesi topography had a height of 1 km. He reported good agreement with solutions of the linearized equations, but it is interesting to note that his model developed a strong downslope circulation when a non-linear lower boundary condition was used.

The model which probably has the greatest potential for comparison with the present study is Dirks (1969). His heating

function was comparable in magnitude (9° C over the plains, 5° C at the peak), though again the two-dimensionality of the model makes the effective forcing stronger. His grid spacing varied from 5 km near the mountain to 40 km at the eastern edge. The peak was 1.75 km high and 35 km wide. His boundary conditions, it should be noted, were quite conducive to the upslope conditions observed. The eastern boundary was "open" giving the effect of an infinite plain, but no normal flow was allowed at the western edge (i.e. over the peak). This forced any pressure anomaly to draw air from the east. None of these studies used a real sounding for the thermodynamic initialization, substituting a constant lapse rate of potential temperature.

Other versions of the model developed by Pielke have been used to study land-sea breezes and heated island effects. It has not previously been applied to an area of such high amplitude and complex topography. The fact that land-sea breezes were successfully induced by a strictly thermal forcing suggests that the actual mechanisms of the Rockies-Great Plains circulation may involve additional forcing features.

4.3 Summary and Conclusions

A three-dimensional, hydrostatic, primitive equation model was employed to simulate one idealized and two real cases. Several similarities with observations were noted, giving some measure of credence to the model. However, there was little correspondence with the observed surface flow, especially with respect to the wind direction. It is somewhat puzzling that the model produces

some agreement with observation but lacks the upslope flow observed. The fact that the observed upslope on the two study days developed with synoptic support, while the model, which lacks any synoptic-scale forcing failed to develop upslope, leads one to speculate about whether the climatologically observed summertime upslope flow (see, for example, Hering and Borden, 1962; and Kuo and Orville, 1973) is correlated with persistent or common synoptic situations which might support such flow.

Several possible reasons for the departure of the model from observations were commented upon, with the intent of both discerning causal mechanisms for the observed upslope, and gaining insight into the characteristics of the model. Singled-out as particularly important were the deviation of the model winds from observations during the initialization process, absence of synoptic scale forcing, local topographic forcing (especially slope heating) and the effects of latent heat release. It is speculated that the influence of an enormous mountain ridge, both on the development of meso- to synoptic scale forcing and on the difficulty of formulating and initializing appropriate numerical models is of overwhelming importance and that future progress in understanding mountain-plains circulation will depend on coming to grips with these problems.

4.4 Suggestions for Future Research

Given the initial and boundary conditions used, the results of the experiments indicate that upslope flow can not be modeled using thermal forcing induced by large topographic differences on the scale of several tens of kilometers without some

synoptic forcing. In order to investigate the role of synoptic influences, a time-dependent lateral boundary condition will need to be devised. The coding necessary for this is not particularly difficult, but gathering of data necessary to design a realistic forcing, with the complicating features of mountainous topography considered might be quite onerous.

Several aspects of the numerics of the model could be revised. The forward-upstream differencing method produces a disturbing amount of numerical diffusion perhaps, in part, accounting for the strong vertical mixing of horizontal momentum. The "material surface" upper boundary condition produces much noise with uncertain results. The questions of the proper treatment of lateral boundary conditions remains largely open. Some means should be devised to force the model into an initial "steady state" which is consistent with observations. It has been suggested that selected points be held constant at initial values during "spin-up". This appears promising, but it might require exorbitant "spin-up" times; and it is not clear that the model even then will adequately represent the complex imbalanced, non-static situation in the atmosphere at the desired time, particularly over data-sparse mountainous areas.

Because of the larger core available on the CRAY-I computer, it will be possible to store more vertical levels, thus making resolution of the boundary layer more complete. The possibility for more horizontal gridpoints will enable future investigators to explore the role of the great plains on the circulation (see Dirks, 1969), as well as to better determine the effect of more highly resolved topographic features. This latter effect might be

investigated in a series of increasing resolution, idealized mountain studies, perhaps using a two-dimensional version of the model.

A more sophisticated forcing function, based on a radiation budget, and including slope angle considerations, would help to resolve the question of the distribution of surface potential temperature, though the data available for the design and evaluation of a realistic surface energy budget remain meager over mountainous terrain. A surface hydrological cycle including evapotranspiration and evaporation would also make such a surface energy budget parameterization more realistic and provide a mid-level moisture supply over the plains.

Inclusion of a parameterization of the effects of convection, particularly downdraft-induced density currents, or coupling with a cumulus model are desirable goals but are difficult to execute, so that this should be regarded as a longer-range plan.

REFERENCES

REFERENCES

- Anderson, G. E., 1971: Mesoscale influences on wind fields. J. Appl. Meteor., 10, 377-386.
- Anthes, R. A., 1976: Numerical prediction of severe storms-- certainty, possibility, or dream? Bull. Amer. Meteor. Soc., 57, 423-430.
- _____, 1975: Some mesoscale modeling activities at Penn. State. Open SESAME, D. K. Lilly, Ed., National Oceanic and Atmospheric Administration, Boulder, CO, 302-318.
- _____, 1977: Report of regional scale modeling group. Project SESAME Planning Documentation Volume, D. K. Lilly, Ed., National Oceanic and Atmospheric Administration, Boulder, CO, 49-60.
- Arakawa, A. and W. H. Schubert, 1974: Interaction of a cumulus cloud ensemble with the large-scale environment, Part I. J. Atmos. Sci., 31, 674-701.
- Archibald, P. C. II and N. A. Court, 1964: Curves. Encyclopedia Britannica.
- Asai, T., 1964: Cumulus convection in the atmosphere with vertical wind shear; numerical experiment. J. Meteor. Soc. Japan, XLII, 245-259.
- Blackadar, A. K. and H. Tennekes, 1968: Asymptotic similarity in neutral barotropic planetary boundary layers. J. Atmos. Sci., 25, 1015-1020.
- Bonner, W. D., 1968: Climatology of the low-level jet. Mon. Wea. Rev., 96, 833-850.
- Buettner, K. J. K. and N. Thyer, 1965: Valley winds in the Mount Rainier area. Archiv. Meteor. Geophys. Bioklim., 14, 106.
- Chagnon, S. A. Jr., 1975: Operations of mesoscale networks. Illustrated by METROMEX, Bull. Amer. Meteor. Soc., 56, 971-977.
- Chalon, J. P., J. C. Fankhauser and P. J. Eccles, 1976: Structure of an evolving hailstorm, Part I: General characteristics and cellular structure. Mon. Wea. Rev., 104, 564-575.
- Clark, T. L., 1976: A Three-Dimensional Small Scale Dynamic Model Using a Terrain-Following Co-ordinate Transformation. Atmospheric Research Directorate Report #APRBP8, 78pp.
- Colson, J., 1801: Analytical Institutions. London, Taylor and Wilkes.

REFERENCES (CONT'D)

- Committee on Climate and Weather Fluctuation and Agricultural Production, 1976: Climate and Food. National Academy of Science, Washington, DC, 212pp.
- Cotton, W. R., 1974: Modeling of convective storms. Open SESAME, D. K. Lilly, Ed., National Oceanic and Atmospheric Administration, Boulder, CO, 319-340.
- _____ and R. L. George, 1978: A summer with PAM. Fourth Symposium on Meteorological Observations and Instrumentation, American Meteorological Society, Boston, MA, 87-92.
- _____, D. Hahn and R. Banta, 1978: Air turbulence measurements in and below cumulus congestus over mountainous terrain. Conference on Cloud Physics and Atmospheric (sic) Electricity, American Meteorological Society, Boston, MA, 408-415.
- _____, R. Pielke and P. Gannon, 1976: Numerical experiments on the influence of mesoscale circulation on the cumulus scale. J. Atmos. Sci., 33, 252-261.
- _____ and G. J. Tripoli, 1978: Cumulus convection in shear flow--three dimensional numerical experiments. J. Atmos. Sci., 35, 1503-1521.
- Danielson, K. S. and W. R. Cotton, Eds., 1977: SPACE Log. Dept. of Atmos. Sci., Colo. State Univ., Ft. Collins, CO, 399pp.
- Deardorff, J., 1974: Three-dimensional numerical study of the height and mean structure of a heated planetary boundary layer. Boundary-Layer Meteorology, 7, 81-106.
- Deaven, D. G., 1976: A solution for boundary problems in isentropic co-ordinate models. J. Atmos. Sci., 33, 1702-1713.
- Dirks, R. A., 1969: A Theoretical Investigation of Convective Patterns in the Lee of the Colorado Rockies. Atmos. Sci. Paper #145, Atmos. Sci. Dept., Colo. State Univ., Ft. Collins, CO, 122pp.
- Elliot, R. D. and Einar L. Hovind, 1964: On convection bands within Pacific coast storms and their relation to storm structure. J. Appl. Meteor., 3, 143-154.
- Fankhauser, J. C., 1976: Structure of an evolving hailstorm, Part II. Thermodynamic structure and airflow in the near environment. Mon. Wea. Rev., 104, 576-587.

REFERENCES (CONT'D)

- Fosberg, M. A., 1967: Numerical analysis of convection over a mountain ridge. J. Appl. Meteor., 6, 889-904.
- Fujita, T., H. Newstein and M. Tepper, 1956: Mesoanalysis, An Important Scale in the Analysis of Weather Data. U.S. Department of Commerce Research Paper #39, Washington, DC, 83pp.
- _____, K. A. Stybar and R. Brown, 1962: On the mesometeorological field studies near Flagstaff, Arizona. J. Appl. Meteor., 1, 26-42.
- Gal-Chen, T., 1973: Numerical Simulation of Convection with Topography. Ph.D. Thesis, Columbia Univ., New York, NY, 170pp.
- _____, and R. C. Somerville, 1975: On the use of a co-ordinate transformation for the solution of the Navier-Stokes equations. J. Comp. Physics, 17, 209-228.
- George, R. L., 1978: Evolution of Mesoscale Convective Systems over Mountainous Terrain. Master's Thesis, Dept. of Atmos. Sci., Colo. State Univ., Ft. Collins, CO.
- _____, and W. R. Cotton, 1978: The characteristics of evolving mesoscale systems over mountainous terrain as revealed by radar and PAM. Conference on Cloud Physics and Atmospheric (sic) Electricity, American Meteorological Society, Boston, MA, 443-450.
- Giraytys, J., 1975: Conference summary: Third symposium on meteorological observations and instrumentation. Bull. Amer. Meteor. Soc., 56, 989-991.
- Gokhale, N. R., 1975: Hailstorms and Hailstone Growth. Albany, NY, SUNY Press, 465pp.
- Grandi, G., 1718: Note al trattato del Galileo del monte naturale accelerato. Opere di Galileo Galilei, Vol. 3, Firenze, p. 393.
- Haltiner, G. J., 1971: Numerical Weather Prediction. New York, John Wiley and Sons, 111pp.
- Hane, C. E., 1973: The squall line thunderstorm: Numerical experimentation. J. Atmos. Sci., 30, 1672-1690.
- Henz, J. F., 1974: Colorado High Plains Thunderstorm Systems-- A Radar--Synoptic Climatology. Master's Thesis, Dept. of Atmos. Sci., Colo. State Univ., Ft. Collins, CO, 82pp.

REFERENCES (CONT'D)

- Hering, W. S. and T. R. Bordon, Jr., 1962: Diurnal variation in the summer wind field over the central U.S. J. Appl. Meteor., 19, 81-86.
- Huang, Y., 1969: Black Hills Mesoscale Numerical Model. Master's Thesis, South Dakota School of Mines and Technology, Rapid City, SD, 70pp.
- Jones, R., 1973: A Numerical Experiment on the Prediction of the Northeast (Winter) Monsoon in Southeast Asia. National Oceanic and Atmospheric Administration Technical Report #ERL 272-WMPO 3, 56pp.
- Kaplan, M. L. and D. A. Paine, 1973: A 32-km moist primitive equation model providing for scale interaction. J. Atmos. Sci., 30, 213-222.
- Kessler, E., 1969: On the distribution and continuity of water substance in atmospheric circulations. Meteor. Monogr., 10, no. 32, 84pp.
- Klemp, J. B. and R. B. Wilhelmson, 1978: Simulation of three-dimensional convective storm dynamics. J. Atmos. Sci., 35, 1070-1096.
- Kreitzberg, Carl W., 1976: Interactive applications of satellite observations and mesoscale numerical models. Bull. Amer. Meteor. Soc., 57, 679-685.
- _____, 1974: Regional and mesoscale modeling at Drake. Open SESAME, D. K. Lilly, Ed., National Oceanic and Atmospheric Administration, Boulder, CO, 289-301
- _____ and D. J. Perkey, 1976: Release of potential instability: Part I. A sequential plume model within a hydrostatic primitive equation model. J. Atmos. Sci., 33, 456-475.
- _____ and _____, 1977: Release of potential instability: Part II. The mechanism of convective/mesoscale interaction. J. Atmos. Sci., 34, 1569-1595.
- _____, _____ and J. E. Pinkerton, 1974: Mesoscale Modeling, Forecasting and Remote Sensing Research. Report #AFCRL-TR-74-0253, Dept. of Physics and Atmos. Sci., Drexel Univ., Philadelphia, PA, 318pp.
- Kuo, H. L., 1968: The thermal interaction between the atmosphere and the earth and propagation of diurnal temperature waves. J. Atmos. Sci., 25, 682-706.

REFERENCES (CONT'D)

- Kuo, J. and H. D. Orville, 1973: A radar climatology of summer-time convective clouds in the Black Hills. J. Appl. Meteor., 12, 359-368.
- Lavoie, R. L., 1972: A mesoscale numerical model of lake-effect storms. J. Atmos. Sci., 29, 1025-1040.
- _____, 1974: A numerical model of trade wind weather in Oahu. Mon. Wea. Rev., 102, 630-637.
- Lewis, J. M. and Y. Ogura, 1973: Large scale influences upon the generation of a mesoscale disturbance. Eighth Conference on Severe Local Storms, American Meteorological Society, Boston, MA, 308-314.
- _____, _____ and L. Gidel, 1974: Large-scale influence upon the generation of a mesoscale disturbance. Mon. Wea. Rev., 102, 545-560.
- Lilly, D. K., 1964: Numerical simulation for the shape-preserving two-dimensional thermal convection element. J. Atmos. Sci., 21, 83-98.
- _____, 1977: Severe storms and storm systems: Scientific background, methods and critical questions. Project SESAME Planning Documentation Volume, D. K. Lilly, Ed., National Oceanic and Atmospheric Administration, Boulder, CO, 1-22.
- Liu, J. Y. and H. D. Orville, 1969: Numerical modeling of precipitation and cloud shadow effects on mountain-induced cumuli. J. Atmos. Sci., 26, 1283-1298.
- Mahrer, Y. and R. Pielke, 1977a: The effects of topography on sea and land breezes in a two-dimensional numerical model. Mon. Wea. Rev., 105, 1151-1162.
- _____ and _____, 1977b: A numerical study of airflow over irregular terrain. Beitrag zur Physik der Atmosphere, 50, 98-113.
- _____ and _____, 1976: Numerical simulation of the airflow over Barbados. Mon. Wea. Rev., 104, 1392-1402.
- Manton, M. J. and W. R. Cotton, 1977: Formulation of Approximate Equations for Modeling Moist, Deep Convection on the Mesoscale. Atmospheric Science Paper #266, Dept. of Atmos. Sci., Colo. State Univ., Ft. Collins, CO, 62pp.
- Miles, J. W. and H. E. Huppert, 1969: Lee waves in a stratified flow: Part 4. Perturbation approximations. J. Fl. Mech., 35, 497-525.

REFERENCES (CONT'D)

- Montcrieff, M. W. and M. J. Miller, 1976: The dynamics and simulation of tropical squall lines and cumulonimbus. Quart. J. Roy. Meteor. Soc., 102, 373-394.
- Ogura, Y., 1962: Convection of isolated masses of a buoyant fluid: A numerical calculation. J. Atmos. Sci., 19, 492-502.
- Orlanski, I., 1975: A rational subdivision of scales for atmospheric processes. Bull. Amer. Meteor. Soc., 56, 527-530.
- Orville, H. D., 1968: Ambient wind effects on the initiation and development of cumulus clouds over mountains. J. Atmos. Sci., 25, 385-403.
- _____, 1965: A numerical study of the initiation of cumulus clouds over mountainous terrain. J. Atmos. Sci., 22, 684-699.
- _____, 1964: On mountain upslope winds. J. Atmos. Sci., 21, 622-633.
- _____ and F. J. Kopp, 1977: Numerical simulation of the life history of a hailstorm. J. Atmos. Sci., 34, 1596-1618.
- _____ and L. J. Sloan, 1970: A numerical simulation of the life history of a rainstorm. J. Atmos. Sci., 27, 1148-1159.
- Perkey, D. J., 1976: Prediction of Convective Activity Using a System of Parasitic-Nested Numerical Models. National Aeronautics and Space Administration Contractor Report #CR-2761.
- Pielke, R. A., 1974: A survey of fine-mesh modeling techniques. Open SESAME, D. K. Lilly, Ed., National Oceanic and Atmospheric Administration, Boulder, CO, 219-232.
- _____, 1974: A three-dimensional model of the sea breezes over south Florida. Mon. Wea. Rev., 102, 115-139.
- _____, 1973: A Three Dimensional Numerical Model of the Sea-Breezes over South Florida. Ph.D. Dissertation, the Penn. State Univ., University Park, PA, 135pp.
- _____ and W. R. Cotton, 1977: A mesoscale analysis over south Florida for a high rainfall event. Mon. Wea. Rev., 105, 343-362.
- _____ and Y. Mahrer, 1975: Representation of the heated planetary boundary layer in mesoscale models with coarse vertical resolution. J. Atmos. Sci., 32, 2288-2308.

REFERENCES (CONT'D)

- Pielke, R. A. and P. Mehring, 1977: Use of mesoscale climatology in mountainous terrain to improve the spatial representation of mean monthly temperatures. Mon. Wea. Rev., 105, 108-112.
- Pitchford, K. L. and J. London, 1962: The low-level jet as related to nocturnal thunderstorms over midwest United States. J. Appl. Meteor., 1, 43-47.
- Randerson, D., 1975: Conference summary: First conference on regional and mesoscale modeling, analysis and prediction. Bull. Amer. Meteor. Soc., 56, 1094-1103.
- Ross, Bruce B., 1974: Current development of a three dimensional mesoscale model at the geophysical fluid dynamics laboratory. Open SESAME, D. K. Lilly, Ed., National Oceanic and Atmospheric Administration, Boulder, CO, 265-276.
- Sasaki, Y., 1959: A numerical experiment of squall-line formation. J. Meteor., 16, 347-353.
- Scorer, R. S., 1972: The interaction of local weather and pollution problems. Air and Water Pollution, Wesley E. Brittin, Ed., Boulder, CO, Colorado Associated Universities Press, 571-586.
- Tang, W., 1974: Mountain-valley circulation and dispersion of vehicular exhaust gasses from a valley highway. Symposium on Atmospheric Diffusion and Air Pollution, American Meteorological Society, Boston, MA, 233-237.
- Thompson, P. T., 1971: Use of Mountain Recreation Resources: A Comparison of Recreation and Tourism in the Colorado Rockies and the Swiss Alps. Univ. of Colo., Boulder, CO, 225pp.
- Uccellini, L. W., 1973: A case study of apparent gravity wave initiation of severe convective storms. Eighth Conference on Severe Local Storms, American Meteorological Society, Boston, MA, 343-350.
- Wallace, J. M. and F. R. Hartranft, 1969: Diurnal wind variations, surface to 30 km. Mon. Wea. Rev., 97, 446-455.
- Wang, J., 1967: Agricultural Meteorology. Palo Alto, CA, Agricultural Weather Information Service, 693pp.
- Wetzel, P. J., 1973: Moisture Sources and Flow Patterns During the Northeast Colorado Hail Season. Master's Thesis, Dept. of Atmos. Sci., Colo. State Univ., Ft. Collins, CO, 89pp.
- Wexler, H., 1961: A boundary layer interpretation of the low-level jet. Tellus, 13, 368-378.

BIBLIOGRAPHIC DATA SHEET		1. Report No. CSU-ATSP- 303	2.	3. Recipient's Accession No.
4. Title and Subtitle A Numerical Simulation of Mesoscale Flow Over Mountainous Terrain				5. Report Date December, 1978
7. Author(s) Richard Lynn Hughes				6.
9. Performing Organization Name and Address Department of Atmospheric Science Colorado State University Foothills Campus Fort Collins, Colorado				8. Performing Organization Rept. No. CSU-ATSP- 303
12. Sponsoring Organization Name and Address National Science Foundation, Washington, D.C. 20550 National Center for Atmospheric Research, National Hail Research Experiment, Boulder, Colorado 80307				10. Project, Task/Work Unit No.
				11. Contract, Grant No. NSF # ATM 09770 NHRF # 6016
15. Supplementary Notes				13. Type of Report & Period Covered Masters Thesis
				14.
16. Abstracts A three-dimensional, hydrostatic, primitive equation mesoscale model was used to investigate thermally driven flow over the Colorado Rocky Mountains and plains. One idealized and two real cases were simulated. Some similarities to observations and climatological data were obtained. Episodes of eastward propagation of vertical velocity regions were predicted. Persistent lines of rising motion were simulated near areas of observed enhanced cloudiness. Weakening of the modeled downslope circulation occurred at the time that convection was observed to erupt. There was, however, poor correspondence with the observed surface flow, especially with respect to wind direction.				
17. Key Words and Document Analysis. 17a. Descriptors Mesoscale Meteorology; Numerical Simulation; Orogenic Mesoscale Systems; Ridge/Valley Circulation				
17b. Identifiers/Open-Ended Terms				
17c. COSATI Field/Group				
18. Availability Statement		19. Security Class (This Report) UNCLASSIFIED		21. No. of Pages 123
		20. Security Class (This Page) UNCLASSIFIED		22. Price